THE ASTROPHYSICAL JOURNAL SUPPLEMENT SERIES, 107:621–660, 1996 December

HST SNAPSHOT SURVEY OF 3CR RADIO SOURCE COUNTERPARTS. I. INTERMEDIATE REDSHIFTS

SIGRID DE KOFF,[1,2] STEFI A. BAUM,[1] WILLIAM B. SPARKS,[1] JOHN BIRETTA,[1] DANIEL GOLOMBEK,[1] FERDINANDO MACCHETTO,[1] PATRICK MCCARTHY,[3] AND GEORGE K. MILEY[2]

Received 1996 February 14; accepted 1996 June 27

ABSTRACT

We have obtained images of 267 3CR radio galaxies and quasars by conducting a snapshot survey with *HST*'s WFPC2 through a broadband red (F702W) filter. This is the first in a series of papers resulting from this survey, describing and presenting the basic data. Here we focus on the 77 radio galaxies within the redshift range $0.1 < z < 0.5$ (91% of the total number of 3CR radio galaxies within this redshift range). The images show that on the 0.″1 scale of the *HST* observations there is a wide variety of structure in radio galaxy morphology. At least 30% of the galaxies show dust, either well-defined dust lanes or chaotically distributed throughout the galaxy. We find disturbed morphologies, such as multiple nuclei and tails of emission, that could indicate merging systems. There is an obvious optical synchrotron jet in 3C 346, and another eight jet candidates are present.

Subject headings: galaxies: interactions — galaxies: jets — galaxies: structure — radio continuum: galaxies — surveys

1. INTRODUCTION

Powerful radio emission from galaxies is one of the most astrophysically interesting and important phenomena. The extreme transparency of the "radio universe" allows us to find galaxies across a wide range of redshifts, and thereby we can study the evolution and structure of radio galaxies. We may both use these objects as unique probes of their environment and investigate the energetic active galactic nuclei (AGN) phenomenon itself. The high spatial resolution and sensitivity of *HST* imaging observations offer an attractive route to tackle such problems as the following: (1) what are the frequency and characteristics of optical jets; (2) do optical continuum and radio structure align and is there detailed morphological correspondence; (3) how common are dust lanes and nuclear dust disks and what is their orientation and morphology; (4) is there evidence for merging, such as nuclear cusps or tidal tails; (5) are there differences in host galaxies of FR-I and FR-II sources; (6) what are the core profiles in nearby radio-loud galaxies; (7) what are the galaxy morphologies for redshifts in excess of one; (8) what are the morphologies of quasar hosts.

For the above reasons we undertook a snapshot survey of the 3CR radio sources using the Wide Field Planetary Camera 2 (WFPC2) during cycle 4. The "snapshot" mode of *HST* is designed to optimize scheduling efficiencies and is well suited for observing of representative samples of objects.

By basing the survey on the 3CR catalog we have the opportunity to investigate radio galaxies over a wide range in redshift ($0 < z < 2.5$) and radio luminosity ($10^{41} - 10^{46}$ ergs s^{-1}). An extensive suite of complementary ground- and space-based observations exist for the 3CR sample.

At $z > 0.6$ the UV continua of powerful radio galaxies are closely aligned with their radio sources (McCarthy, van Breugel, & Spinrad 1987; Chambers, Miley, & van Breugel 1987). The orientations at lower redshift and lower radio luminosity have been studied in detail with claims of both minor and major axis alignments with respect to the radio lobes. The *HST* snapshot sample offers an opportunity to look at the alignment effect at high resolution, in the interesting "transition" redshift range from $z < 0.1$ out to $z > 1$, where the effect becomes important.

We know from ground-based observations that the most luminous radio galaxies at high redshifts have disturbed morphologies (e.g., Heckman, van Breugel, & Miley 1986), and at the highest redshifts the optical continuum is highly elongated and rather irregular (McCarthy et al. 1987; Chambers et al. 1987). The higher angular resolution of *HST* may give clues as to whether these peculiarities originate in collisions and the merging of galaxies.

At low redshifts, dust and gas in active galaxies are very common, and gas disks seem to play a fundamental role in the triggering of a radio source (e.g., Kotanyi & Ekers 1979; Baum & Heckman 1989; Baum, Heckman, & van Breugel 1992). With *HST* it is possible to investigate dust out to a substantial redshift. For example, in the observations described here, there is clear evidence of dust and dust lanes out to a redshift of $z \approx 0.5$.

Optical synchrotron jets, if present, can be seen in *HST* images (e.g., Crane et al. 1993; Sparks, Biretta, & Macchetto 1994; Sparks et al. 1995). Because of the extremely short lifetimes of energetic particles responsible for optical synchrotron emission (100–1000 yr for M87; see Owen, Hardee, & Bignell 1980; Biretta, Stern, & Harris 1991; Meisenheimer 1991) we can pin down the acceleration sites and perhaps determine the internal jet structure. We may also investigate the relationship between dust and gas disks and the propagation of jets, both optical and radio.

As of 1995 August 30, we observed 267 sources in a redshift range from 0.0031 (3C 272.1) to 2.474 (3C 257). In cycle 5 we will be observing 100 3CR sources under a separate WFPC2 program using narrowband observations to produce images in optical line emission. A VLA snapshot

[1] Space Telescope Science Institute, 3700 San Martin Drive, Baltimore, MD 21218.
[2] Leiden Observatory, P.O. Box 9513, NL-2300 RA Leiden, The Netherlands.
[3] Observatories of the Carnegie Institution of Washington, 813 Santa Barbara Street, Pasadena CA 91101.

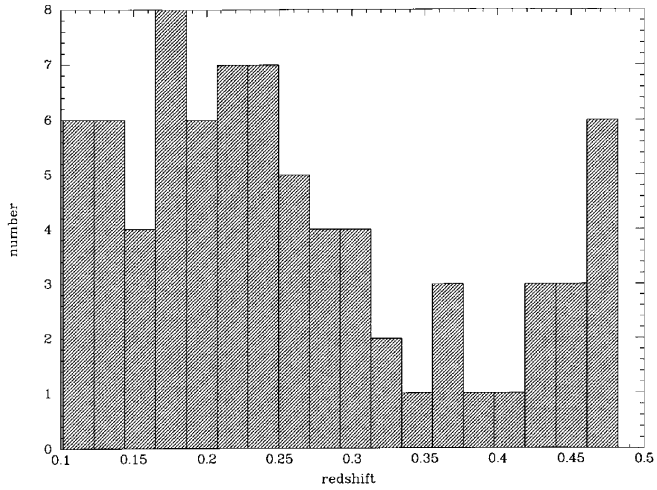

FIG. 1.—Redshift distribution for the radio galaxies presented here

survey has been undertaken using the A array to produce radio images at comparable resolution to our optical data for those sources for which such data were not available.

For the purpose of presentation and analysis we have divided the total sample into four subsets: radio galaxies at

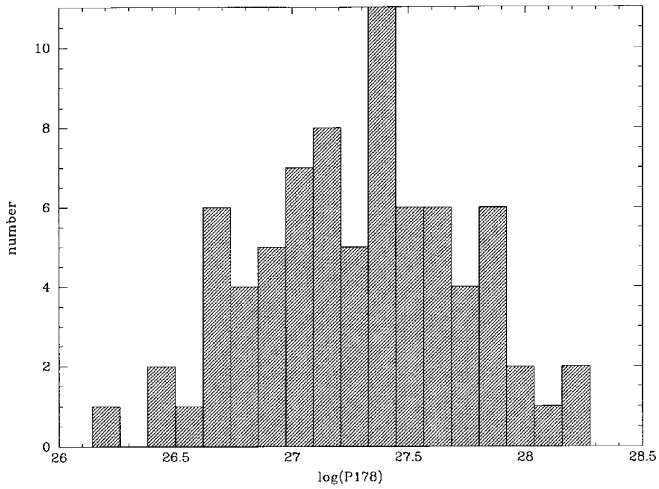

FIG. 2.—Radio power (at 178 MHz) distribution for the radio galaxies presented here.

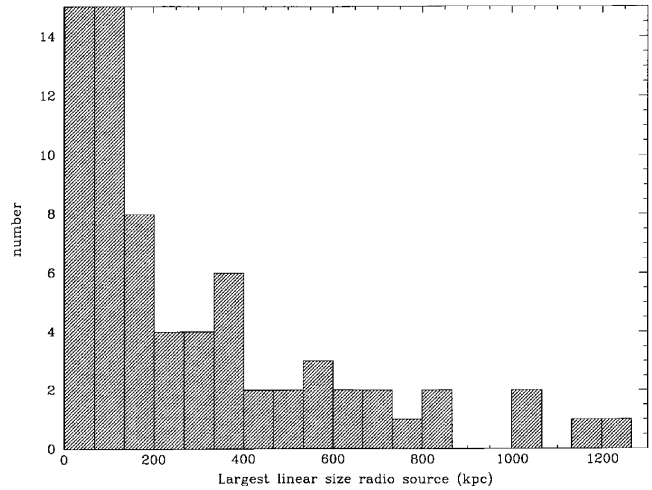

FIG. 3.—Radio largest linear size distribution for the radio galaxies presented here.

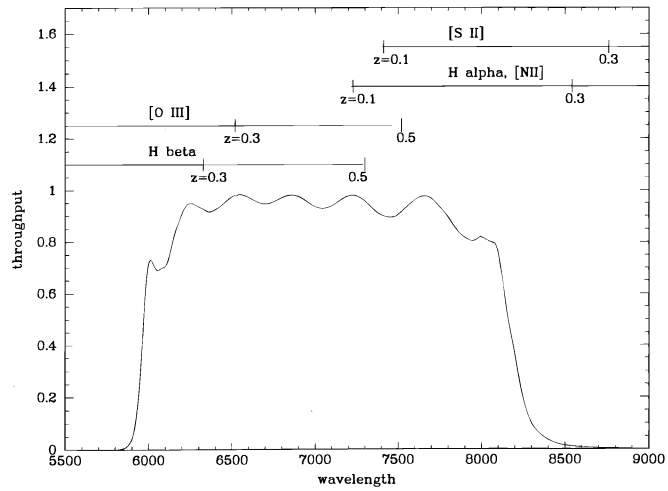

FIG. 4.—Most important line contaminations for the F702W filter for the redshift range $0.1 < z < 0.5$.

low ($0 < z < 0.1$) redshifts, radio galaxies at intermediate ($0.1 < z < 0.5$) redshifts, radio galaxies at high ($z > 0.5$) redshifts, and quasars. Companion papers present the WFPC2 snapshot images of the 3C radio galaxies in the redshift range $0 < z < 0.1$ (Baum et al. 1996) and $z > 0.5$ (McCarthy et al.). Future papers will discuss the statistical analysis, and will address specific topics such as dust, compact steep-spectrum sources, optical jets, and the alignment effect.

In this paper we describe the sample selection, observations, and data reduction for the intermediate-redshift subset.

2. SAMPLE SELECTION

As a basis for the *HST* snapshot program, we use the revised 3CR as defined by Bennett (1962a, 1962b): $S(178) > 9$ Jy and $\delta > -5$, with the additional constraint that $b > 10°$. All sources have been identified optically, and redshifts have been measured for all but two sources (Spinrad et al. 1985; Djorgovski et al. 1988). The completeness properties of the 3CR are discussed by Laing, Riley, & Longair (1985). However, several targets were excluded from the snapshot sample because of duplications with other *HST* programs, and several more were not observed because of scheduling practicalities. In total, during cycle 4 we observed 267 3CR sources.

The intermediate-redshift galaxies discussed here comprise 77 radio galaxies with $0.1 < z < 0.5$. The sources are listed in Table 1. The 3CR contains 85 sources in that redshift range; hence, the observations are 91% complete.

The redshift, radio power, and radio linear size distributions are shown in Figures 1, 2, and 3 for this sample, respectively. For references to the sources of this information see Table 2.

3. OPTICAL IMAGING

3.1. *Observations*

Table 1 summarizes the observations. Typically we obtained short, 2–5 minutes, fine lock guided images taken with the Planetary Camera (PC) relay of the WFPC2. The PC utilizes an 800 × 800 pixel Loral CCD as detector, with pixel size 0.″0455 (Burrows et al. 1995; Trauger et al. 1994). The expected tracking accuracy for fine lock guidance is ≈3 mas rms. The broadband F702W filter, close to Cousins *R*,

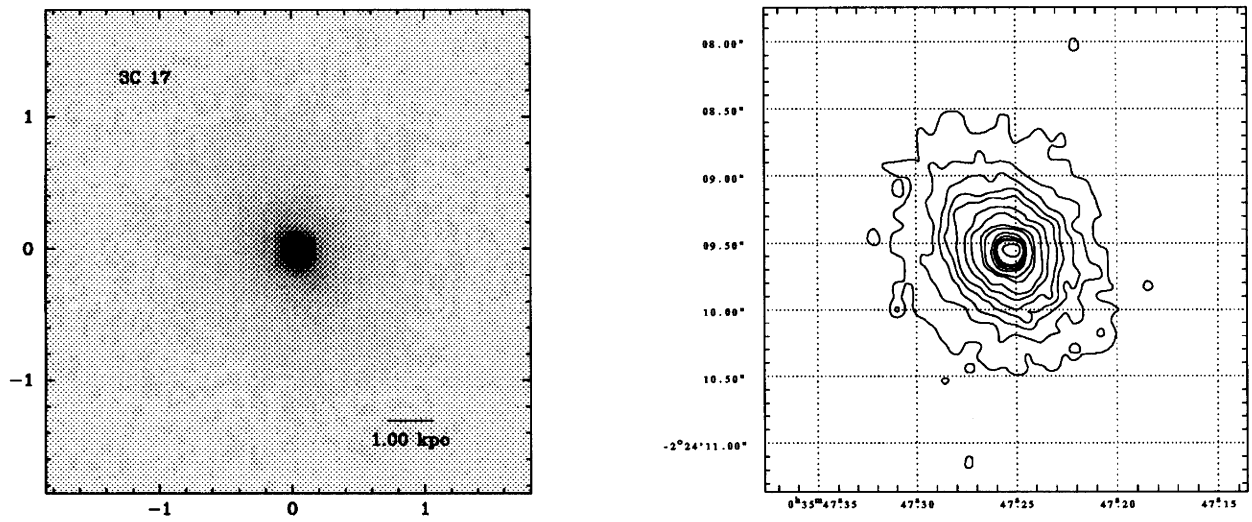

FIG. 5.—(*Left*) 3C 17, $z = 0.2197$. (*Right*) Contour levels: 2, 3, 4, 5, 6, 8, 10, 15, 20, 40, 60, 80, 100, 200, 400 × 1.866 × 10^{-18} ergs s^{-1} cm^{-2} $Å^{-1}$ $pixel^{-1}$.

is used throughout. This filter was chosen to give maximum sensitivity while recognizing that it would often include contributions from both line and continuum emission. We regarded this to be the optimum filter for finding interesting structures which could later be followed up in detail.

In the redshift range considered here the image may include a contribution from emission-line gas from [S II], Hα, [N II], [O III], and Hβ, as shown in Figure 4.

3.2. *Data Processing*

We used the calibrated data produced by the STScI reduction pipeline. For the WFPC2 the pipeline performs six actions: it makes a "bad-pixel map" (this identifies known static defects in the instrument), corrects the value of each pixel for the analog-to-digital conversion error, subtracts the bias level, performs a dark correction, performs the flat-field correction, and determines the absolute sensitivity (Baum et al. 1994). Subsequent reductions were carried out using the NOAO Image Reduction and Analysis Facility (IRAF) software package and the Space Telescope Science Data Analysis System (STSDAS).

A limitation of WFPC2 images is caused by defects due to the impact of cosmic rays on the detections. For about half the objects we obtained two exposures per object, making the cosmic-ray removal easier. The IRAF task "stsdas.crrej" was used to remove the cosmic rays by comparing and combining the different images. This task is designed to take multiple exposures of a given field and combine the images while rejecting very high counts in each pixel stack. Cosmic rays are selected in an iterative process as those pixels with values greater than $N \times \sigma$ [where N and σ are specified user parameters; we used $N = 4$, $\sigma = (5, 5, 4, 3)$]. These pixels are considered bad and are not used in the creation of the output, cosmic-ray–free image. This rejection process is iterative to allow the solution to achieve equilibrium slowly and allow for propagation of information about rejected pixels into adjacent pixels.

For the remaining objects we obtained only one exposure. For these images the cosmic rays were removed using the IRAF task "cosmicrays." This task detects cosmic-ray events in the input image and replaces them by the average number of counts in the four neighboring pixels. For these images it was sometimes necessary to remove missed cosmic rays manually, using the "imedit" IRAF task to replace the

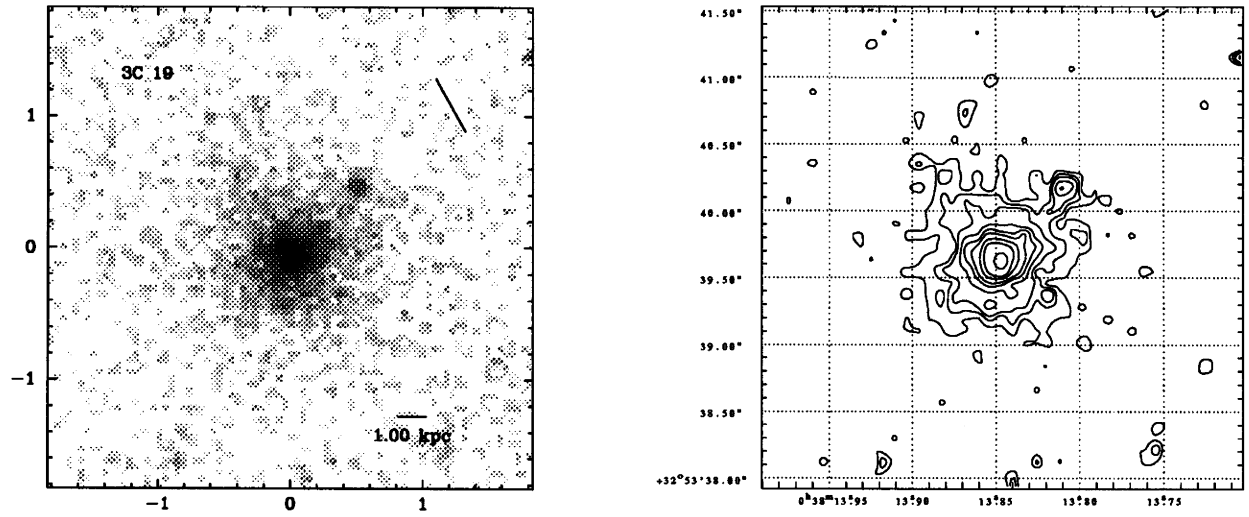

FIG. 6.—(*Left*) 3C 19, $z = 0.482$. (*Right*) Contour levels: 2, 3, 4, 5, 6, 8, 10, 15, 20, 40, 60 × 1.866 × 10^{-18} ergs s^{-1} cm^{-2} $Å^{-1}$ $pixel^{-1}$.

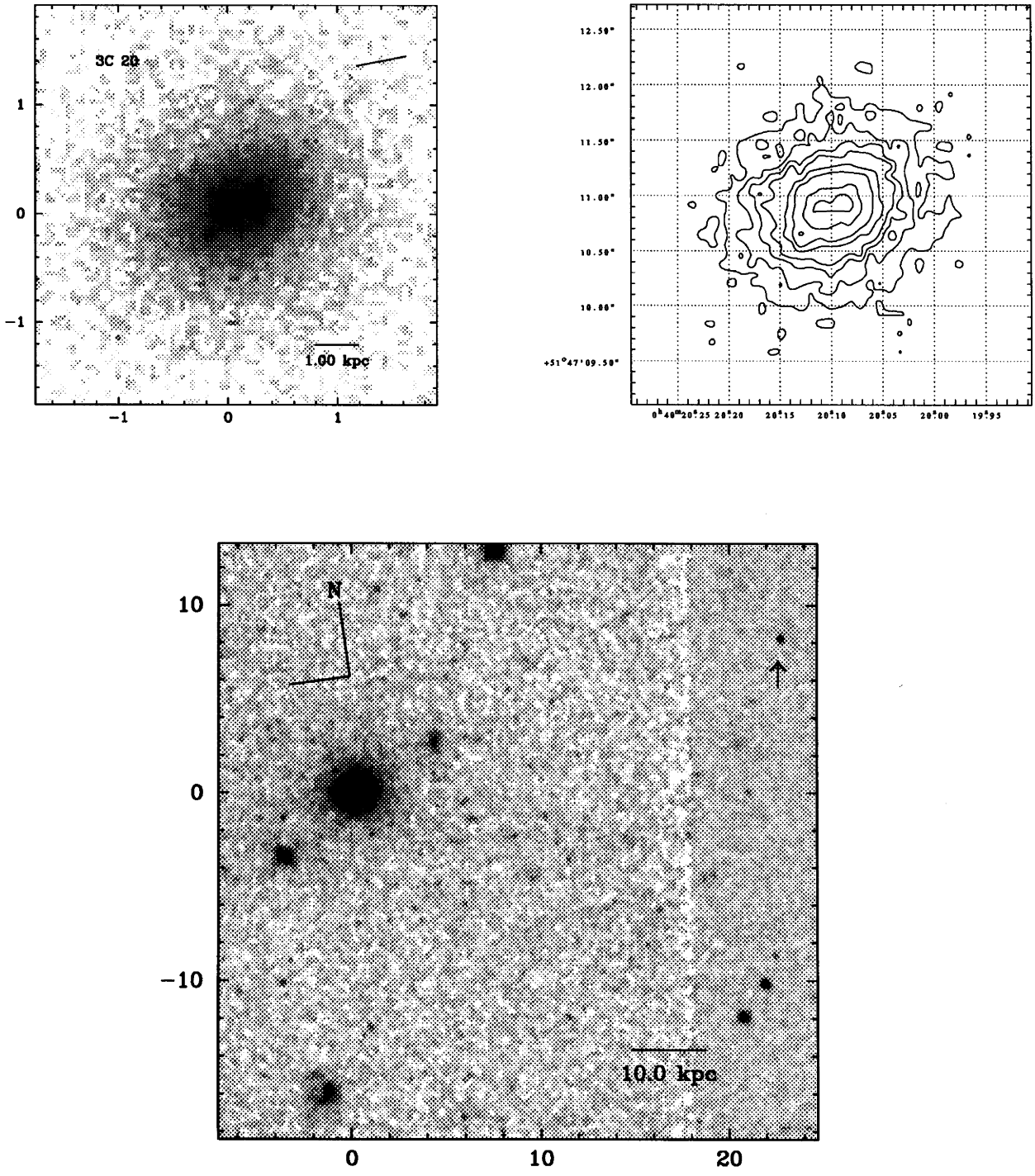

FIG. 7.—(*Left*) 3C 20, $z = 0.174$. (*Right*) Contour levels: (*Bottom*) 3, 4, 5, 6, 8, 10, 15, 20, 40, 60 × 1.866 × 10^{-18} ergs s^{-1} cm^{-2} $Å^{-1}$ $pixel^{-1}$. (*Bottom*) The arrow indicates the position of the optical hotspot.

bad pixel by the average of the surrounding pixels. Although this generally worked well, occasionally residual cosmic-ray defects remained.

We precessed the image coordinate frames to equinox B1950 to facilitate comparison with radio data from the literature. The identification of the object was not always straightforward. Low-resolution optical images of the radio galaxy were sometimes used to identify the source. An approximate coordinate frame for the WFPC2 images is provided by image header information. Uncertainties of order $\sim 1''$ are present (Burrows et al. 1995). The coordinates of the emission peak of the radio galaxies as measured on the PC are given in Table 3.

3.3. *Analysis*

The data were flux-calibrated using a value for the F702W inverse sensitivity of 1.866 × 10^{-18} $ergs^{-1}$ cm^{-2} $Å^{-1}$ dn^{-1} ("dn" represents data numbers). For the purpose of presentation all images were rotated so that north points up and east to the left. Nonrotated images (which have less smoothing) were used for measurement purposes.

The magnitude, m, and average surface magnitude, μ, not

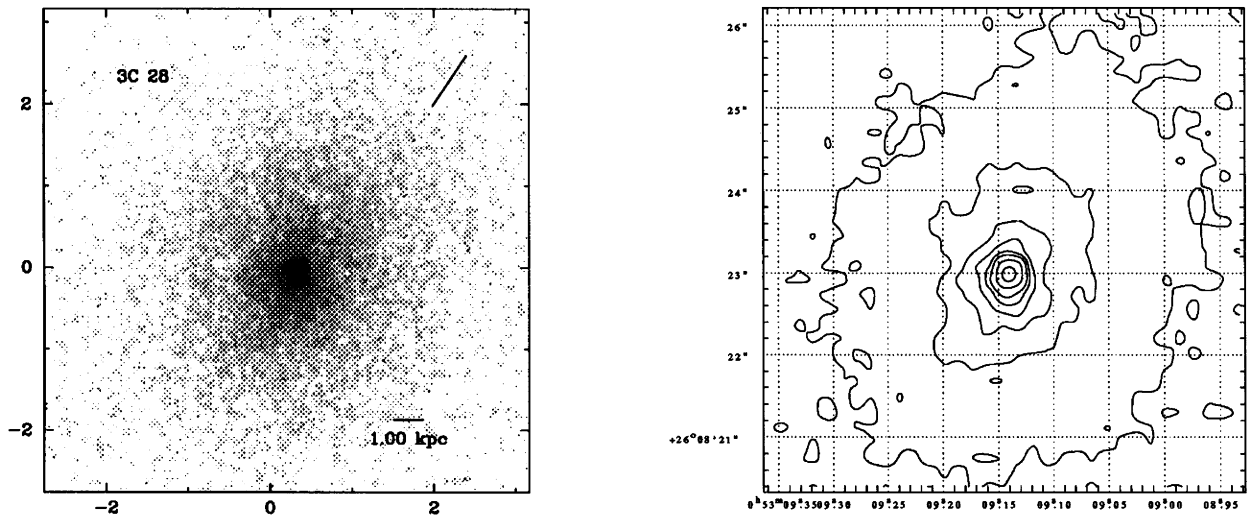

FIG. 8.—(*Left*) 3C 28, $z = 0.1952$. (*Right*) Contour levels: 1, 2, 3, 4, 5, 6, 8, 10, 15 × 1.866 × 10^{-18} ergs s^{-1} cm^{-2} $Å^{-1}$ $pixel^{-1}$.

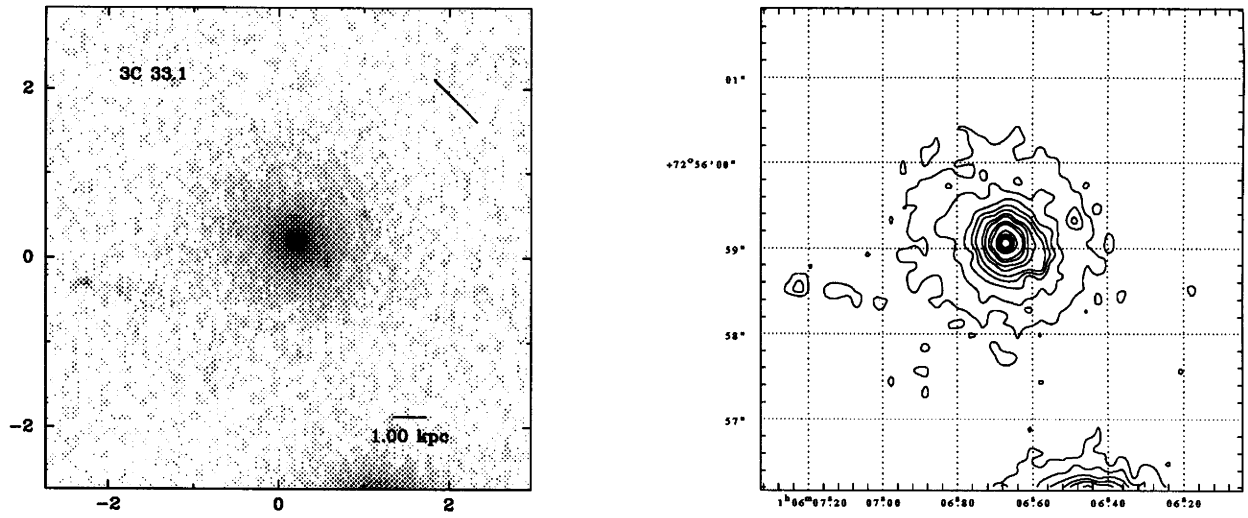

FIG. 9.—(*Left*) 3C 33.1, $z = 0.181$. (*Right*) Contour levels: 2, 3, 4, 5, 6, 8, 10, 15, 20, 40, 60, 80, 100, 200 × 1.866 × 10^{-18} ergs s^{-1} cm^{-2} $Å^{-1}$ $pixel^{-1}$.

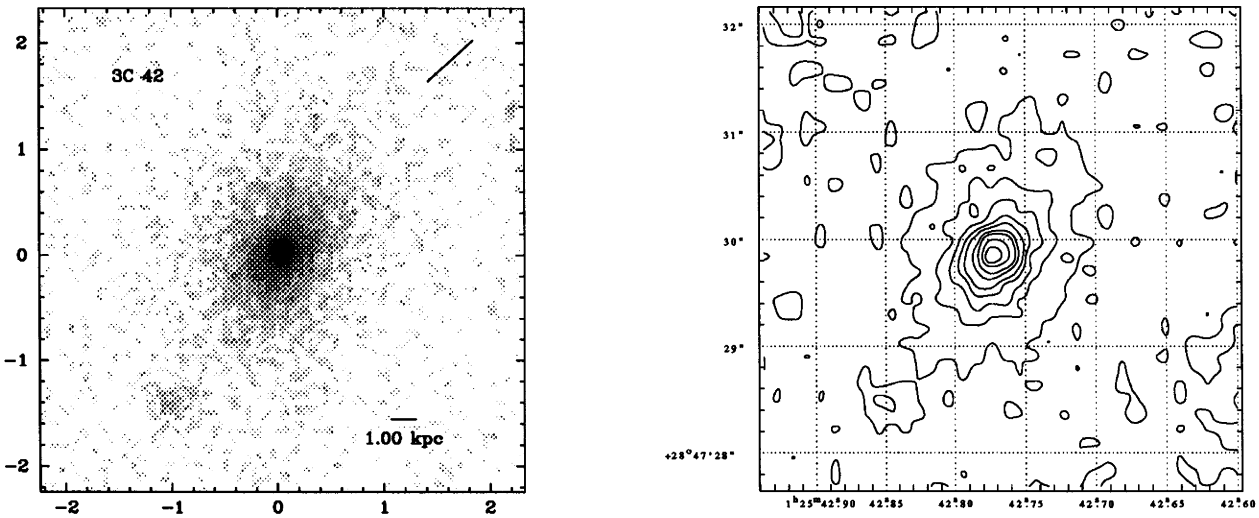

FIG. 10.—(*Left*) 3C 42, $z = 0.395$. (*Right*) Contour levels: 1, 2, 3, 4, 5, 6, 8, 10, 15, 20 × 1.866 × 10^{-18} ergs s^{-1} cm^{-2} $Å^{-1}$ $pixel^{-1}$.

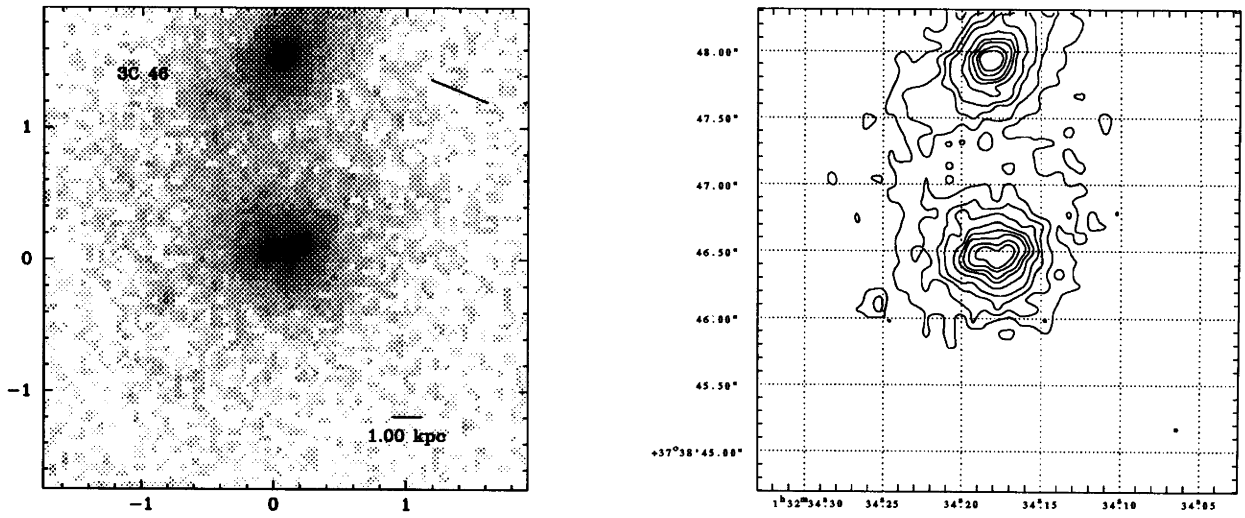

FIG. 11.—(*Left*) 3C 46, $z = 0.4373$. (*Right*) Contour levels: 3, 4, 5, 6, 8, 10, 12, 16, 20 × 1.866 × 10^{-18} ergs s^{-1} cm^{-2} $Å^{-1}$ $pixel^{-1}$.

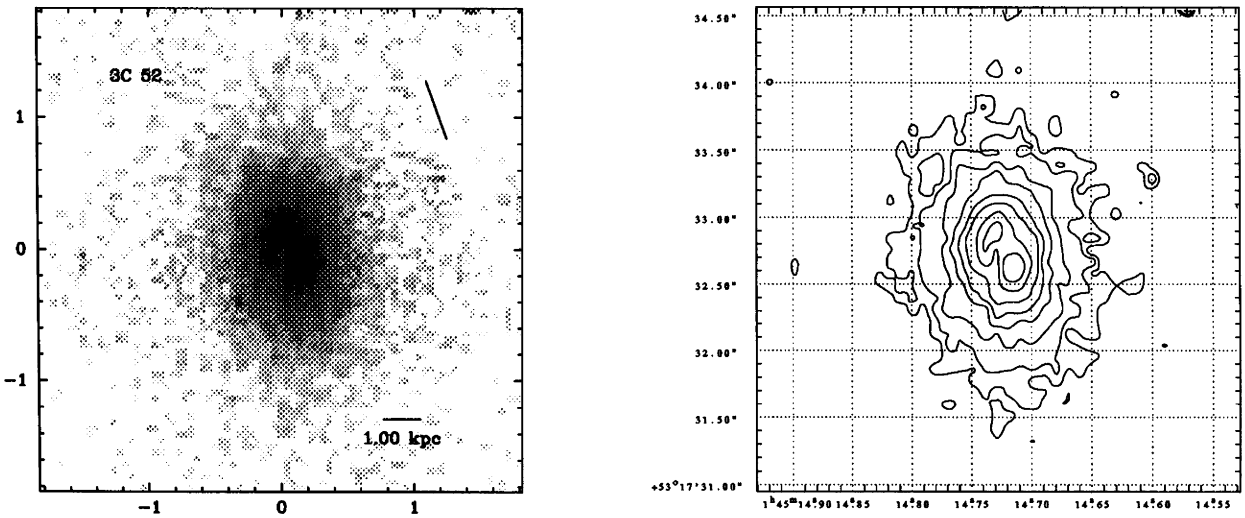

FIG. 12.—(*Left*) 3C 52, $z = 0.2854$. (*Right*) Contour levels: 1.5, 2, 3, 4, 5, 6, 8, 10, 12, 15, 20 × 1.866 × 10^{-18} ergs s^{-1} cm^{-2} $Å^{-1}$ $pixel^{-1}$.

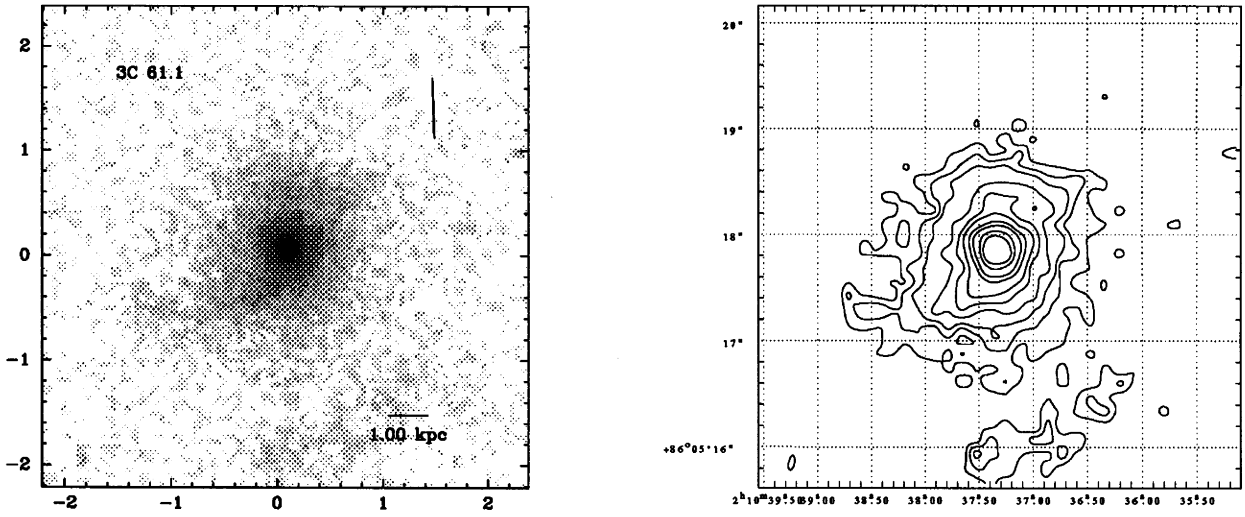

FIG. 13.—(*Left*) 3C 61.1, $z = 0.186$. (*Right*) Contour levels: 2, 2.5, 3, 4, 5, 6, 8, 10, 15, 20, 40 × 1.866 × 10^{-18} ergs s^{-1} cm^{-2} $Å^{-1}$ $pixel^{-1}$.

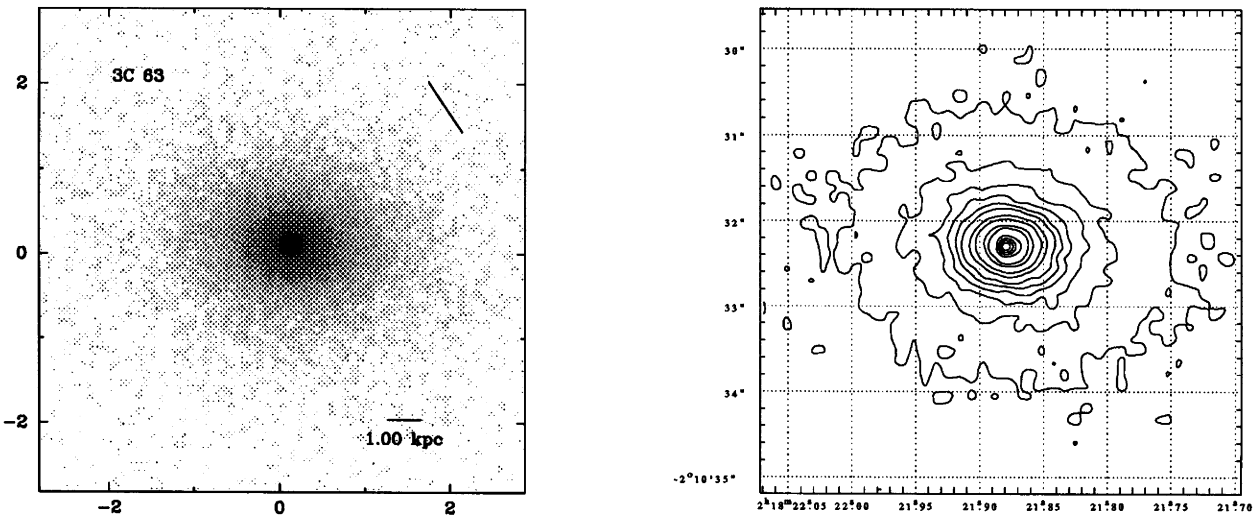

FIG. 14.—(*Left*) 3C 63, $z = 0.175$. (*Right*) Contour levels: 1, 2, 3, 4, 5, 6, 8, 10, 15, 20, 40, 60, 80, 100, 200 × 1.866 × 10^{-18} ergs s^{-1} cm^{-2} $Å^{-1}$ $pixel^{-1}$.

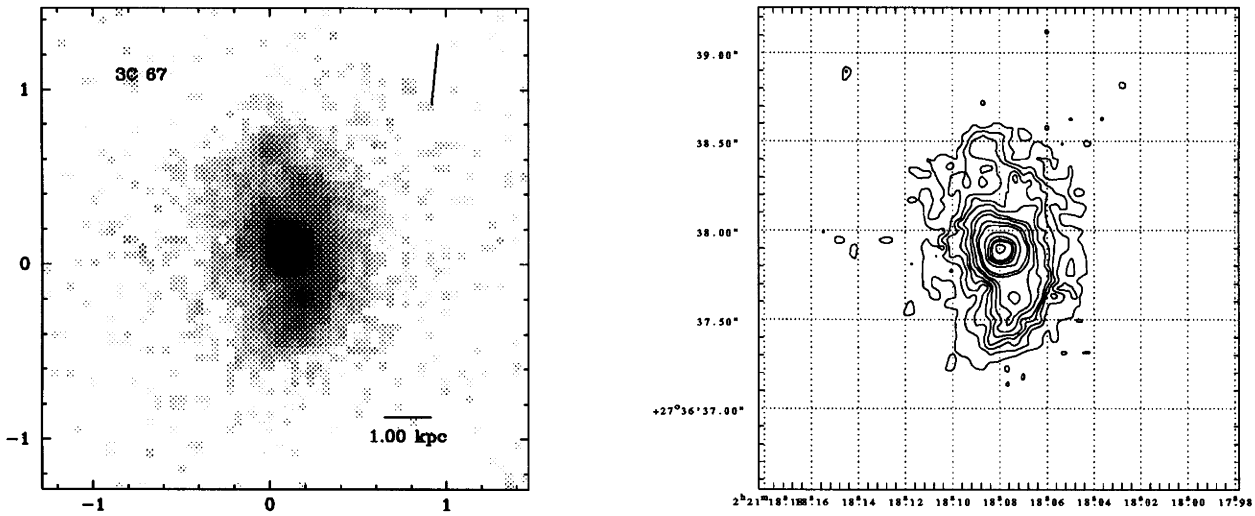

FIG. 15.—(*Left*) 3C 67, $z = 0.3102$. (*Right*) Contour levels: 1, 2, 3, 4, 5, 6, 8, 10, 15, 20, 40, 60, 80, 100, 200 × 1.866 × 10^{-18} ergs s^{-1} cm^{-2} $Å^{-1}$ $pixel^{-1}$.

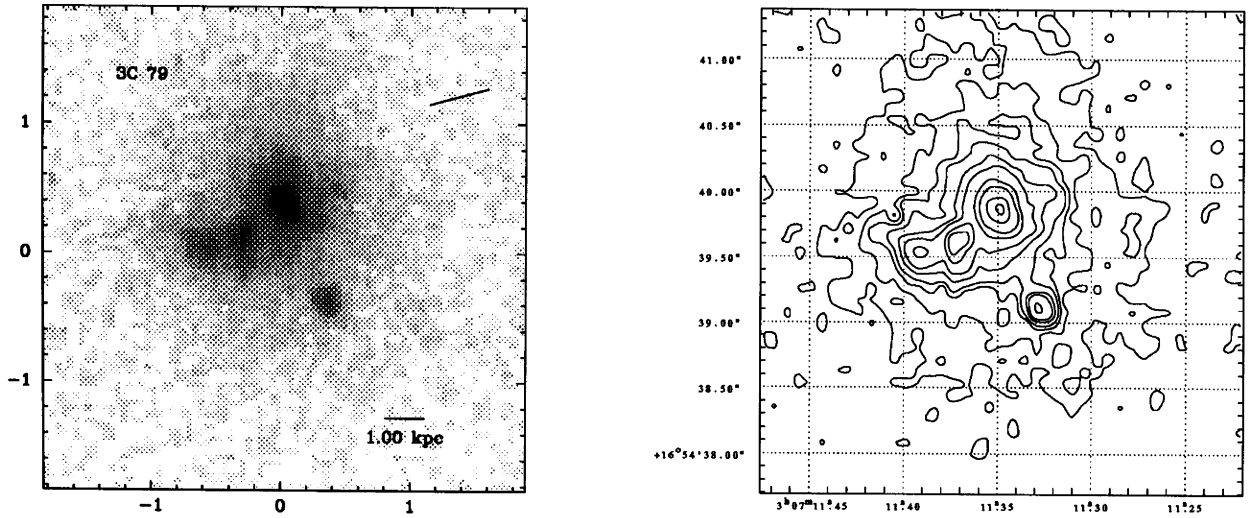

FIG. 16.—(*Left*) 3C 79, $z = 0.2559$. (*Right*) Contour levels: 3, 4, 5, 6, 8, 10, 15, 20, 40, 60 × 1.866 × 10^{-18} ergs s^{-1} cm^{-2} $Å^{-1}$ $pixel^{-1}$.

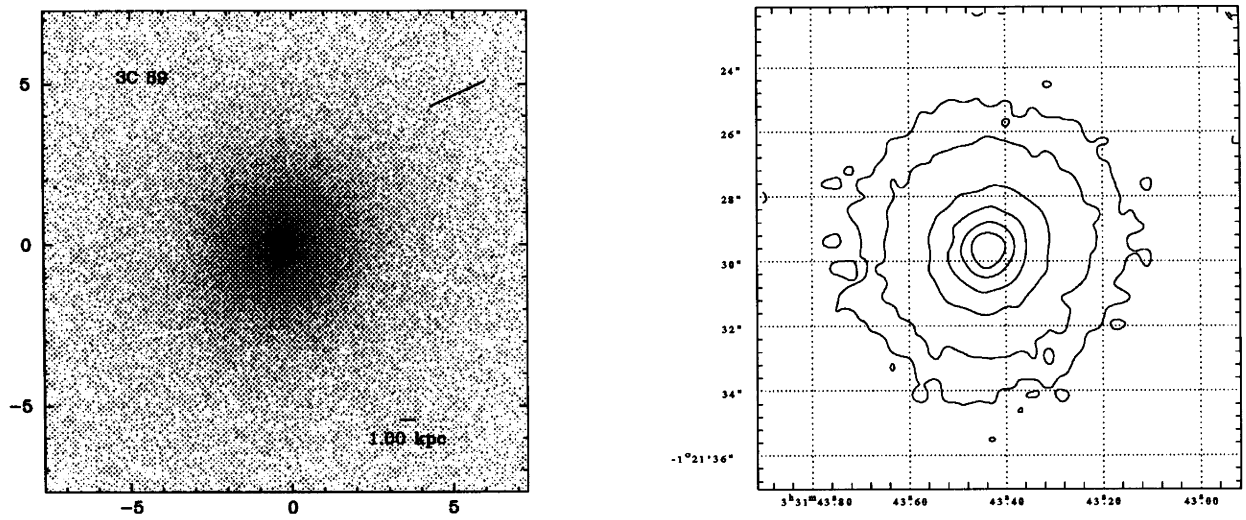

FIG. 17.—(*Left*) 3C 89, $z = 0.1386$. (*Right*) Contour levels: 1.7, 2, 3, 4, 5, 6, 8 × 1.866 × 10^{-18} ergs s^{-1} cm^{-2} $Å^{-1}$ $pixel^{-1}$.

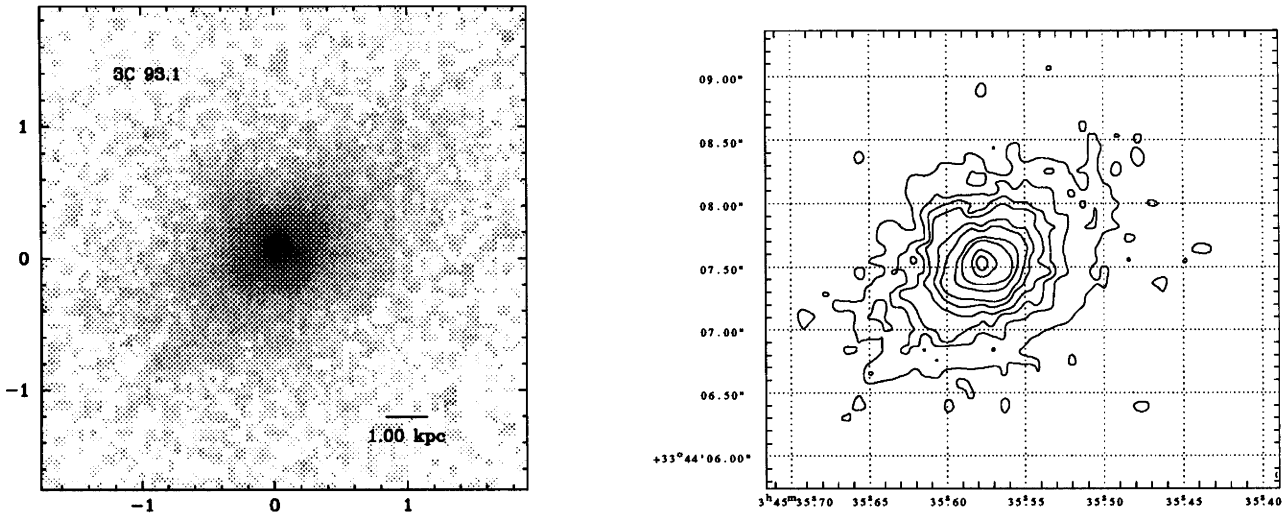

FIG. 18.—(*Left*) 3C 93.1, $z = 0.244$. (*Right*) Contour levels: 3, 4, 5, 6, 8, 10, 15, 20, 40, 60 × 1.866 × 10^{-18} ergs s^{-1} cm^{-2} $Å^{-1}$ $pixel^{-1}$.

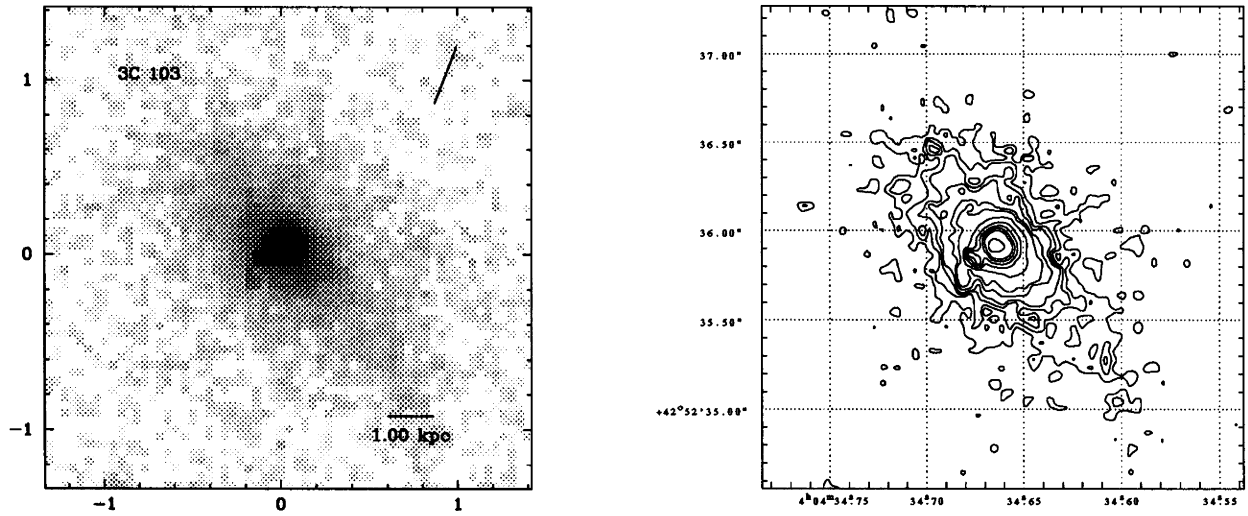

FIG. 19.—(*Left*) 3C 103, $z = 0.33$. (*Right*) Contour levels: 3, 4, 5, 6, 8, 10, 20, 40, 60, 80, 100, 200 × 1.866 × 10^{-18} ergs s^{-1} cm^{-2} $Å^{-1}$ $pixel^{-1}$.

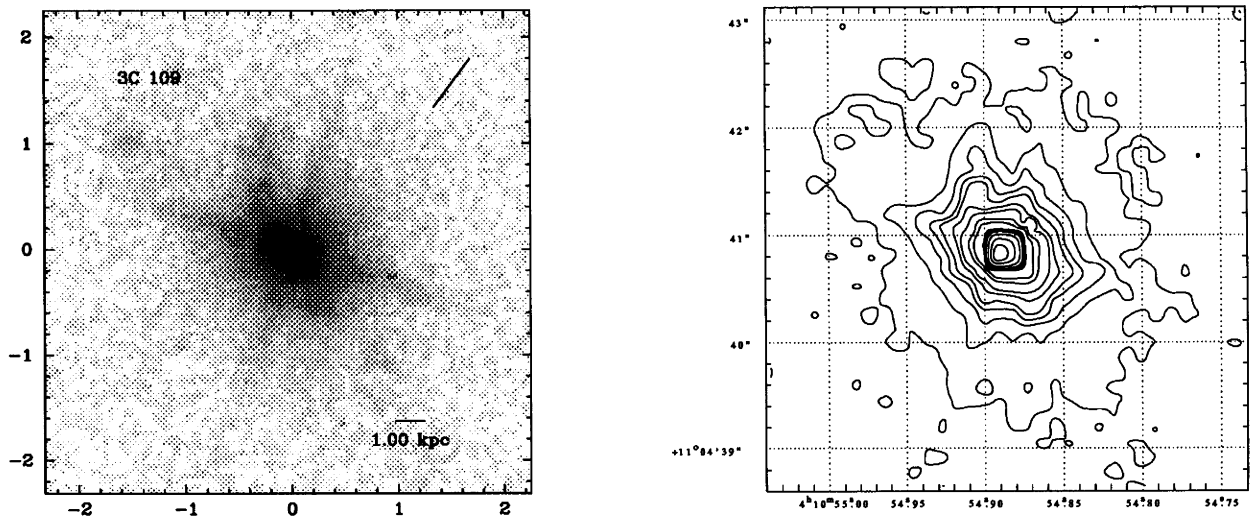

FIG. 20.—(*Left*) 3C 109, $z = 0.3056$. (*Right*) Contour levels: 2, 3, 4, 5, 6, 8, 10, 15, 20, 40, 60, 80, 100, 200, 400 × 1.866 × 10^{-18} ergs s^{-1} cm^{-2} $Å^{-1}$ $pixel^{-1}$.

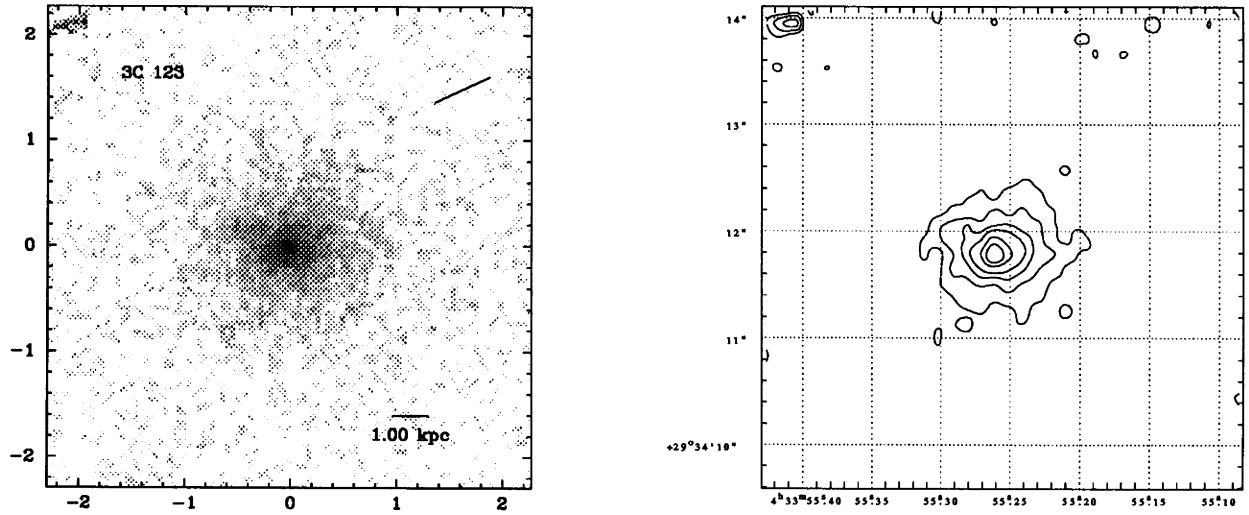

FIG. 21.—(*Left*) 3C 123, $z = 0.218$. (*Right*) Contour levels: 1, 3, 4, 5, 6, 8, 10, 15 × 1.866 × 10^{-18} ergs s^{-1} cm^{-2} $Å^{-1}$ $pixel^{-1}$.

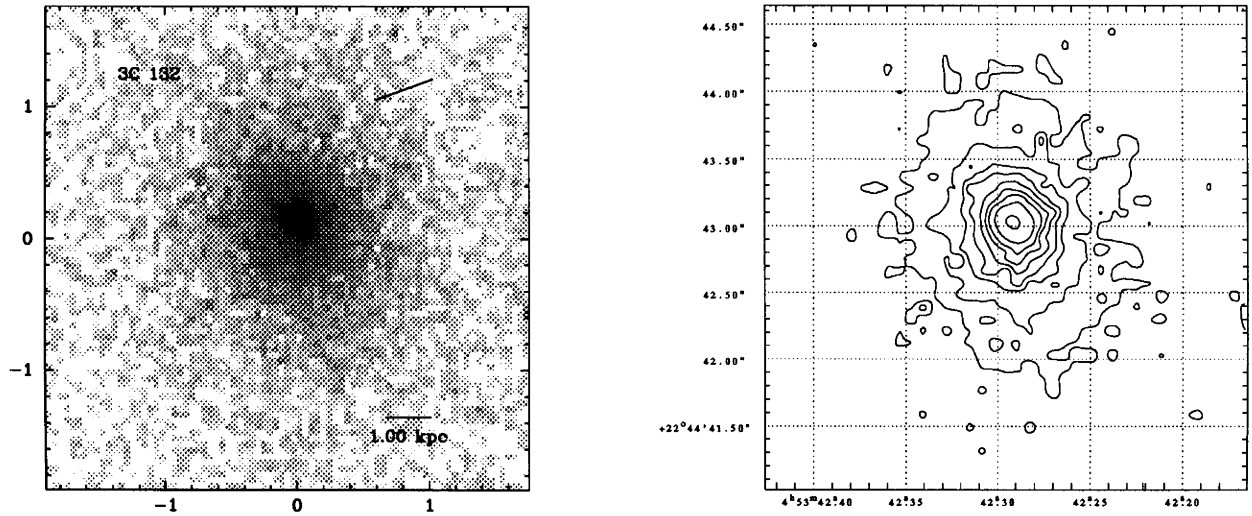

FIG. 22.—(*Left*) 3C 132, $z = 0.214$. (*Right*) Contour levels: 2, 3, 4, 5, 6, 8, 10, 15, 20, 40 × 1.866 × 10^{-18} ergs s^{-1} cm^{-2} $Å^{-1}$ $pixel^{-1}$.

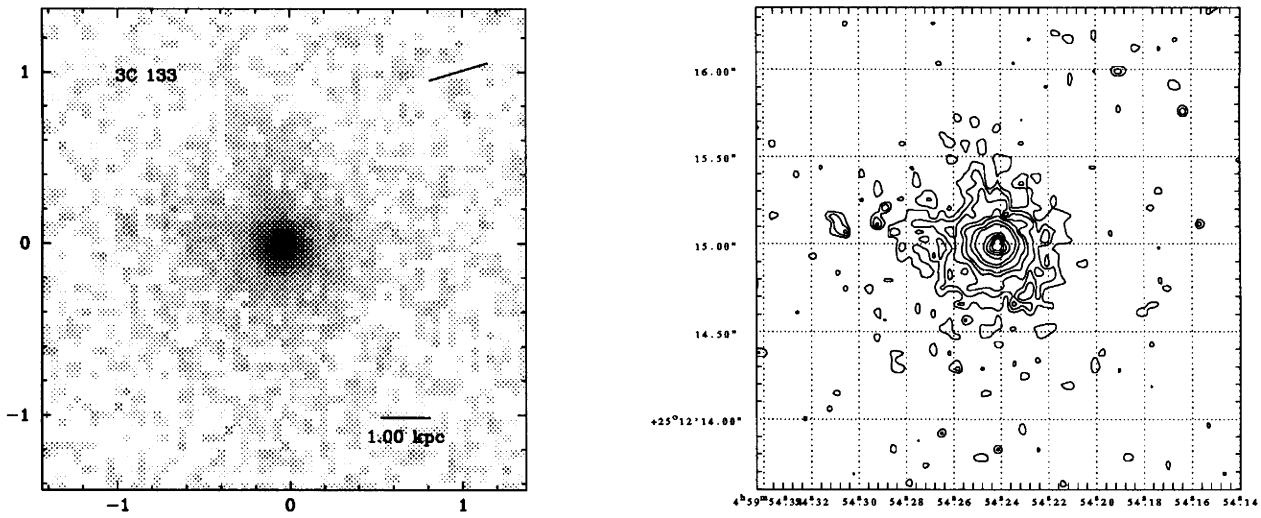

FIG. 23.—(*Left*) 3C 133, $z = 0.2775$. (*Right*) Contour levels: 4, 5, 6, 8, 10, 15, 20, 40, 60, 80, 100, 200 × 1.866 × 10^{-18} ergs s^{-1} cm^{-2} $Å^{-1}$ $pixel^{-1}$.

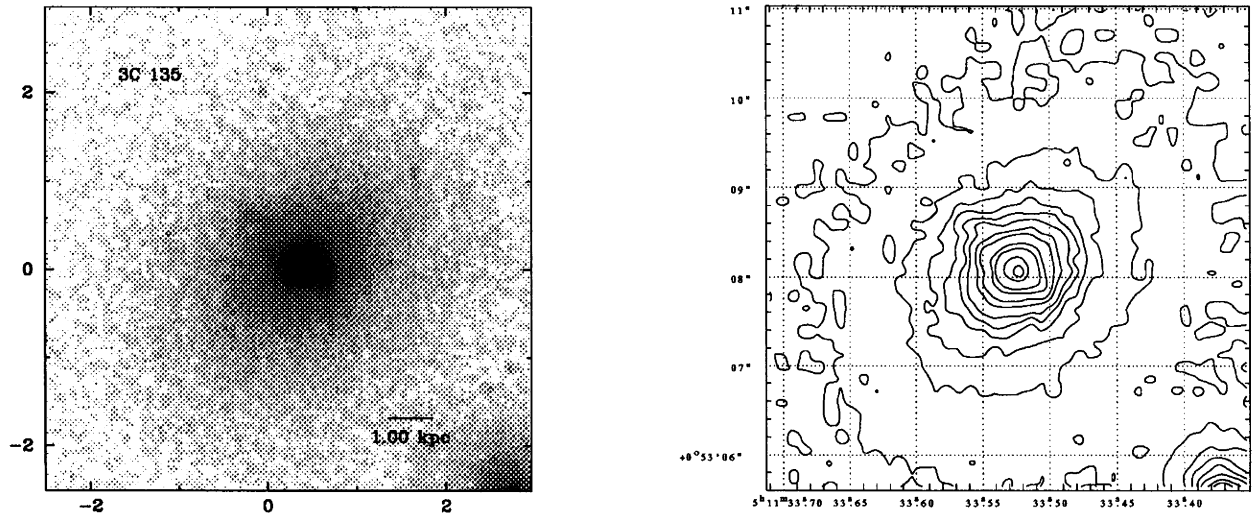

FIG. 24.—(*Left*) 3C 135, $z = 0.1273$. (*Right*) Contour levels: 1, 2, 3, 4, 5, 6, 8, 10, 15, 20, 40, 60 × 1.866 × 10^{-18} ergs s^{-1} cm^{-2} $Å^{-1}$ $pixel^{-1}$.

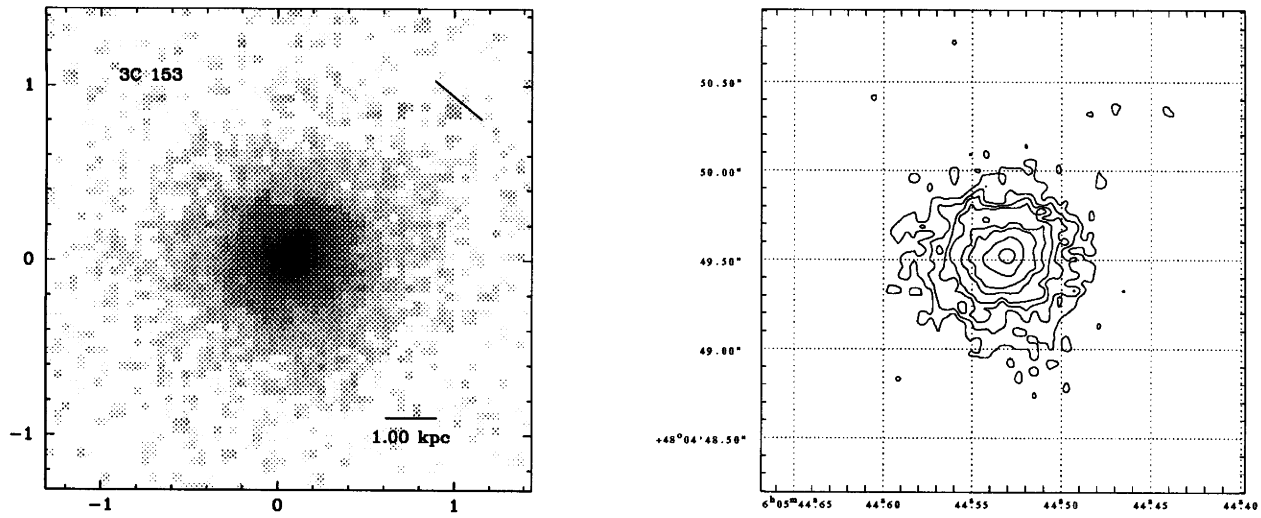

FIG. 25.—(*Left*) 3C 153, $z = 0.2769$. (*Right*) Contour levels: 2, 3, 4, 5, 6, 8, 10, 15, 20, 40, 60 × 1.866 × 10^{-18} ergs s^{-1} cm^{-2} $Å^{-1}$ $pixel^{-1}$.

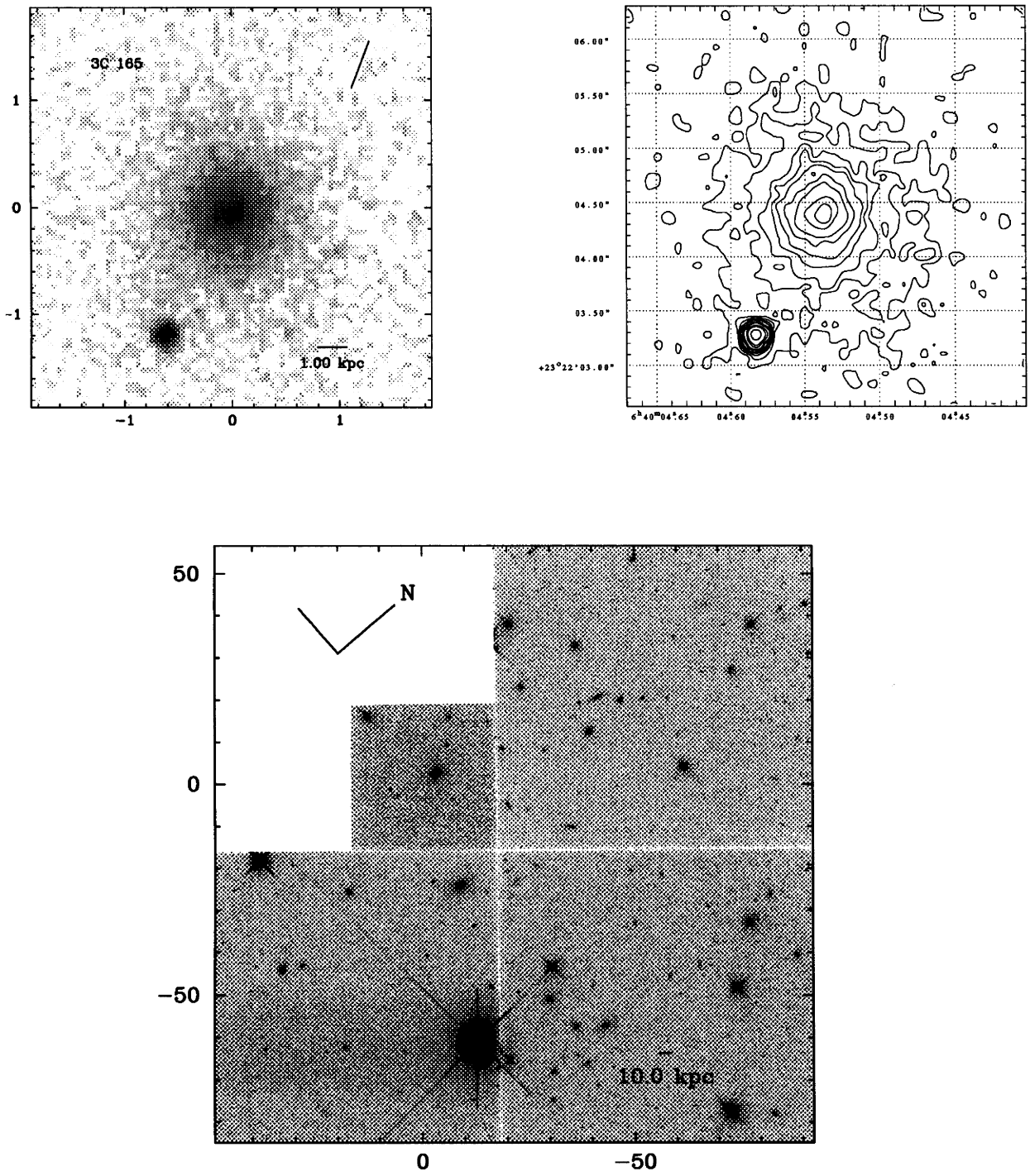

FIG. 26.—(*Left*) 3C 165, $z = 0.2957$. (*Right*) Contour levels: 2, 3, 4, 5, 6, 8, 10, 15, 20, 40 × 1.866 × 10^{-18} ergs s^{-1} cm^{-2} $Å^{-1}$ $pixel^{-1}$. (*Bottom*) Wide field.

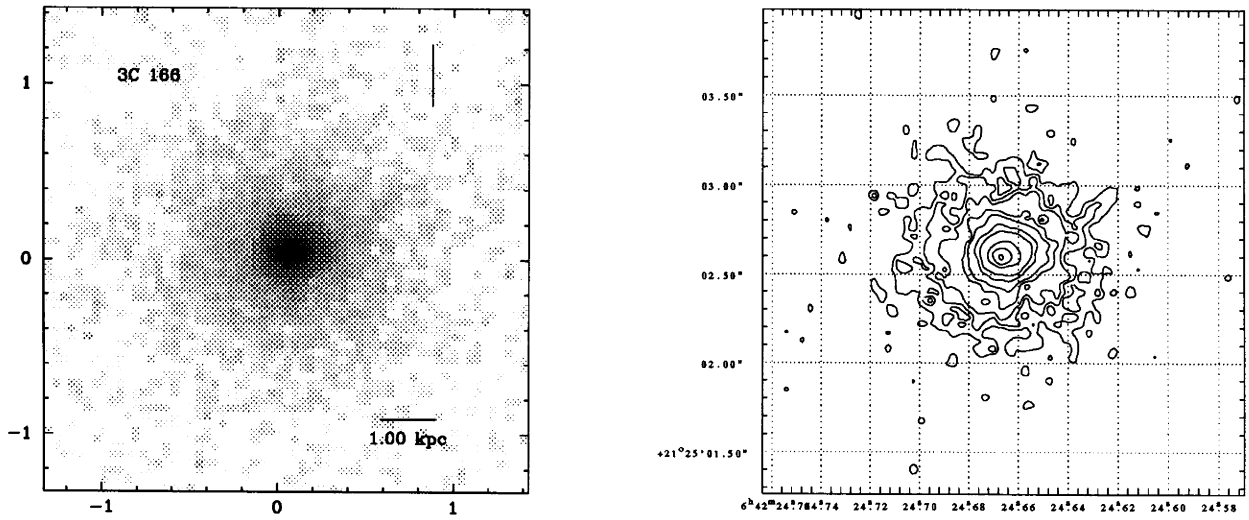

FIG. 27.—(*Left*) 3C 166, $z = 0.245$. (*Right*) Contour levels: 4, 5, 6, 8, 10, 15, 20, 40, 60, 80, 100 × 1.866 × 10^{-18} ergs s^{-1} cm^{-2} $Å^{-1}$ $pixel^{-1}$.

corrected for Galactic reddening, were determined, interior to an absolute surface brightness level of $8.0 \times 10^{-20} \times (1 + z)^{-4}$ ergs $^{-1}$ cm $^{-2}$ pixel $^{-1}$. The magnitude is given by the expression

$$m = -2.5 \log_{10} F + M(0) ,$$

where F is the measured flux and $M(0) = -21.1$, the zero point for the *HST* magnitude scale, normalized to Vega. The surface brightness, μ, in units of mag arcsec^{-2} is given by

$$\mu = -2.5 \log_{10} (S) + M(0) ,$$

where S is the measured surface brightness. In addition, magnitudes and surface magnitudes inside 15 kpc and 1 kpc radii were determined (m_{15}, m_1, μ_{15}, and μ_1, respectively).

The total error in the flux for the objects considered here is dominated by the uncertainty in the determination of the magnitude zero point $M(0)$. $M(0)$ is accurate to within 2% (Burrows et al. 1995). In addition, the photometry was done without correcting for the problem of the charge transfer efficiency of the Loral CCD. This will incorporate an extra error in flux up to 4% (Holtzman et al. 1995).

We measured the position angle on the sky of the largest extensions of the emission regions at a surface brightness level of $8.0 \times 10^{-20} \times (1 + z)^{-4}$ ergs $^{-1}$ cm $^{-2}$ pixel $^{-1}$ integrated over the F702W passband. The objects have sufficiently complex morphologies that, in many cases, the position angle is not particularly well defined. The uncertainty in the position angle measurements may be as large as $\approx 10°$–$15°$. We determined the ellipticities and largest angular size at the same surface brightness level. These values were determined manually because of the complexity of the objects. For example, some objects show extreme "lumpiness" in their emission (e.g., 3C 299, 3C 79). Sometimes it was not possible to determine the values for the ellipticity and position angle. The errors in ellipticity are less than 0.08, and the errors in largest angular size are less than 0.″2.

The results of the measurements of magnitudes, position angles, ellipticities, and largest angular sizes are summarized in Table 3.

4. INDIVIDUAL SOURCE DESCRIPTIONS

Gray-scale *HST* WFPC2 images and contour plots of radio galaxies with $0.1 < z < 0.5$ are shown in Figures 5–83.

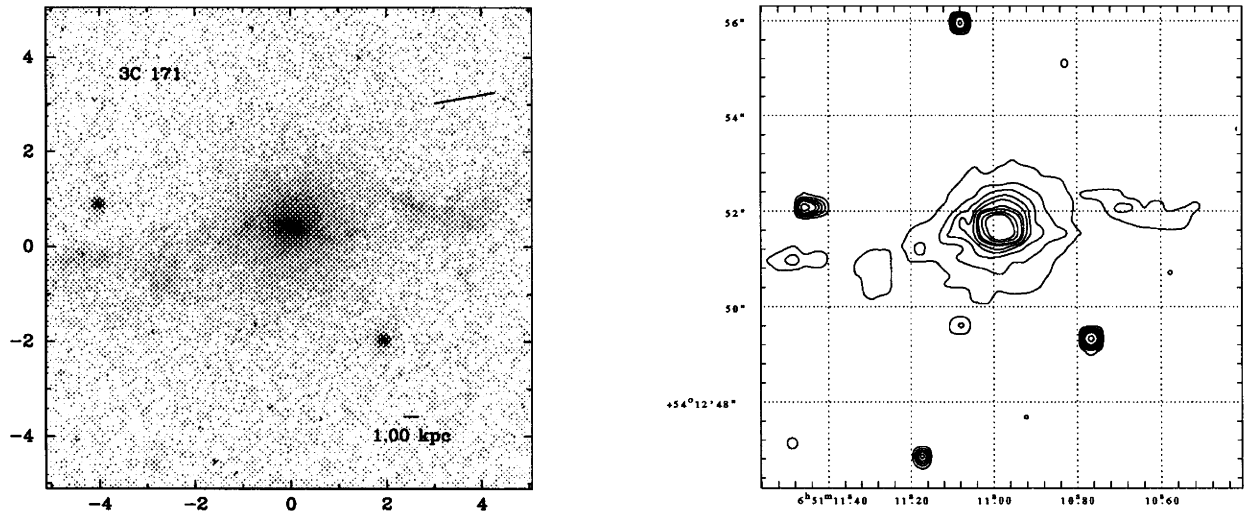

FIG. 28.—(*Left*) 3C 171, $z = 0.2384$. (*Right*) Contour levels: 2, 3, 4, 5, 6, 8, 10, 15, 20, 40 × 1.866 × 10^{-18} ergs s^{-1} cm^{-2} $Å^{-1}$ $pixel^{-1}$.

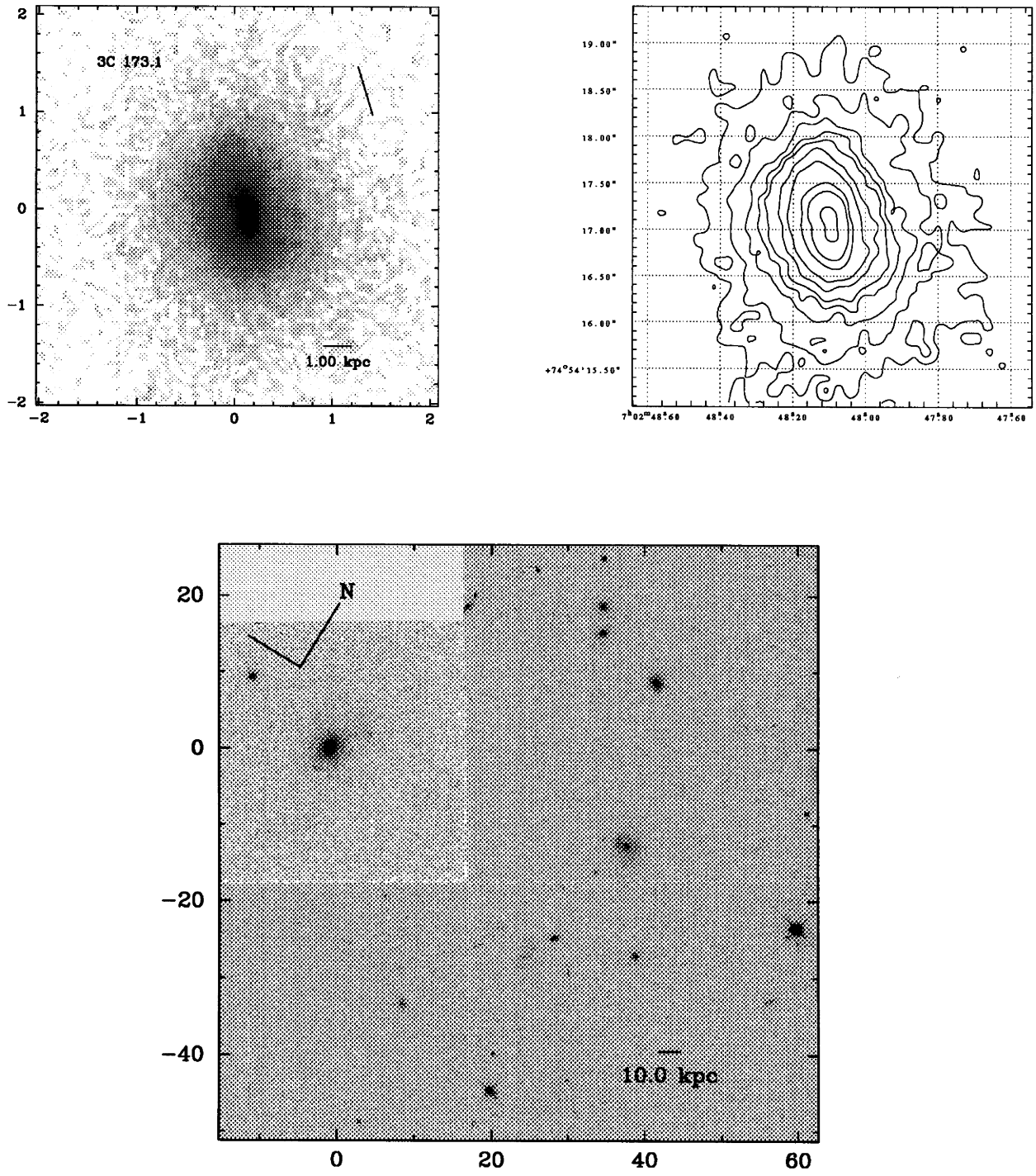

FIG. 29.—(*Left*) 3C 173.1, $z = 0.292$. (*Right*) Contour levels: 2.2, 3, 4, 5, 6, 8, 10, 15, 20, 40 × 1.866 × 10^{-18} ergs s^{-1} cm^{-2} $Å^{-1}$ $pixel^{-1}$. (*Bottom*) Wide field.

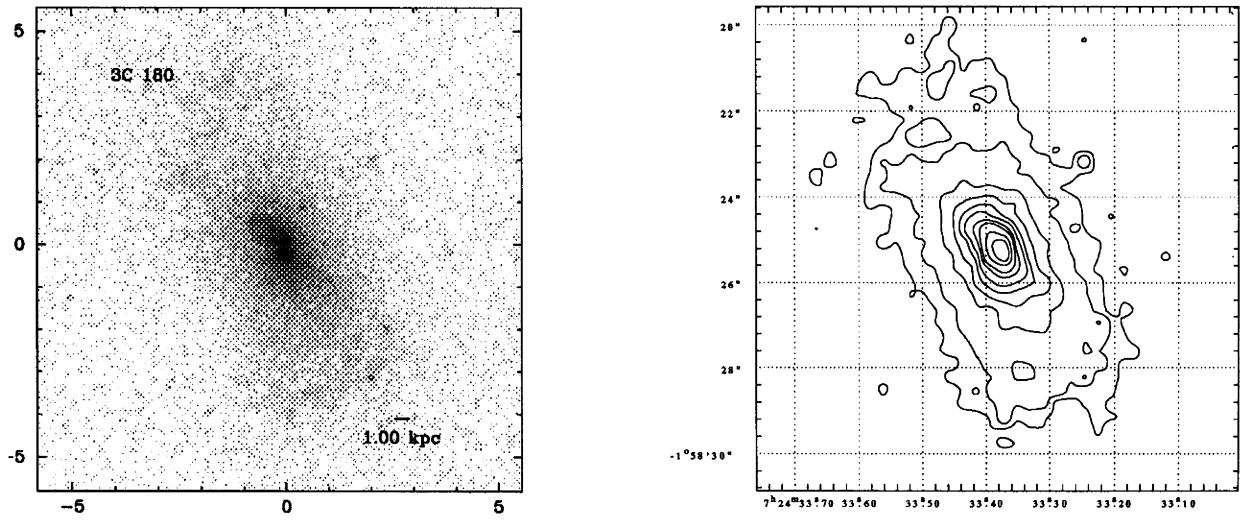

FIG. 30.—(*Left*) 3C 180, $z = 0.22$. (*Right*) Contour levels: 1.5, 2, 3, 4, 5, 6, 8, 10, 15, 20, 40 × 1.866 × 10^{-18} ergs s^{-1} cm^{-2} $Å^{-1}$ $pixel^{-1}$.

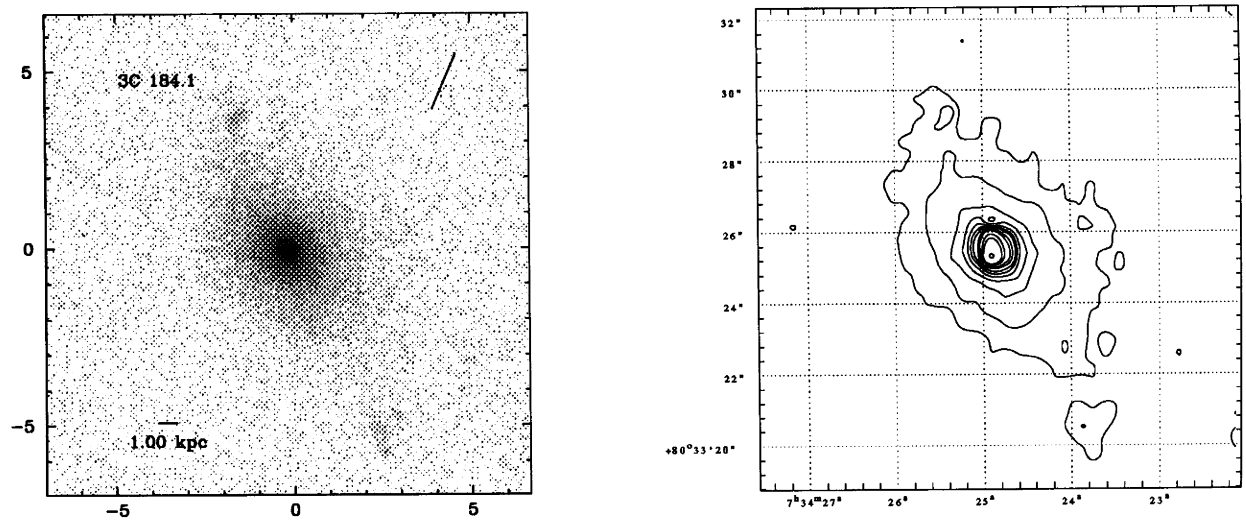

FIG. 31.—(*Left*) 3C 184.1, $z = 0.1182$. (*Right*) Contour levels: 0.5, 1, 2, 3, 4, 5, 6, 8, 10, 15, 20, 40, 60 × 1.866 × 10^{-18} ergs s^{-1} cm^{-2} $Å^{-1}$ $pixel^{-1}$.

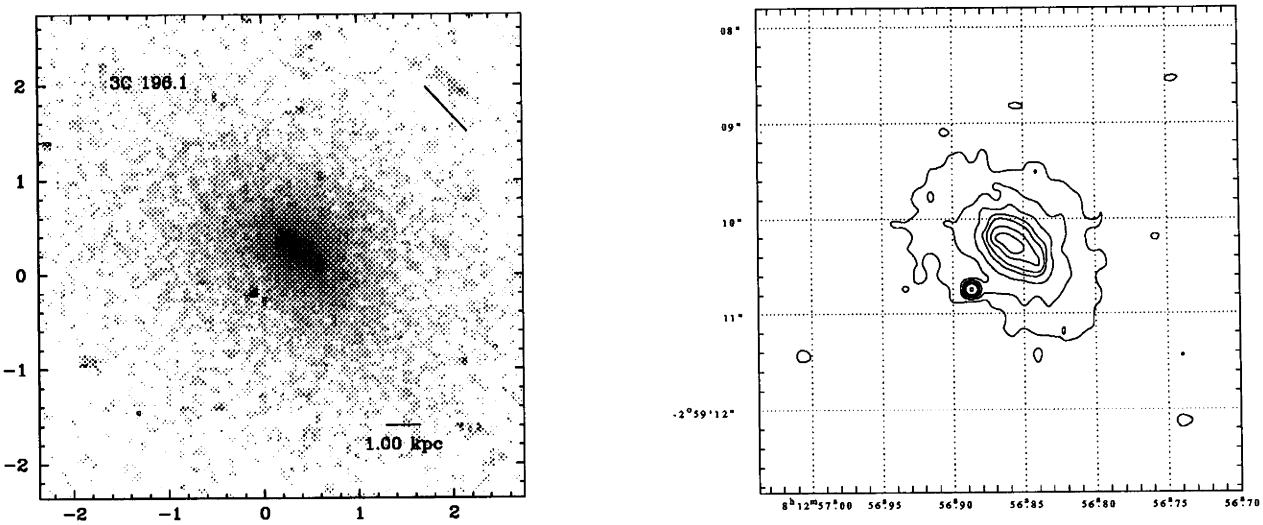

FIG. 32.—(*Left*) 3C 196.1, $z = 0.198$. (*Right*) Contour levels: 2, 3, 4, 5, 6, 8, 10, 15, 20 × 1.866 × 10^{-18} ergs s^{-1} cm^{-2} $Å^{-1}$ $pixel^{-1}$.

TABLE 1

OBSERVATION LOG: RADIO GALAXIES WITH $0.1 < z < 0.5$

3CR (1)	Date (2)	T (3)	N (4)
17.0	1994 Oct 10	280	2
19.0	1994 Jul 18	300	1
20.0	1995 Feb 20	300	1
28.0	1994 Oct 17	280	2
33.1	1995 Feb 13	300	1
42.0	1995 Jan 16	300	1
46.0	1995 Feb 13	300	1
52.0	1994 Aug 29	280	2
61.1	1995 May 01	300	1
63.0	1994 Oct 17	280	2
67.0	1994 Aug 15	280	2
79.0	1994 Mar 14	280	2
89.0	1994 Jun 27	280	2
93.1	1994 Sep 12	300	1
103.0	1995 Feb 06	300	1
109.0	1994 Jul 18	560	4
123.0	1994 Dec 19	300	1
132.0	1994 Dec 19	140	1
133.0	1994 Mar 07	300	1
135.0	1994 Sep 19	280	2
153.0	1994 May 02	280	2
165.0	1994 Feb 21	300	1
166.0	1994 Dec 19	300	1
171.0	1994 Mar 07	600	2
173.1	1994 Apr 25	300	1
180.0	1994 May 02	300	1
184.1	1994 Sep 05	280	2
196.1	1994 Feb 14	280	2
197.1	1994 Apr 25	280	2
200.0	1994 Apr 15	300	1
213.1	1994 Sep 19	300	1
219.0	1994 Feb 14	280	2
223.0	1994 Apr 25	280	2
223.1	1994 Apr 18	280	2
234.0	1994 Dec 26	280	2
244.1	1994 Apr 15	300	1
258.0	1994 Apr 25	300	1
268.2	1995 May 12	300	1
268.3	1994 Oct 10	300	1
274.1	1995 May 10	300	1
275.0	1994 Mar 07	300	1
277.0	1994 Apr 25	300	1
284.0	1994 Aug 15	280	2
287.1	1994 Apr 04	280	2
288.0	1995 Apr 30	280	2
299.0	1995 May 05	300	1
300.0	1995 Jan 10	140	1
303.0	1994 Nov 14	280	2
303.1	1994 Mar 28	300	1
306.1	1994 Apr 25	300	1
313.0	1995 Jan 16	300	1
314.1	1994 Dec 19	280	2
315.0	1994 Nov 28	280	2
319.0	1994 Apr 15	280	2
320.0	1995 Feb 06	280	2
327.0	1994 Apr 18	280	2
327.1	1994 Aug 15	300	1
332.0	1995 Apr 29	280	2
341.0	1994 Mar 28	300	1
346.0	1994 Aug 01	280	2
348.0	1994 May 09	280	2
349.0	1994 Sep 19	300	1
357.0	1995 Jan 23	280	2
379.1	1994 Feb 07	280	2
381.0	1995 Feb 06	280	2
401.0	1994 Sep 05	300	1
410.0	1994 Jun 20	300	1
411.0	1995 May 04	300	1
424.0	1994 Sep 05	280	2
433.0	1995 Apr 26	280	2
434.0	1994 Aug 29	300	1
435.A	1994 Oct 24	300	1
436.0	1994 Sep 19	280	2
438.0	1994 Dec 12	300	1
456.0	1994 Aug 22	300	1
459.0	1994 Oct 10	280	2
460.0	1994 Jul 18	300	1

NOTES.—Col. (1) = 3CR number; col. (2) = observation date; col. (3) = total integration time per object; col. (4) = number of subexposures.

The numbers on both horizontal and vertical axes of the gray-scale images refer to distance in arcseconds. All image intensity levels are plotted logarithmically except for 3C 258 and 3C 274.1, for which they are plotted linearly. The arrow in the upper right corner of the figures indicates the *direction* of the radio source axis from the literature. For images not showing this arrow, no value for the radio source axis was found in the literature. A contour map of each object is also shown.

3C 17, $z = 0.2197$.—This galaxy is a broad-line radio galaxy. A VLA map shows three knots, one of which is identified as the core (Morganti, Killeen, & Tadhunter 1993). The *HST* image shows a slightly elongated elliptical compact nucleus making a $\sim 75°$ angle with the radio axis.

3C 19, $z = 0.482$.—The *HST* image shows some emission extending in the northwest direction from the nucleus ending in a patch. The radio axis is directed almost perpendicular to the optical emission. There is also a feature that is a candidate for an optical jet.

3C 20, $z = 0.174$.—This galaxy has a known optical hot spot found by Hiltner et al. (1994). We indicated the position of the hot spot with an arrow in the figure. The radio map shows a slightly elongated core in position angle 101°. Our image shows a bar of emission in the same direction, and so we consider this to be a candidate for an optical jet.

3C 28, $z = 0.1952$.—This elliptical galaxy is part of an X-ray cluster, Abell 115 (Feretti et al. 1984). The galaxy hosts a narrow-angle–tail radio source (Gregorini & Bondi 1989).

3C 33.1, $z = 0.181$.—The *HST* image suggests that the galaxy is a member of a small group. There are faint, compact patches of emission around the galaxy nucleus, a suggestion of dust lane features to the northwest and a narrow extension to the east.

3C 42, $z = 0.395$.—This is a candidate for an optical hot spot; a patch of emission southeast of the galaxy coincides with the radio emission (Leahy et al. 1991).

3C 46, $z = 0.4373$.—The galaxy appears to be partly obscured by dust. The radio emission is extended perpendicular to the possible dust lane (Gregorinni et al. 1988).

3C 52, $z = 0.2854$.—This image shows a galaxy with a dust disk. The radio image is X-shaped (Leahy & Williams 1984).

3C 61.1, $z = 0.186$.—The optical image is highly complex with structures including tails of emission emerging from the nucleus to the south and east. There is no obvious correlation between optical and radio emission features (Leahy & Perley 1991). The galaxy is one of four galaxies in a group.

3C 63, $z = 0.175$.—This galaxy is known to have strong emission lines (Spinrad et al. 1985).

3C 67, $z = 0.3102$.—The galaxy appears to have two arclike arms of emission bending to the north and to the south. In one arm there are separate distinguishable patches. The optical emission is extended in the same direction as the radio axis.

3C 79, $z = 0.2559$.—This is a very complex object, consisting of four patches of different sizes. The radio axis is aligned with the optical axis to within 15°. 3C 79 is a broad-line radio galaxy (Lilly & Longair 1984). The object has been classified as an N-type galaxy (Kristian, Sandage, & Katem 1974). The image shows no compact nucleus.

3C 89, $z = 0.1386$.—The *HST* image shows a diffuse, elliptical source with indications of substructure. This

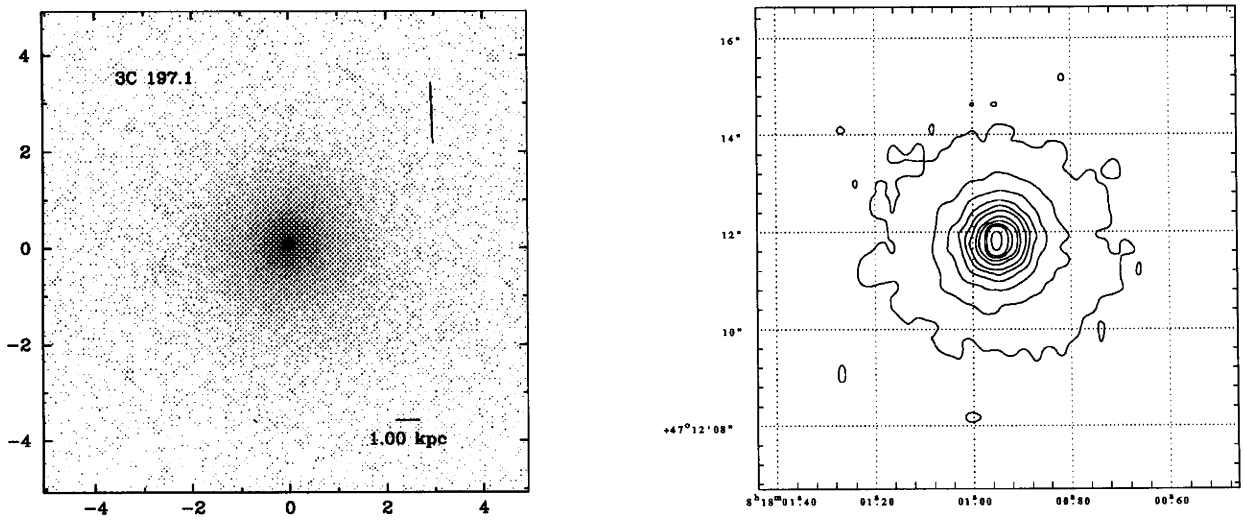

FIG. 33.—(*Left*) 3C 197.1, $z = 0.1301$. (*Right*) Contour levels: 1, 2, 3, 4, 5, 6, 8, 10, 15, 20, 40, 60 × 1.866 × 10^{-18} ergs s^{-1} cm^{-2} $Å^{-1}$ $pixel^{-1}$.

galaxy hosts a narrow-angle–tail radio source (Baum et al. 1988).

3C 93.1, $z = 0.244$.—The image shows an elliptical nucleus with a faint extension to the west coinciding with the radio emission (Akujor et al. 1991). This object has strong emission lines.

3C 103, $z = 0.3306$.—There is a cosmic ray very near to the galaxy nucleus. The elongated galaxy nucleus shows no obvious connection with radio emission (Pooley et al. 1987).

3C 109, $z = 0.3056$.—The image of this N galaxy shows some filamentary emission around the compact nucleus in northeast direction. This radio galaxy is an isolated, broad-line radio galaxy (Grandi & Osterbrock 1978). We have not yet attempted point-spread function (PSF) subtraction.

3C 123, $z = 0.218$.—The image shows a diffuse source.

3C 132, $z = 0.214$.—The image shows an elliptical nucleus with some structure.

3C 133, $z = 0.2779$.—The image shows an elliptical nucleus with some faint emission extending to the east in the direction of the radio source. This faint emission is a candidate for an optical jet.

3C 135, $z = 0.1273$.—This N galaxy is a member of a close pair, companion to the southwest. There is elongated fine structure with the same orientation. The system lies in a rich cluster of galaxies (McCarthy, Spinrad, & van Breugel 1995).

3C 153, $z = 0.2769$.—The image shows an elliptical nucleus (less than 1 kpc). This galaxy has strong emission lines.

3C 165, $z = 0.2957$.—The image shows a nucleus that is elongated and shows some structure. The WFPC2 image shows that the radio galaxy is part of a cluster of galaxies.

3C 166, $z = 0.245$.—The elliptical nucleus shows some extended emission to the north and south. The radio source (Leahy & Williams 1984) lies along the extended emission.

3C 171, $z = 0.2384$.—There is extensive emission-line gas Heckman, van Breugel, & Miley 1984) around this broad-line radio galaxy (Lilly & Longair 1984). The nucleus is resolved sufficiently enough to see that it comprises several parts. The radio image shows an elongated, small bright

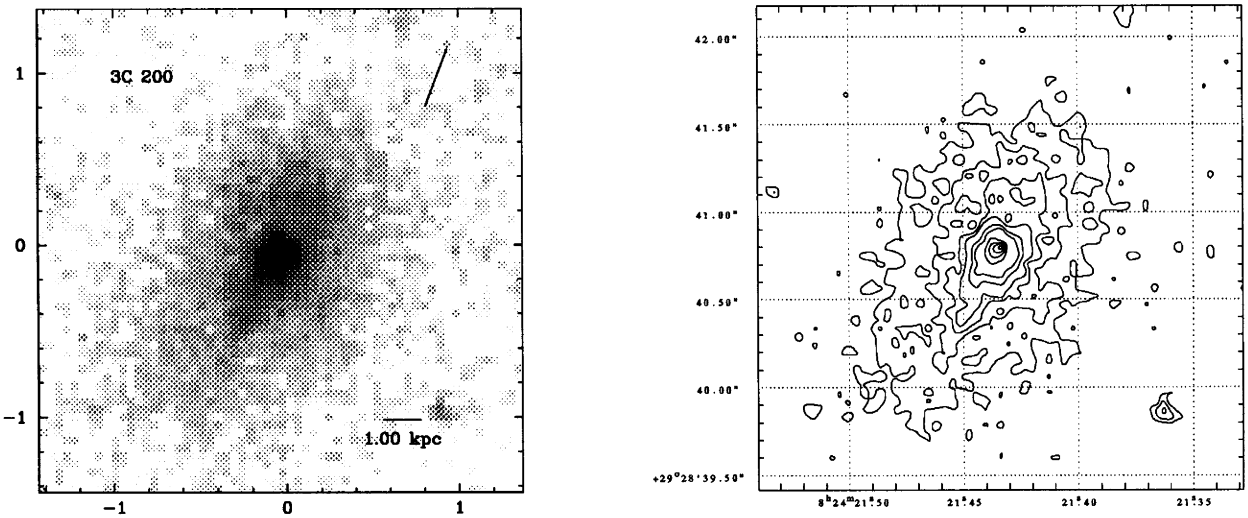

FIG. 34.—(*Left*) 3C 200, $z = 0.458$. (*Right*) Contour levels: 4, 6, 8, 10, 15, 20, 40, 60, 80, 100 × 1.866 × 10^{-18} ergs s^{-1} cm^{-2} $Å^{-1}$ $pixel^{-1}$.

TABLE 2

PROPERTIES: RADIO GALAXIES WITH $0.1 < z < 0.5$

3CR (1)	z (2)	$S(178)$ (Jy) (3)	$\log_{10} P$ (4)	α (5)	LAS (arcsec) (6)	P.A. (7)	FR (8)	EM (9)	References (10)
17.0	0.2197	20	27.31	0.52	30	147	II	SE	3
19.0	0.482	12.1	27.81	0.6	6	29	II	...	14, 3
20.0	0.174[b]	42.9	27.43	0.67	51	101[a]	II	...	8, 3
28.0	0.1952	16.3	27.11	1.06	30	166	II	E	2, 3
33.1	0.181	13	26.95	0.62	216	45	II	...	2, 3
42.0	0.395	12	27.62	0.73	28	132	II	SE	9, 3
46.0	0.4373	10.2	27.65	1.13	163	68	II	SE	2, 3
52.0	0.2854	13.5	27.37	0.62	51	20	II	...	2, 3
61.1	0.186	31.2	27.35	0.77	186	2[a]	II	...	9, 3
63.0	0.175	19.2	27.08	0.79	22	34	II	SE	2, 3
67.0	0.3102	10	27.32	0.58	2	174	II	...	2, 3
79.0	0.2559	30.5	27.63	0.92	86	105	II	SE	2, 3
89.0	0.1386	20.2	26.90	0.96	60	121	II	ABS	2, 5
93.1	0.244	9.9	27.10	0.7	0.3	-	II	SE	3
103.0.....	0.33	26.6	27.80	0.79	...	159	...	SE	2
109.0.....	0.3056	21.6	27.64	0.85	96	143	II	SE	2, 3
123.0.....	0.218	189	28.28	0.7	23	115	II	E	2, 3
132.0.....	0.214	13.7	27.12	0.68	23	130[a]	II	E	14, 3
133.0.....	0.2775	22.3	27.57	0.7	12	107	II	SE	14, 3
135.0.....	0.1273	17.3	26.75	0.92	130	...	II	SE	6
153.0.....	0.2769	15.3	27.40	0.66	7	50	II	SE	2, 3
165.0.....	0.2957[c]	13.5	27.41	0.71	...	159	...	WE	2
166.0.....	0.245	14.7	27.27	0.9	...	180	...	...	2
171.0.....	0.2384	19.5	27.37	0.87	30	100	II	SE	2, 3
173.1.....	0.292	15.4	27.45	0.88	58	17	II	ABS	9, 3
180.0.....	0.22	15.1	27.19	0.84	...	...	...	SE	2
184.1.....	0.1182	13	26.56	0.68	167	157[a]	II	SE	2, 3
196.1.....	0.198	18.6	27.18	1.16	4	43	II	SE	2, 3
197.1.....	0.1301	8.1	26.44	0.69	14	2	II	ABS	6, 3
200.0.....	0.458	11.3	27.73	0.84	17	159	II	WE	2, 3
213.1.....	0.194	6.6	26.71	0.55	43	162	II	SE	10, 3
219.0.....	0.1744	41.2	27.41	0.81	184	40	II	SE	2, 3
223.0.....	0.1368	14.7	26.75	0.74	300	164	II	SE	2, 3
223.1.....	0.1075	6	26.14	0.56	117	15[a]	II	SE	2, 3
234.0.....	0.1848	31.4	27.35	0.86	110	64[a]	II	SE	2, 3
244.1.....	0.428	20.3	27.92	0.82	52	168[a]	II	SE	2, 3
258.0.....	0.165	9.7	26.73	1.3	3	31	II	E	11, 3
268.2.....	0.362	9.7	27.45	1.0	96	21[a]	...	SE	2
268.3.....	0.371	10.7	27.51	0.5	1	161	II	SE	2, 3
274.1.....	0.422	16.5	27.82	0.87	152	76[a]	II	...	2
275.0.....	0.480	14.5	27.89	0.68	5	51	II	...	2, 3
277.0.....	0.414	7.5	27.46	0.89	140	75[a]	II	...	2, 3
284.0.....	0.2394	11.3	27.14	0.95	176	101[a]	II	SE	2, 3
287.1.....	0.2159	8.2	26.90	0.52	112	91[a]	II	SE	2, 3
288.0.....	0.246	18.9	27.39	0.85	16	146	II	WE	2, 3
299.0.....	0.367	11.8	27.55	0.65	12	11	II	SE	2, 10
300.0.....	0.27	17.9	27.45	0.75	96	130	II	...	2, 3
303.0.....	0.141	11.2	26.66	0.76	38	97	II	...	2, 3
303.1.....	0.267	8.1	27.09	0.77	2	132	II	SE	2, 3
306.1.....	0.441	13.5	27.78	0.9	93	180	II	SE	2, 3
313.0.....	0.461	20.6	28.00	0.82	131	59[a]	II	SE	2, 3
314.1.....	0.1197	10.6	26.49	0.95	...	144[a]	...	WE	9
315.0.....	0.1083	17.8	26.62	0.72	...	11[a]	I	SE	12
319.0.....	0.192	15.3	27.07	0.9	93	49[a]	II	WE	12, 3
320.0.....	0.342	9.1	27.37	0.75	18	77	II	ABS	2, 3
327.0.....	0.1039	35.3	26.88	0.61	169	100	II	SE	2, 3
327.1.....	0.4628	23.6	28.06	0.81	17	115	II	SE	2, 3
332.0.....	0.1515	9.6	26.65	0.61	81	20[a]	II	SE	13, 3
341.0.....	0.448	10.8	27.69	0.85	71	50	II	SE	2
346.0.....	0.161	10.9	26.76	0.52	13	71	II	WE	2, 3
348.0.....	0.154	351	28.23	1.	191	101	II	E	15
349.0.....	0.205	13.3	27.07	0.74	82	142	II	SE	2, 3
357.0.....	0.1664	9.7	26.74	0.57	81	111[a]	II	WE	2, 3
379.1.....	0.256	7.4	27.01	0.68	76	161[a]	II	SE	2, 3
381.0.....	0.1605	16.6	26.94	0.81	69	4[a]	II	SE	2, 3
401.0.....	0.201	20.9	27.25	0.71	19	24	II	...	2, 3
410.0.....	0.2485	34.6	27.66	0.56	13	129	II	...	2, 3
411.0.....	0.467	16.5	27.92	0.79	22	108	II	SE	2, 3
424.0.....	0.127	14.6	26.68	0.85	33	156	I	WE	6
433.0.....	0.1016	56.2	27.06	0.75	58	172	II	SE	2, 6
434.0.....	0.322	4.8	27.04	0.61	12	78	II	WE	2, 3

TABLE 2—*Continued*

3CR (1)	z (2)	$S(178)$ (Jy) (3)	$\log_{10} P$ (4)	α (5)	LAS (arcsec) (6)	P.A. (7)	FR (8)	EM (9)	References (10)
435.A.....	0.471	11.6	27.77	0.87	14	31	II	...	2, 7
436.0	0.2145	17.8	27.23	0.86	105	...	II	SE	3
438.0	0.29	44.7	27.91	0.88	19	136	II	WE	2, 3
456.0	0.233	10.6	27.08	0.69	...	...	II	SE	...
459.0	0.2199	25.6	27.42	0.74	8	94	II	E	2, 3
460.0	0.268	8.2	27.10	0.8	6	36	II	...	2

NOTE.—Col. (1) = 3CR number; col. (2) = redshift; col. (3) = radio flux at 178 MHz; col. (4) = log radio power at 178 MHz in W Hz^{-1}; col. (5) = radio spectral index; col. (6) = radio source largest angular size; col. (7) = radio structure position angle; col. (8) = Fanaroff-Riley type; col. (9) = emission lines; col. (10) = references. Data taken from the literature. Cols. (2), (3), (4), (6), and (9) are taken from Spinrad et al. 1985; cols. (7) and (8) from references in col. (10).

[a] Large-scale P.A.

[b] Lawrence et al. 1986.

[c] Pooley et al. 1987.

REFERENCES.—(1) Spinrad et al. 1985; (2) McCarthy et al. 1995; (3) McCarthy, van Breugel, & Kapahi 1991; (5) Baum et al. 1988; (6) Black et al. 1992; (7) McCarthy et al. 1989; (8) Hiltner et al. 1994; (9) Leahy & Perley 1991; (10) Spencer et al. 1989; (11) Akujor et al. 1991; (12) Leahy & Williams 1984; (13) Antonucci 1985; (14) Jenkins, Pooley, & Riley 1977; (15) Dreher & Feigelson 1984.

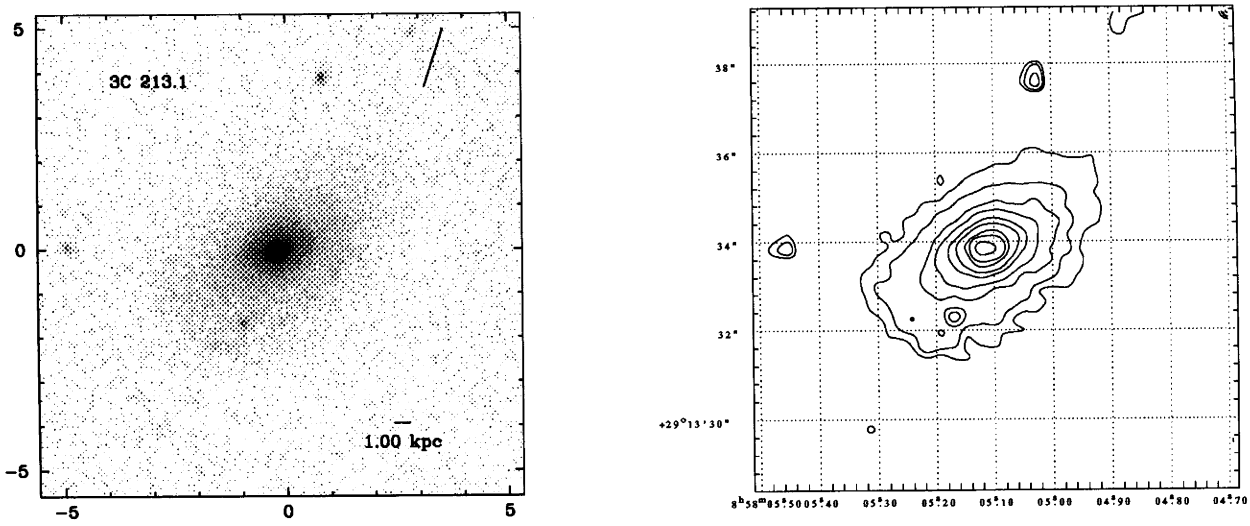

FIG. 35.—(*Left*) 3C 213.1, $z = 0.194$. (*Right*) Contour levels: 3.5, 4, 5, 6, 8, 10, 15, 20, 40, 60 × 1.866 × 10^{-18} ergs s^{-1} cm^{-2} $Å^{-1}$ $pixel^{-1}$.

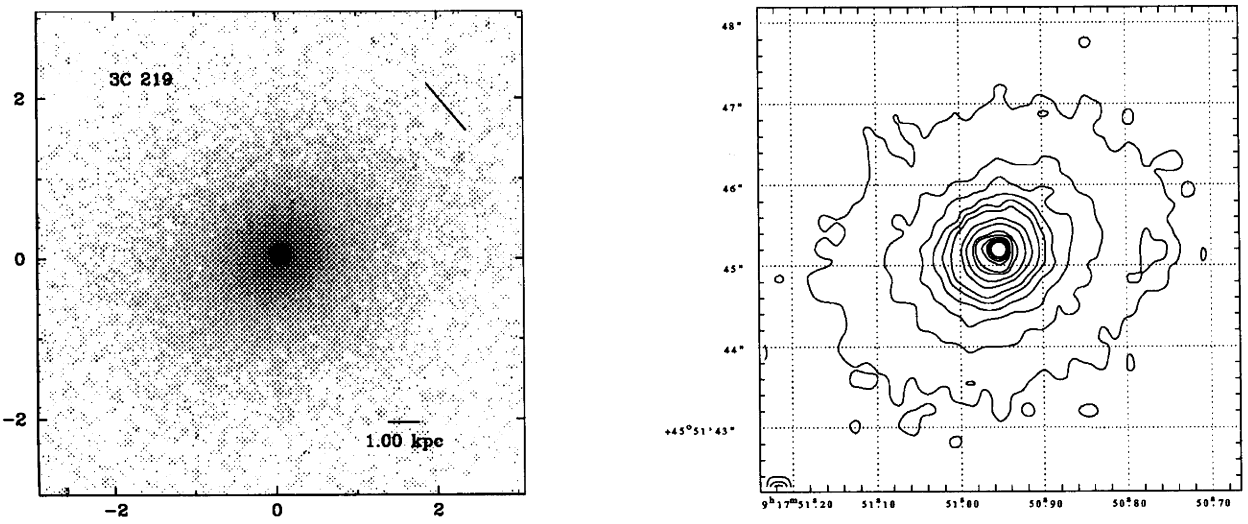

FIG. 36.—(*Left*) 3C 219, $z = 0.1744$. (*Right*) Contour levels: 1, 2, 3, 4, 5, 6, 8, 10, 15, 20, 40, 60, 80, 100, 200 × 1.866 × 10^{-18} ergs s^{-1} cm^{-2} $Å^{-1}$ $pixel^{-1}$.

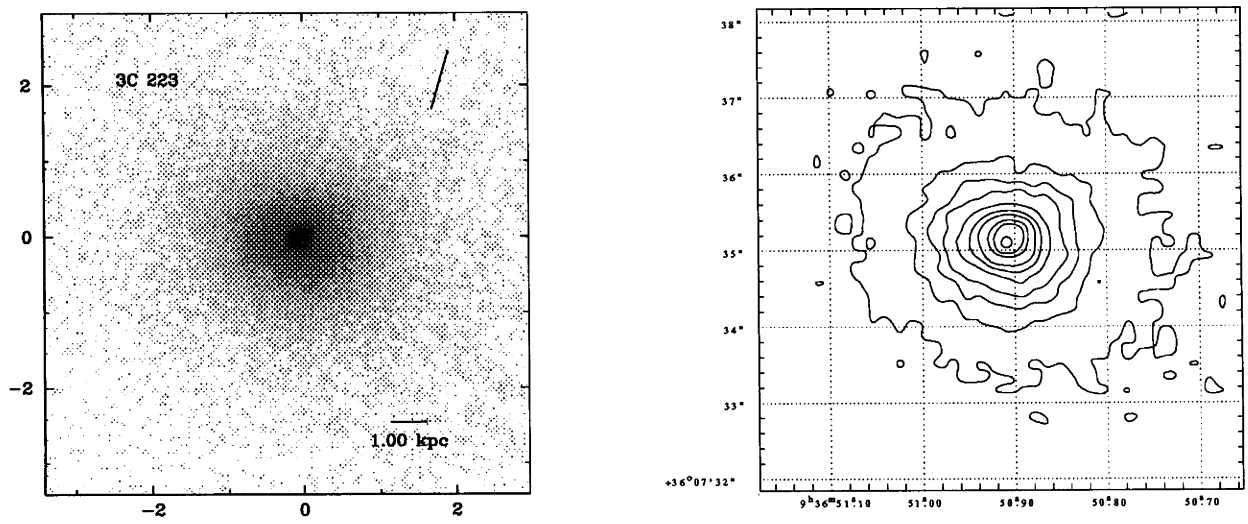

FIG. 37.—(*Left*) 3C 223, $z = 0.1368$. (*Right*) Contour levels: 1, 2, 3, 4, 5, 6, 8, 10, 15, 20, 40 × 1.866 × 10^{-18} ergs s^{-1} cm^{-2} $Å^{-1}$ $pixel^{-1}$.

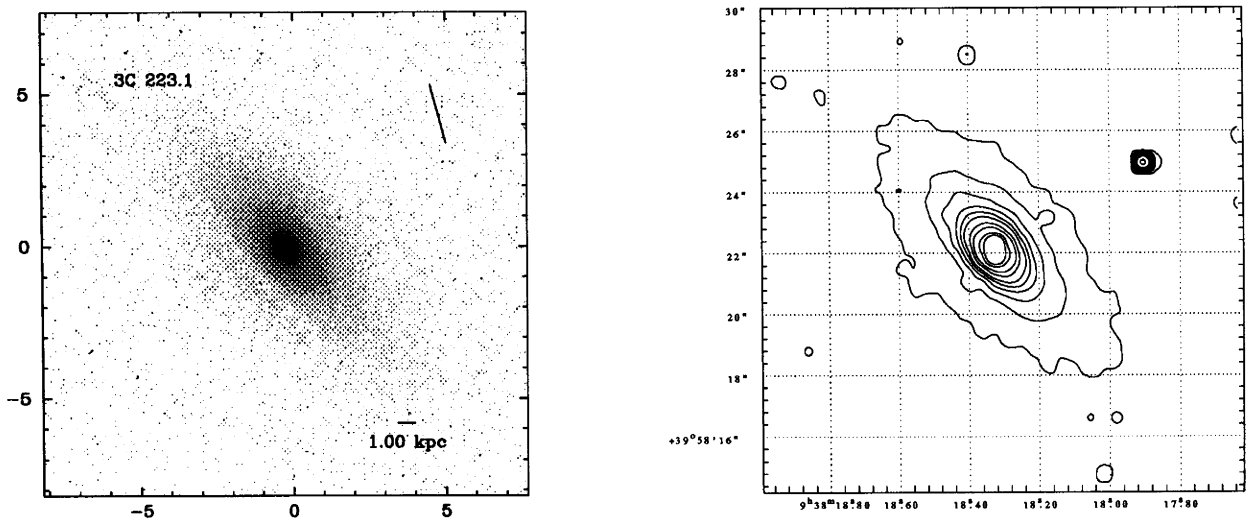

FIG. 38.—(*Left*) 3C 223.1, $z = 0.1075$. (*Right*) Contour levels: 1, 2, 3, 4, 5, 6, 8, 10, 15, 20, 40 × 1.866 × 10^{-18} ergs s^{-1} cm^{-2} $Å^{-1}$ $pixel^{-1}$.

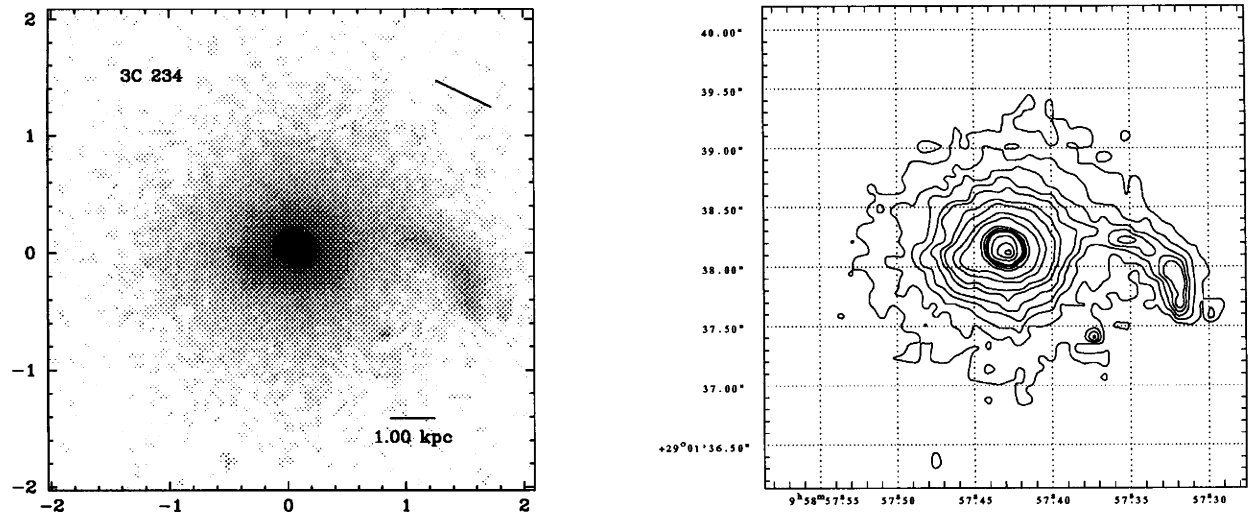

FIG. 39.—(*Left*) 3C 234, $z = 0.1848$. (*Right*) Contour levels: 2, 3, 4, 6, 8, 10, 15, 20, 40, 60 × 1.866 × 10^{-18} ergs s^{-1} cm^{-2} $Å^{-1}$ $pixel^{-1}$.

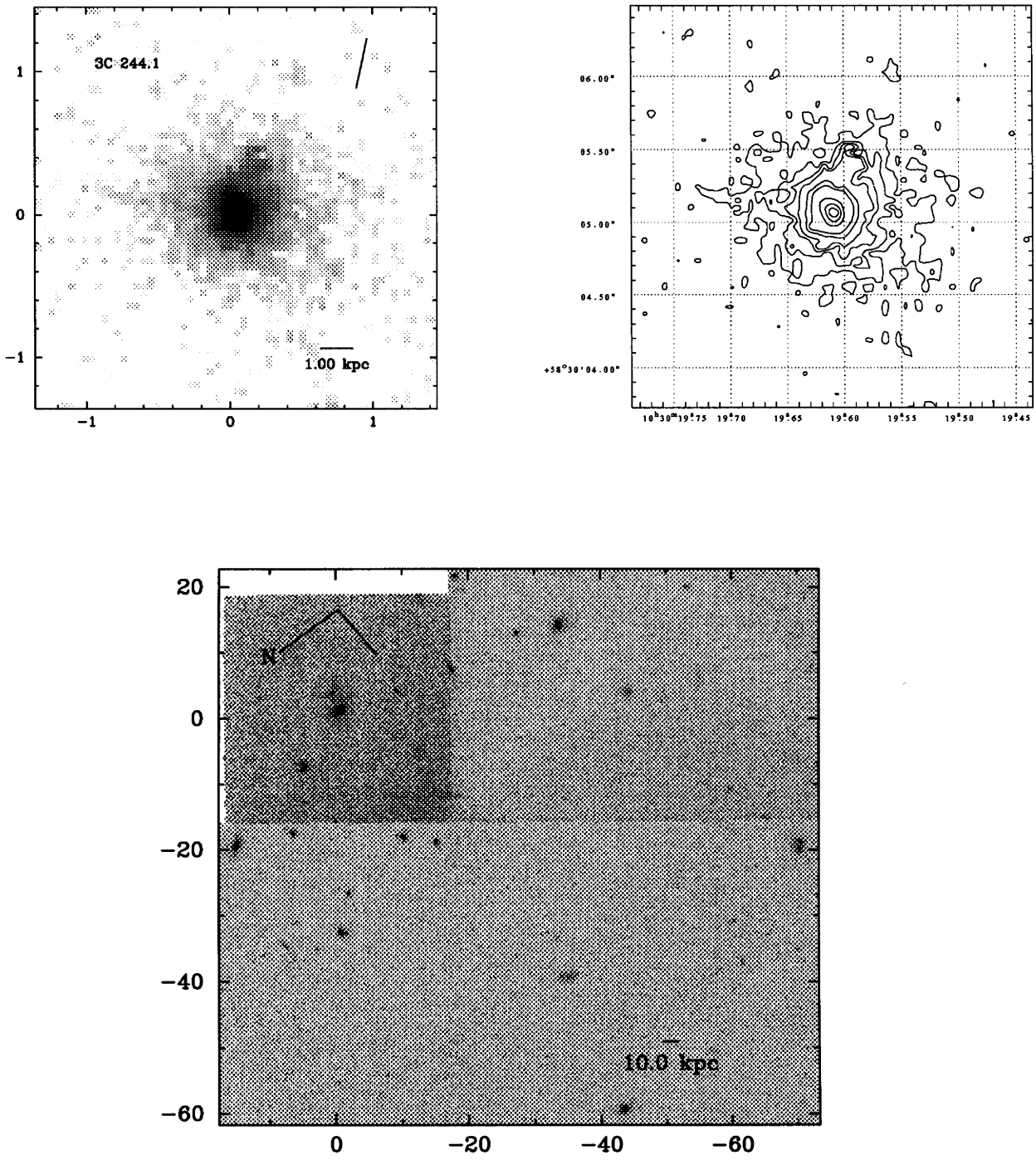

FIG. 40.—(*Left*) 3C 244.1, $z = 0.428$. (*Right*) Contour levels: 4, 6, 8, 10, 20, 40, 60, 80, 100, 200 × 1.866 × 10^{-18} ergs s^{-1} cm^{-2} $Å^{-1}$ $pixel^{-1}$. (*Bottom*) Wide field.

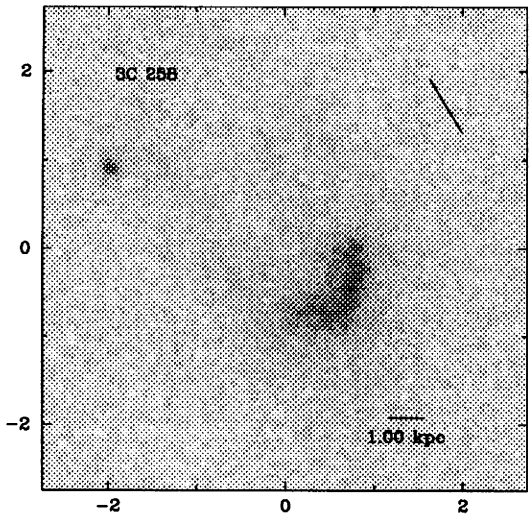

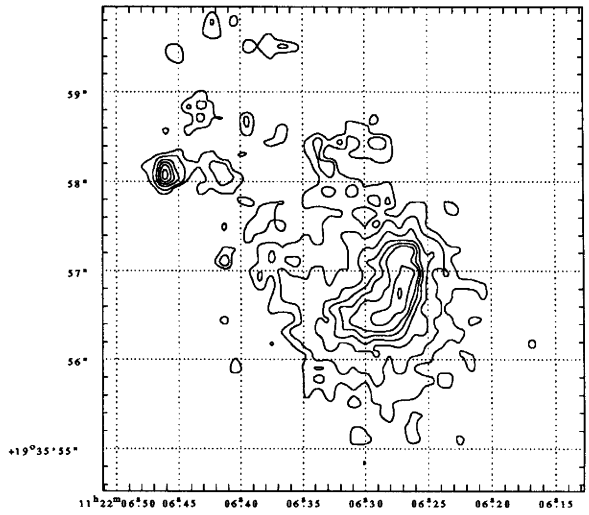

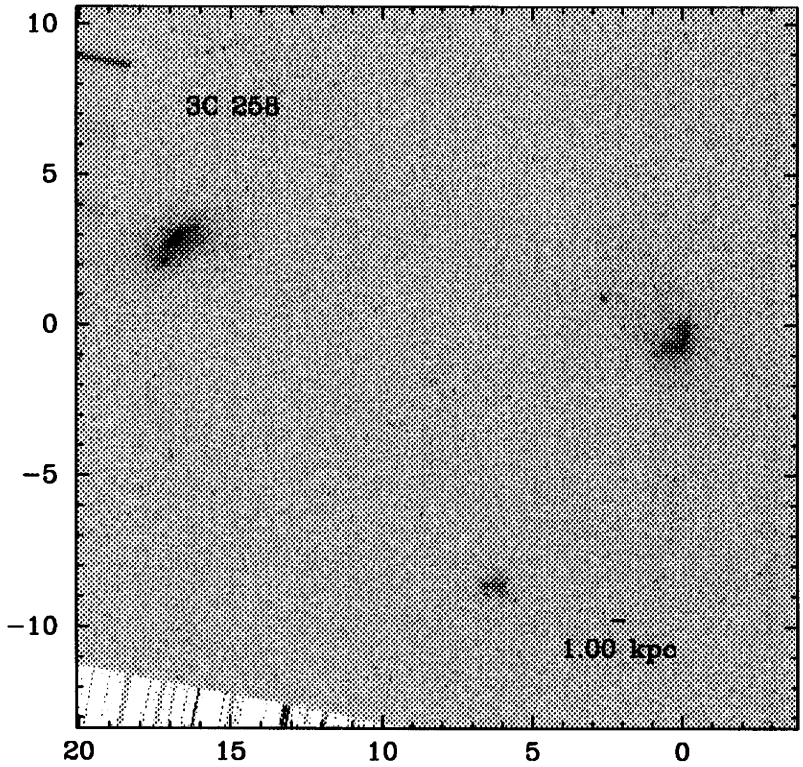

FIG. 41.—(*Left*) 3C 258, $z = 0.165$. (*Right*) Contour levels: 1.5, 2, 3, 4, 5, 6, 8, 10, 20 × 1.866 × 10^{-18} ergs s^{-1} cm^{-2} $Å^{-1}$ $pixel^{-1}$. (*Bottom*) Wide field.

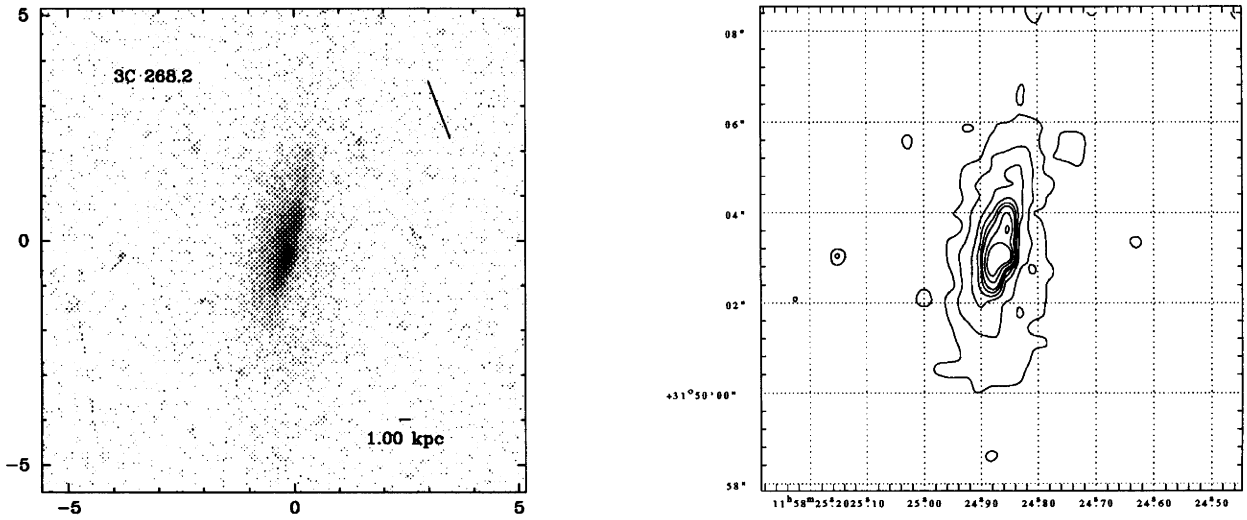

FIG. 42.—(*Left*) 3C 268.2, $z = 0.362$. (*Right*) Contour levels: 1.5, 2, 3, 4, 5, 6, 8, 10, 20 × 1.866 × 10^{-18} ergs s^{-1} cm^{-2} $Å^{-1}$ $pixel^{-1}$.

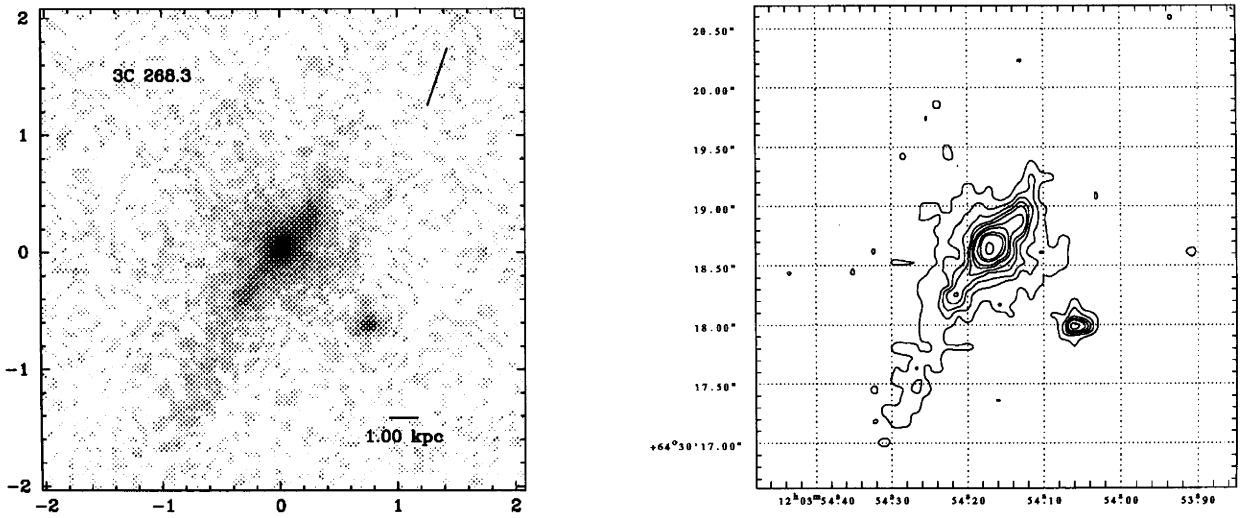

FIG. 43.—(*Left*) 3C 268.3, $z = 0.371$. (*Right*) Contour levels: 2, 3, 4, 5, 6, 8, 10, 20, 40, 60, 80 × 1.866 × 10^{-18} ergs s^{-1} cm^{-2} $Å^{-1}$ $pixel^{-1}$.

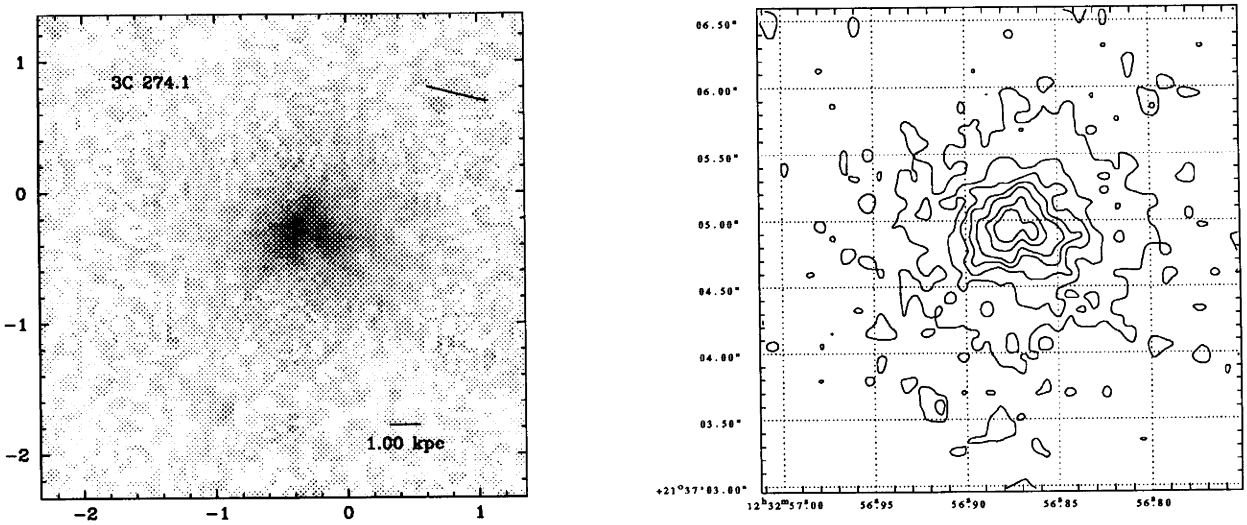

FIG. 44.—(*Left*) 3C 274.1, $z = 0.422$. (*Right*) Contour levels: 2, 3, 4, 5, 6, 8, 10, 20 × 1.866 × 10^{-18} ergs s^{-1} cm^{-2} $Å^{-1}$ $pixel^{-1}$.

TABLE 3

HST, WFPC2, F702W PROPERTIES: RADIO GALAXIES WITH $0.1 < z < 0.5$

3CR (1)	R.A. (2)	Decl. (3)	m (4)	μ (5)	m_1 (6)	μ_1 (7)	m_{15} (8)	μ_{15} (9)	LAS (10)	P.A. (11)	e (12)	Comment (13)
17.0.....	0:35:47.3	−2:24:10	18.8	19.19	22.62	21.47	17.95	22.68	1.9	42	0.22	Compact nucleus
19.0.....	0:38:13.8	32:53:40	21.1	21.04	24.02	21.92	19.17	22.94	1.3	136	0.20	Tail, jet?
20.0.....	0:40:20.1	51:47:11	20.5	19.91	20.79	20.01	19.72	24.81	1.2	130	0.28	Jet?
28.0.....	0:53:09.1	26:08:23	20.3	20.07	20.94	19.97	18.50	23.41	1.9	155	0.39	Diffuse source
33.1.....	1:06:06.7	72:55:59	20.4	19.33	20.41	19.56	18.43	23.46	0.9	63	0.26	
42.0.....	1:25:42.8	28:47:30	20.8	20.64	21.88	19.98	18.90	22.88	1.6	153	0.47	Hot spot?
46.0.....	1:32:34.2	37:38:46	20.1	20.49	23.87	21.86	19.16	23.03	2.8	177	0.57	Dust disk
52.0.....	1:45:14.7	53:17:33	19.8	20.20	21.22	19.70	…	…	1.8	20	0.36	Dust disk
61.1.....	2:10:37.4	86:05:18	21.2	19.78	21.09	20.19	…	…	0.7	165	0.18	Tails
63.0.....	2:18:21.9	−2:10:32	18.8	19.40	19.33	18.54	17.65	22.73	1.7	79	0.26	
67.0.....	2:21:18.1	27:36:38	19.7	19.42	20.09	18.47	19.01	23.27	1.4	175	0.4	Tails, dust
79.0.....	3:07:11.3	16:54:40	18.6	19.64	21.35	19.98	17.76	22.27	5.2	71	…	4 components
89.0.....	3:31:43.4	−1:21:30	18.7	19.94	20.47	20.06	16.91	22.38	3.4	133	0.15	Diffuse source
93.1.....	3:45:35.6	33:44:08	20.3	19.76	20.72	19.43	19.02	23.60	1.3	132	0.22	
103.0	4:04:34.7	42:52:36	20.2	19.21	20.47	18.77	21.10	25.29	1.3	34	0.51	
109.0	4:10:54.9	11:04:41	17.5	18.23	17.77	16.17	17.45	21.73	3.1	59	0.12	Comp. nucleus, tails
123.0	4:33:55.3	29:34:12	22.8	20.26	22.54	21.41	20.54	25.29	0.6	90	0.32	Diffuse source
132.0	4:53:42.3	22:44:43	20.3	19.77	20.84	19.74	18.97	23.75	1.5	7	0.25	Diffuse source
133.0	4:59:54.3	25:12:14	21.6	19.38	21.58	20.10	…	…	1.0	87	0.45	Jet?
135.0	5:11:33.5	0:53:08	18.5	19.45	19.03	18.77	16.43	22.04	2.0	141	0.19	Comp. nucleus, tails
153.0	6:05:44.5	48:04:50	20.0	20.03	22.73	21.25	19.07	23.47	1.5	…	…	
165.0	6:40:04.5	23:22:04	20.6	20.45	22.99	21.43	18.37	22.69	1.4	8	0.29	
166.0	6:42:24.7	21:25:03	21.1	19.63	21.19	19.88	20.13	24.70	0.9	108	0.17	Tails?
171.0	6:51:11.0	54:12:52	19.8	19.68	20.39	19.12	18.42	23.03	1.4	66	0.11	Dust, tails, jet?
173.1	7:02:48.1	74:54:17	19.2	20.00	20.55	19.01	18.52	22.86	2.0	8	0.23	Dust disk
180.0	7:24:33.4	−1:58:25	19.6	19.91	20.76	19.61	18.39	23.12	2.0	28	0.41	Dust, tails
184.1	7:34:25.0	80:33:26	18.5	19.19	18.80	18.67	17.12	22.87	1.7	40	0.18	Faint tail
196.1	8:12:56.9	−2:59:10	19.5	20.14	21.69	20.70	17.53	22.42	1.3	…	…	3 clumps, dust?, jet?
197.1	8:18:00.9	47:12:12	18.5	19.34	19.02	18.72	17.76	23.34	1.8	…	…	
200.0	8:24:21.4	29:28:41	20.1	20.45	21.61	19.55	19.82	23.65	2.5	150	0.36	Jet?
213.1	8:58:05.1	29:13:34	18.6	20.02	19.81	18.85	16.43	21.35	2.5	161	0.36	Hot spot?
219.0	9:17:50.9	45:51:45	18.5	19.35	19.02	18.23	17.80	22.89	1.1	145	0.08	Comp. nucleus
223.0	9:36:50.9	36:07:35	18.8	19.57	19.36	18.97	17.40	22.90	1.9	93	0.13	Tail?
223.1	9:38:18.3	39:58:22	17.5	19.27	18.38	18.41	17.06	22.97	3.7	40	0.45	Dust disk
234.0	9:58:57.5	29:01:39	17.9	18.78	22.87	22.00	17.42	22.42	2.7	80	0.47	Tails
244.1	10:30:19.6	58:30:06	20.2	20.34	24.61	22.62	19.05	22.94	2.1	76	0.20	Tail?
258.0	11:22:06.3	19:35:57	21.9	20.32	21.81	21.11	18.32	23.50	1.0	153	0.67	Distorted
268.2	11:58:24.9	31:50:03	20.1	20.37	21.62	19.81	19.05	23.13	2.4	164	0.65	Very elongated, dust?
268.3	12:03:54.2	64:30:19	21.9	19.61	21.84	20.01	19.83	23.88	1.3	144	0.46	Tails, jet?
274.1	12:32:56.9	21:37:05	21.1	20.74	22.99	21.01	19.73	23.63	1.2	…	…	Dust lane?
275.0	12:39:44.8	−4:29:57	20.7	20.62	22.60	20.50	20.99	24.77	1.5	18	0.46	Dust?, tails
277.0	12:49:26.1	50:50:42	21.3	20.85	24.19	22.23	19.66	23.59	0.9	…	…	
284.0	13:08:41.4	27:44:03	19.0	19.90	20.34	19.07	18.02	22.63	2.7	151	0.08	Dust, tails
287.1	13:30:20.8	2:16:06	19.0	19.39	19.49	18.37	17.93	22.69	1.6	142	0.08	Comp. nucleus, hot spot?
288.0	13:36:38.6	39:06:23	19.0	20.39	21.20	19.89	17.34	21.91	2.3	…	…	Diffuse source
299.0	14:19:06.2	41:58:28	20.9	20.73	22.47	20.65	21.00	25.06	2.7	47	…	Tails, dust?
300.0	14:20:40.1	19:49:13	19.8	20.35	21.89	20.45	17.84	22.28	1.9	89	…	
303.0	14:41:24.9	52:14:19	18.1	19.08	18.50	18.06	17.42	22.86	2.0	…	…	Comp. nucleus
303.1	14:43:54.3	77:20:04	19.6	20.01	20.67	19.25	18.05	22.51	1.9	169	0.47	Tails, dust, hot spot?
306.1	14:52:24.2	−4:08:52	20.5	20.47	21.55	19.53	19.41	23.27	0.9	135	0.29	Dust
313.0	15:08:32.6	8:02:57	20.9	20.71	18.86	16.80	18.64	22.45	1.4	…	…	
314.1	15:10:11.5	70:57:11	19.1	19.56	19.44	19.29	17.96	23.69	1.9	75	0.31	
315.0	15:11:30.9	26:18:39	18.3	19.13	19.13	19.15	16.49	22.39	2.6	33	0.46	Highly elongated
319.0	15:22:44.1	54:38:38	20.0	19.49	20.24	19.30	21.90	26.84	1.2	…	…	
320.0	15:29:29.8	35:43:50	20.2	20.65	22.62	20.88	18.88	23.01	1.8	…	…	Diffuse source
327.0	15:59:55.7	2:06:12	17.5	19.54	18.54	18.64	…	…	4.0	135	0.39	Filamentary dust
327.1	16:02:13.1	1:25:58	21.1	20.21	24.20	22.14	19.91	23.72	0.8	38	0.05	
332.0	16:15:46.9	32:29:50	18.2	18.94	18.53	17.97	17.34	22.66	2.0	54	0.10	
341.0	16:26:02.6	27:48:12	20.9	20.31	21.63	19.60	21.46	25.30	1.0	17	0.41	Tails
346.0	16:41:34.5	17:21:21	19.1	19.27	19.46	18.80	17.16	22.38	1.4	122	0.23	Optical jet
348.0	16:48:40.0	5:04:36	21.8	20.27	21.71	21.12	17.38	22.68	0.9	…	…	Two dust rings
349.0	16:58:04.5	47:07:20	19.8	19.63	20.17	19.13	18.64	23.47	1.4	14	0.31	
357.0	17:26:27.3	31:48:26	18.4	19.64	19.39	18.68	17.22	22.38	3.1	84	…	Dust
379.1	18:25:55.7	74:19:07	19.3	20.11	20.62	19.26	18.08	22.60	2.0	…	…	
381.0	18:32:24.6	47:24:39	18.6	19.58	19.39	18.73	17.18	22.41	2.2	156	0.18	Comp. nucleus, tails
401.0	19:39:38.8	60:34:35	20.4	19.64	24.88	23.87	18.24	23.11	1.1	…	0.	
410.0	20:18:04.0	29:32:43	19.9	18.95	24.08	22.76	18.41	22.97	1.0	10	0.36	Jet?
411.0	20:19:44.2	9:51:35	22.6	20.70	25.25	23.18	21.16	24.97	1.2	…	…	Comp. nucleus
424.0	20:45:44.4	6:50:10	20.2	19.58	20.16	19.90	…	…	1.1	51	0.31	
433.0	21:21:30.6	24:51:32	17.5	19.76	19.09	19.23	16.08	22.10	1.0	94	0.27	Dust, jet?, hot spot?
434.0	21:20:54.4	15:35:12	20.9	20.01	24.16	22.49	18.90	23.11	1	123	0.23	
435.A.....	21:26:37.2	7:19:50	21.4	20.65	22.40	20.32	…	…	1.2	21	0.18	
436.0	21:41:58.0	27:56:29	19.4	20.13	22.74	21.63	17.68	22.45	1.8	3	0.31	Dust
438.0	21:53:45.7	37:46:11	20.9	20.40	23.80	22.27	19.20	23.54	1.2	…	0	Diffuse source, dust?
456.0	23:09:56.7	9:03:07	19.2	19.35	19.60	18.37	17.96	22.60	1.4	107	0.15	
459.0	23:14:02.3	3:48:54	18.3	19.29	22.39	21.24	18.24	22.97	2.4	160	0.13	Tails, hot spot?
460.0	23:18:59.8	23:30:20	20.0	20.17	21.52	20.09	18.58	23.04	2.3	12	0.76	2 components

NOTES.—Col. (1) = 3CR number; cols. (2), (3) = position for epoch B1950; cols. (4), (5) = magnitude and average surface brightness inside a fixed isophotal level; cols. (6), (7) = same as cols. (4) and (5) but inside 1 kpc aperture; cols. (8), (9) = same as for cols. (4) and (5) but inside 15 kpc aperture; col. (10) = largest angular size of optical structure in arcsec; col. (11) = position angle of largest extensions; col. (12) = measured ellipticity (see text).

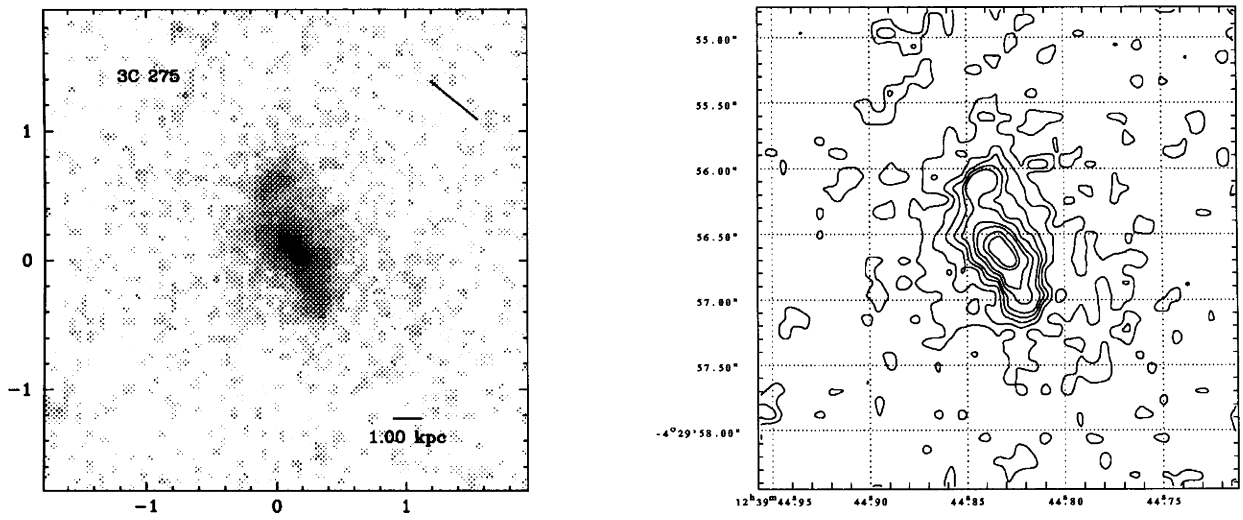

FIG. 45.—(*Left*) 3C 275, $z = 0.480$. (*Right*) Contour levels: 2, 3, 4, 5, 6, 8, 10, 20, 40, 60 × 1.866 × 10^{-18} ergs s^{-1} cm^{-2} $Å^{-1}$ $pixel^{-1}$.

radio bar aligned with the extended optical nucleus (Baum et al. 1988). In this case the morphologically associated optical and radio emission is probably due to the presence of emission-line gas rather than to a continuum optical jet.

3C 173.1, $z = 0.292$.—This galaxy has a nucleus that is partly obscured by dust. The radio axis is pointed perpendicular to the dust. The image shows a cluster of galaxies.

3C 180, $z = 0.22$.—Tails of extended emission are seen around this giant elliptical galaxy. The core appears to be full of dust, or conceivably could be built of three separate components. The image suggests that there is a shell of emission around the nucleus.

3C 184.1, $z = 0.1182$.—This radio galaxy is known to have strong emission lines. The image shows patches of emission to both northeast and southwest of the nucleus. The radio lobes are orientated almost perpendicular to the extended emission (Leahy & Perley 1991).

3C 196.1, $z = 0.198$.—The highly elongated nucleus seems to be broken up in several patches of emission. The radio emission is extended along the same direction as the nucleus (Baum et al. 1988).

3C 197.1, $z = 0.1301$.—The image shows a primarily amorphous elliptical morphology.

3C 200, $z = 0.458$.—The galaxy emission is extended in the same direction as the radio axis (Bogers et al. 1994). There is a narrow feature pointing southeast that is a very strong candidate for an optical jet since the radio morphology is practically identical.

3C 213.1, $z = 0.194$.—The galaxy nucleus is slightly elongated in the same direction as the radio source. The two patches of emission north and south of the nucleus coincide with the radio emission (Spencer et al. 1989) suggesting a double hot spot. The image suggests that there is a "shell" of emission around the galaxy.

3C 219, $z = 0.1744$.—This object is a high-luminosity radio galaxy, and it is a member of a cluster of galaxies (Mathews, Morgan, & Schmidt 1964; Schmidt 1965). There is a possibly interacting companion to the southeast.

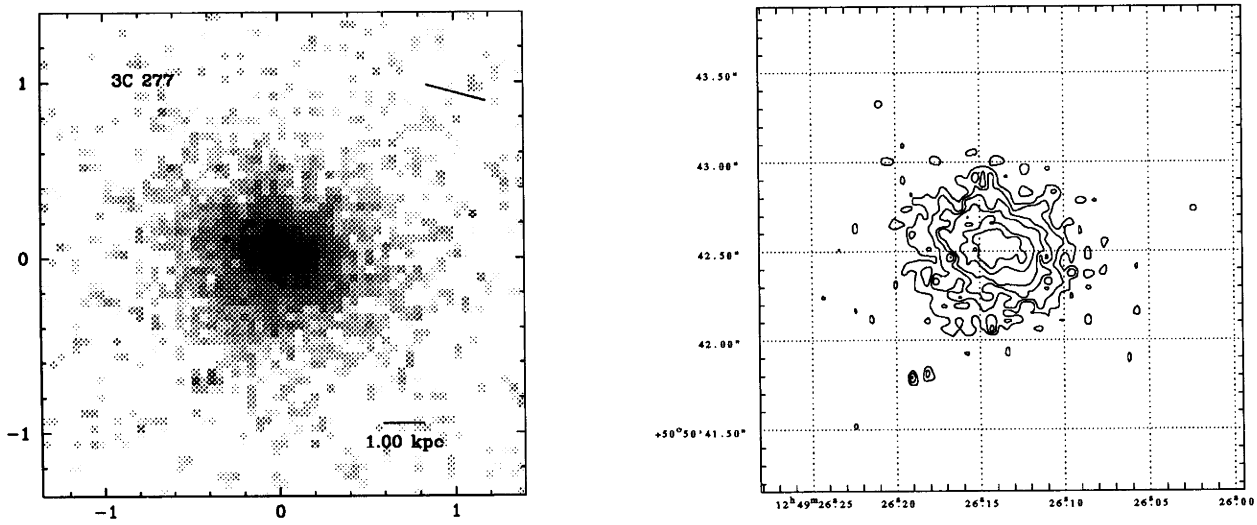

FIG. 46.—(*Left*) 3C 277, $z = 0.414$. (*Right*) Contour levels: 3, 4, 5, 6, 8, 10, 20 × 1.866 × 10^{-18} ergs s^{-1} cm^{-2} $Å^{-1}$ $pixel^{-1}$.

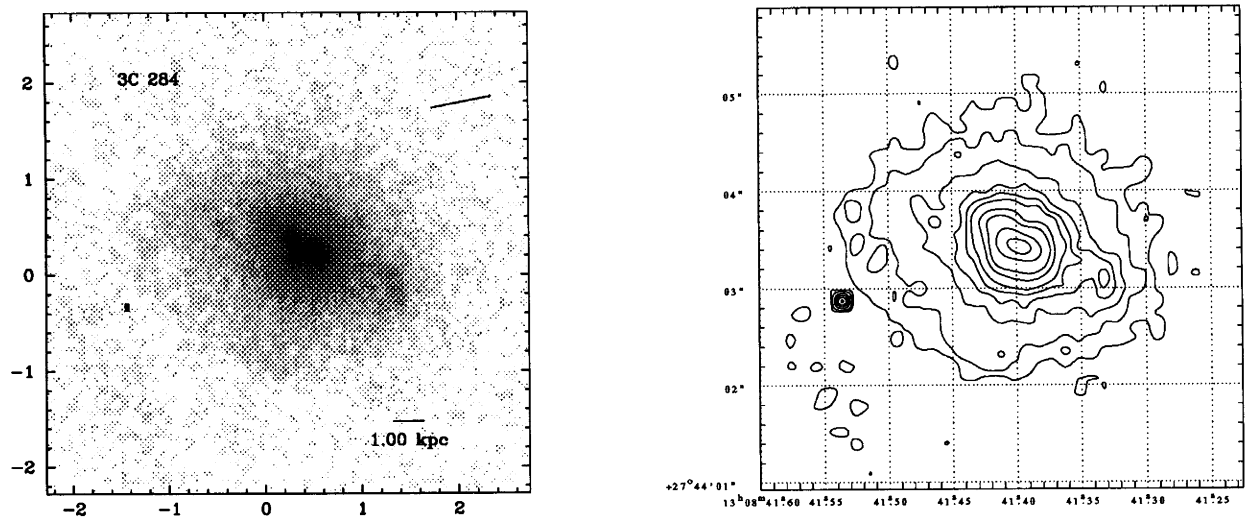

FIG. 47.—(*Left*) 3C 284, $z = 0.2394$. (*Right*) Contour levels: 1.5, 2, 3, 4, 5, 6, 8, 10, 20, 40 × 1.866 × 10^{-18} ergs s^{-1} cm^{-2} $Å^{-1}$ $pixel^{-1}$.

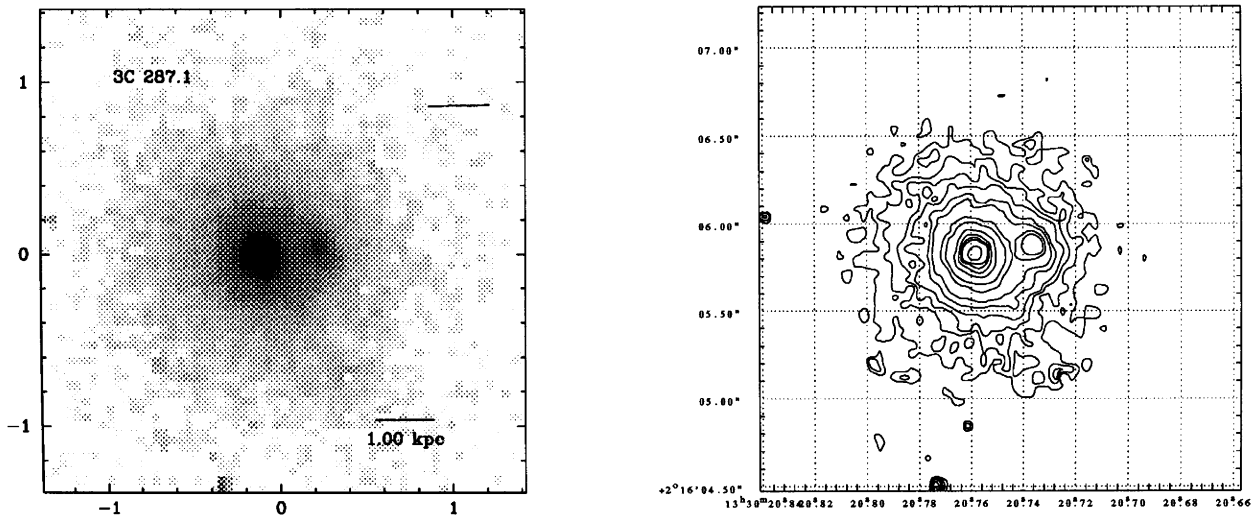

FIG. 48.—(*Left*) 3C 287.1, $z = 0.2159$. (*Right*) Contour levels: 3, 4, 5, 6, 8, 10, 15, 20, 40, 60, 80, 100, 200, 400 × 1.866 × 10^{-18} ergs s^{-1} cm^{-2} $Å^{-1}$ $pixel^{-1}$.

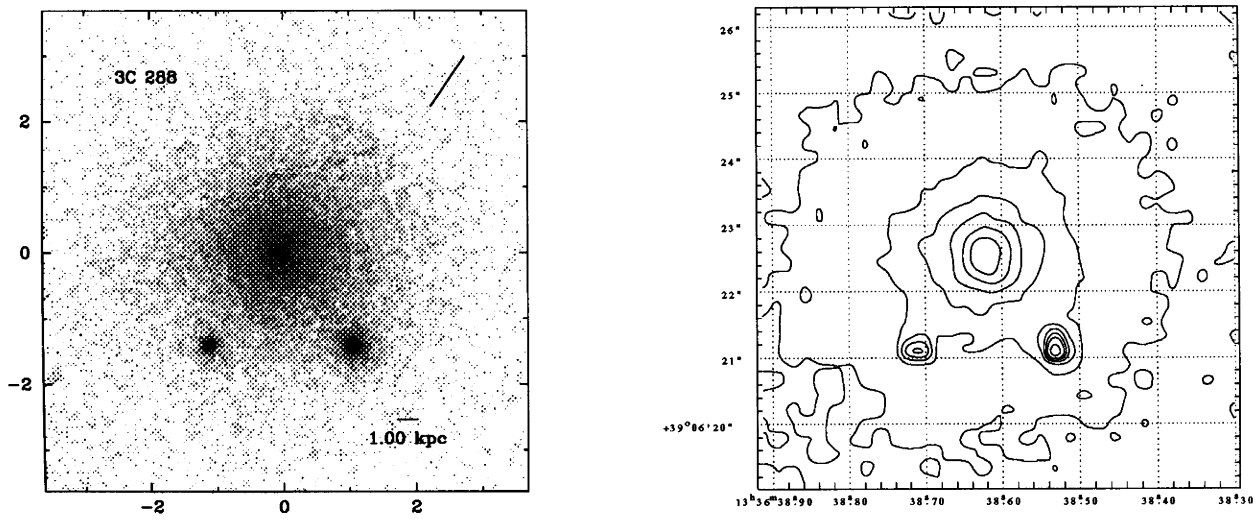

FIG. 49.—(*Left*) 3C 288, $z = 0.246$. (*Right*) Contour levels: 1.5, 2, 3, 4, 5, 6, 8, 10, 20 × 1.866 × 10^{-18} ergs s^{-1} cm^{-2} $Å^{-1}$ $pixel^{-1}$.

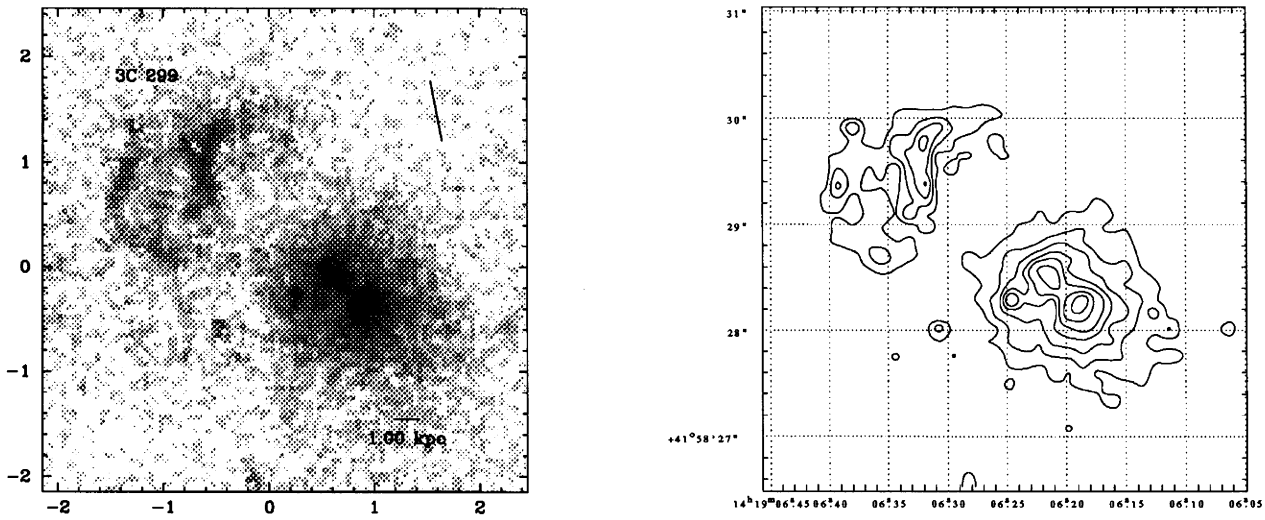

FIG. 50.—(*Left*) 3C 299, $z = 0.367$. (*Right*) Contour levels: 2, 3, 4, 5, 6, 8, 10, 15, 20 × 1.866 × 10^{-18} ergs s^{-1} cm^{-2} $Å^{-1}$ $pixel^{-1}$.

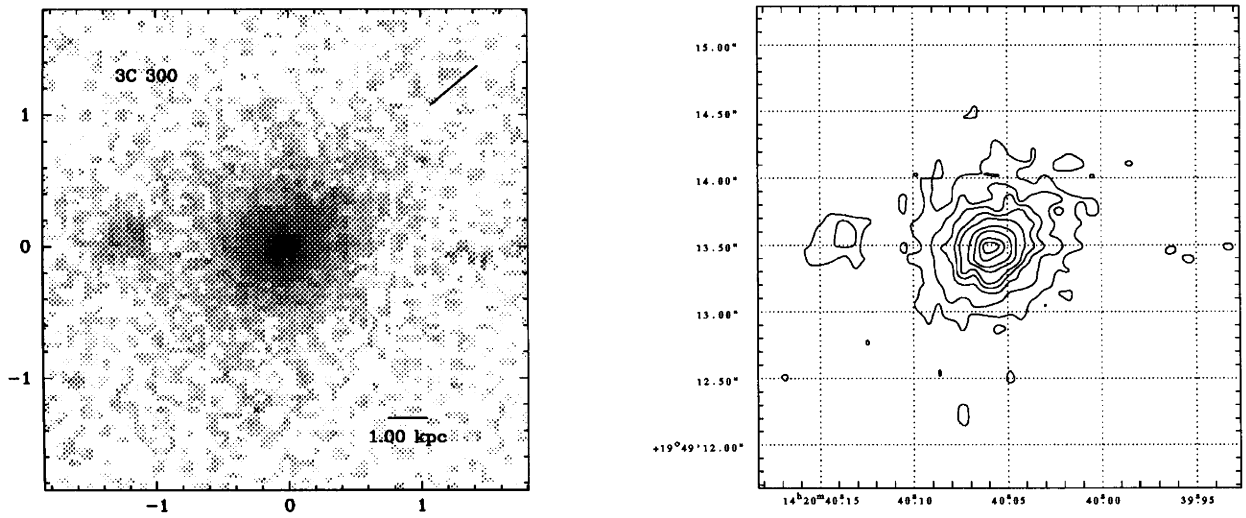

FIG. 51.—(*Left*) 3C 300, $z = 0.27$. (*Right*) Contour levels: 2, 3, 4, 5, 6, 8, 10, 15, 20, 40 × 1.866 × 10^{-18} ergs s^{-1} cm^{-2} $Å^{-1}$ $pixel^{-1}$.

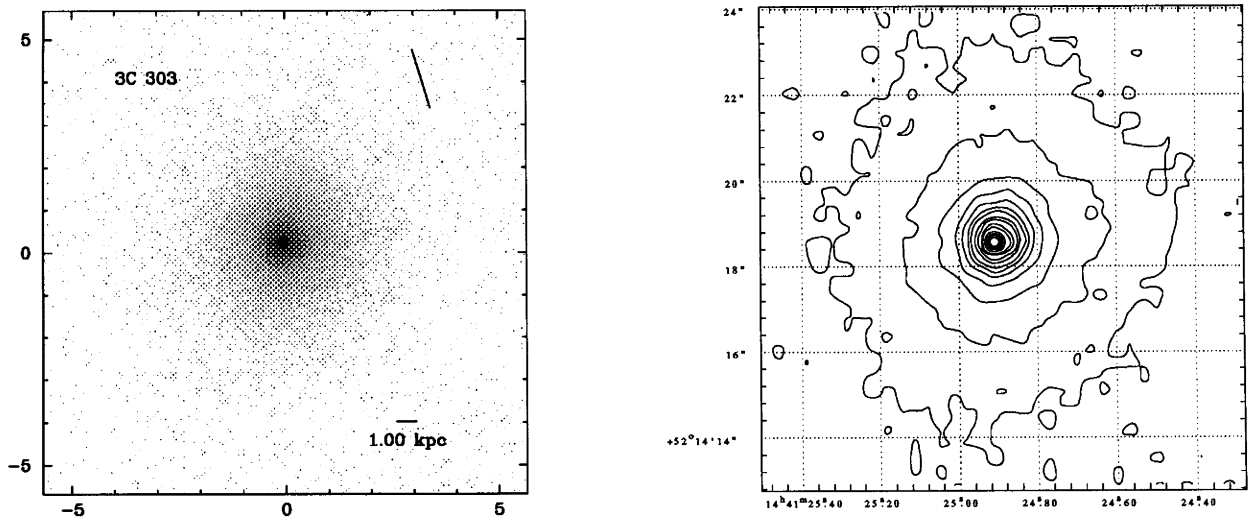

FIG. 52.—(*Left*) 3C 303, $z = 0.141$. (*Right*) Contour levels: 0.5, 1, 2, 3, 4, 5, 6, 8, 10, 20, 40, 60, 80, 100, 200, 400 × 1.866 × 10^{-18} ergs s^{-1} cm^{-2} $Å^{-1}$ $pixel^{-1}$.

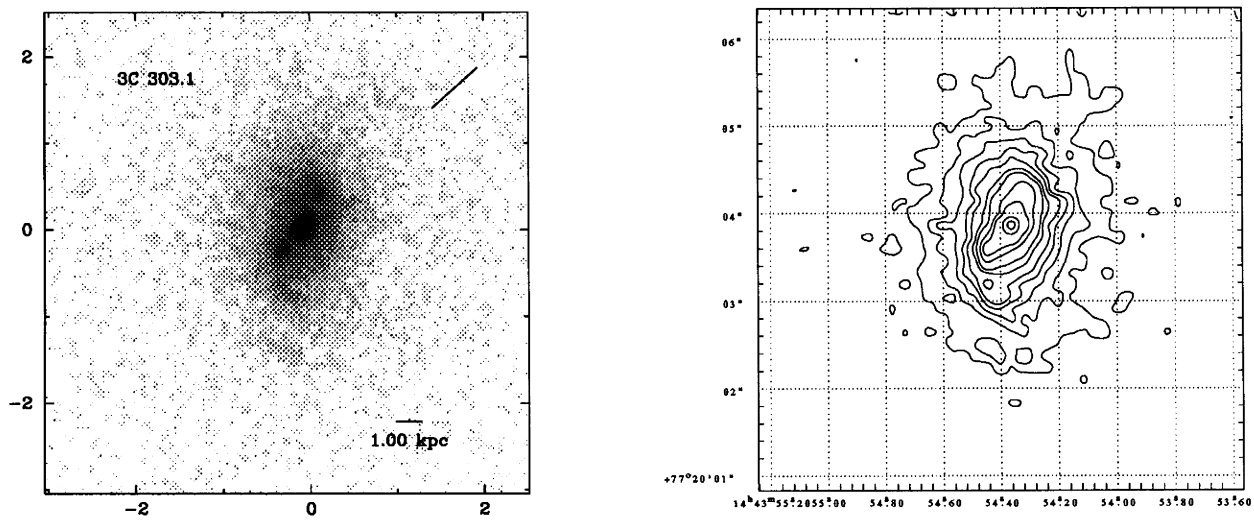

FIG. 53.—(*Left*) 3C 303.1, $z = 0.267$. (*Right*) Contour levels: 2, 3, 4, 5, 6, 8, 10, 15, 20, 40, 60 × 1.866 × 10^{-18} ergs s^{-1} cm^{-2} $Å^{-1}$ $pixel^{-1}$.

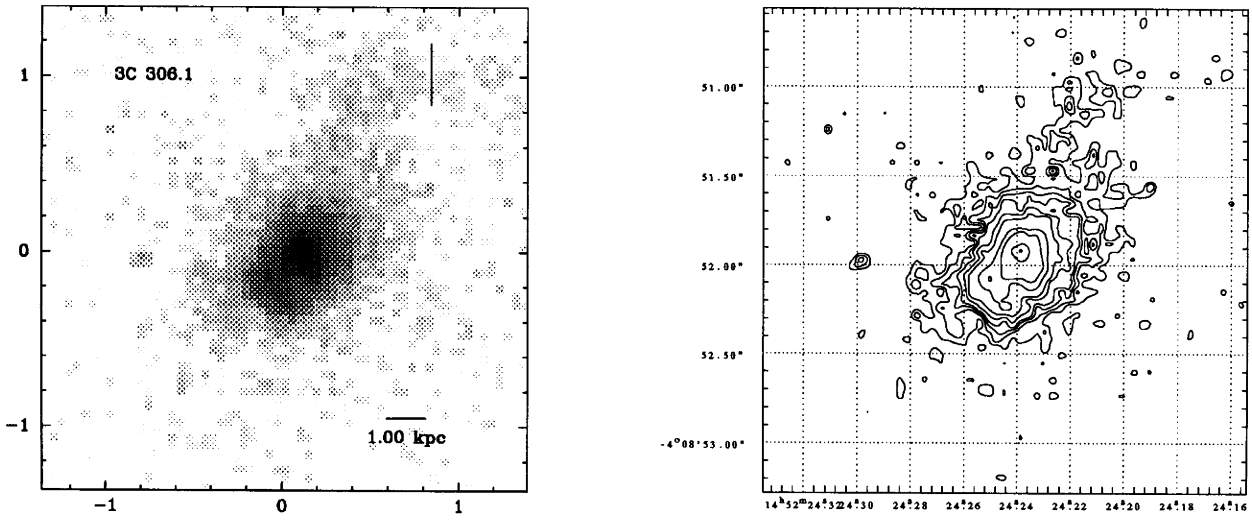

FIG. 54.—(*Left*) 3C 306.1, $z = 0.441$. (*Right*) Contour levels: 3, 4, 5, 6, 8, 10, 15, 20, 40, 60, 80 × 1.866 × 10^{-18} ergs s^{-1} cm^{-2} $Å^{-1}$ $pixel^{-1}$.

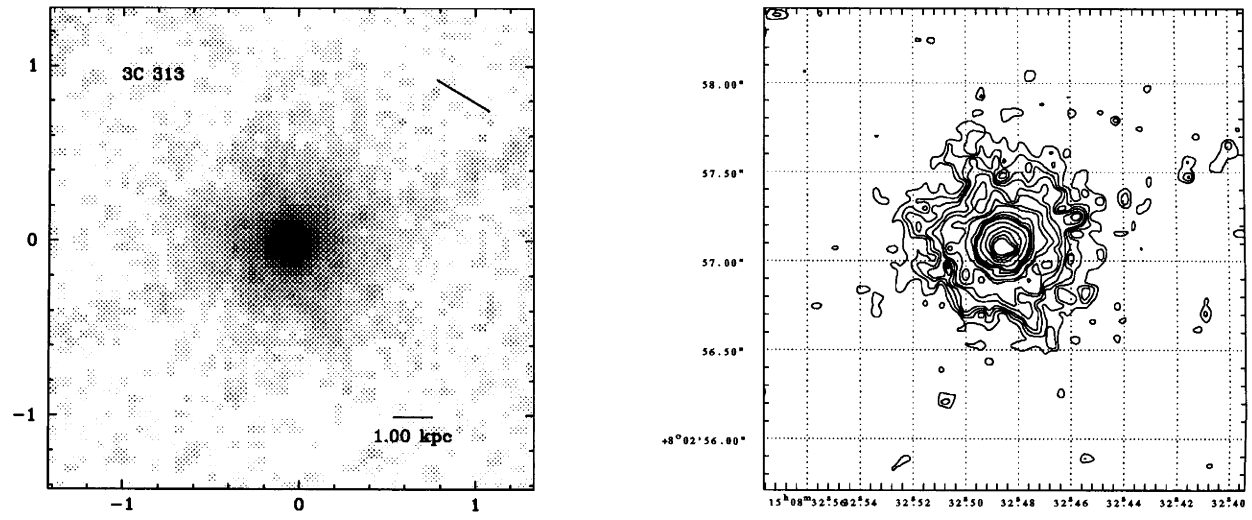

FIG. 55.—(*Left*) 3C 313, $z = 0.461$. (*Right*) Contour levels: 3, 4, 5, 6, 8, 10, 15, 20, 40, 60, 80, 100, 200, 400, 600, 800, 1000 × 1.866 × 10^{-18} ergs s^{-1} cm^{-2} $Å^{-1}$ $pixel^{-1}$.

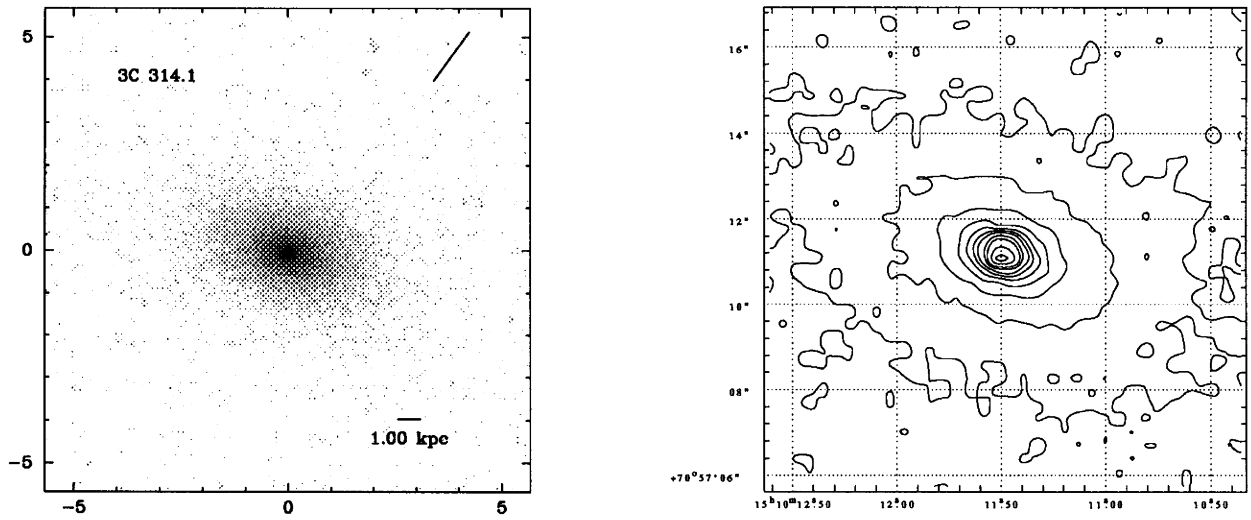

FIG. 56.—(*Left*) 3C 314.1, $z = 0.1197$. (*Right*) Contour levels: 0.5, 1, 2, 3, 4, 5, 6, 8, 10, 15, 20 × 1.866 × 10^{-18} ergs s^{-1} cm^{-2} $Å^{-1}$ $pixel^{-1}$.

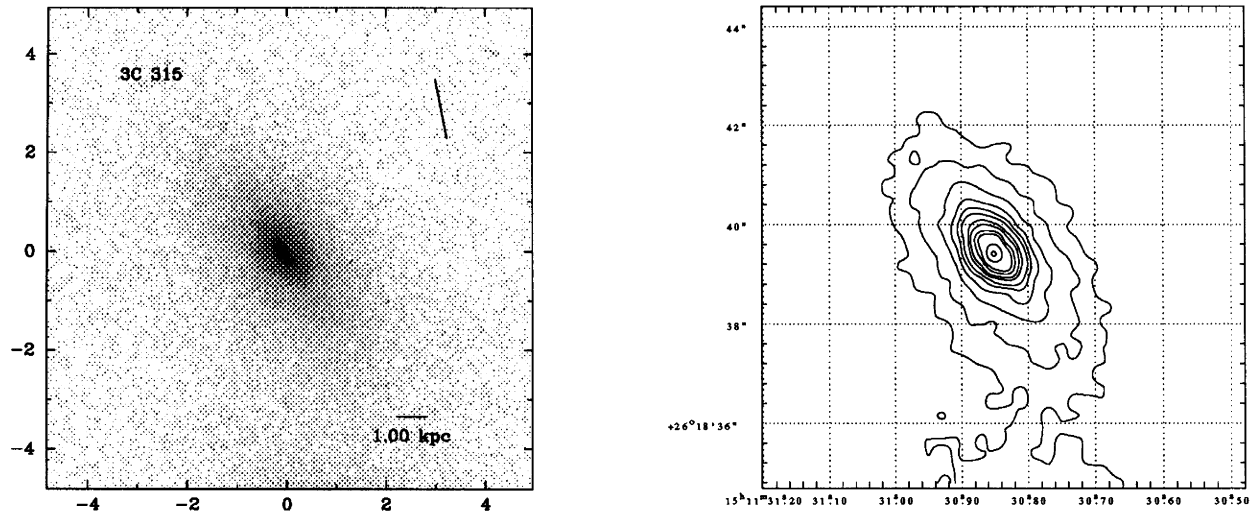

FIG. 57.—(*Left*) 3C 315, $z = 0.1083$. (*Right*) Contour levels: 1.4, 2, 3, 4, 5, 6, 8, 10, 15, 20, 40, 60, 80 × 1.866 × 10^{-18} ergs s^{-1} cm^{-2} $Å^{-1}$ $pixel^{-1}$.

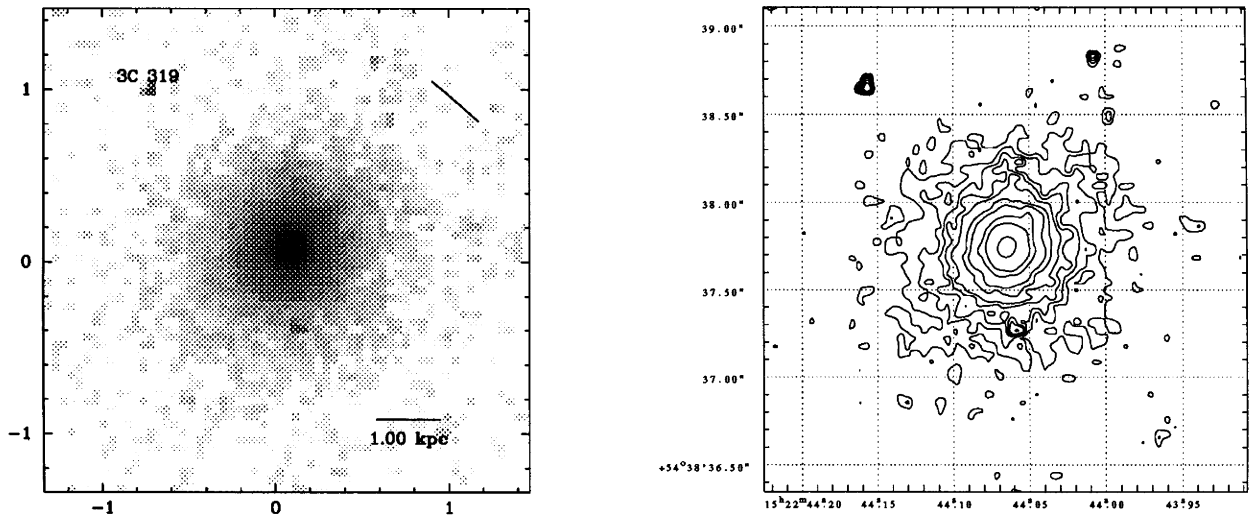

FIG. 58.—(*Left*) 3C 319, $z = 0.192$. (*Right*) Contour levels: 2, 3, 4, 5, 6, 8, 10, 15, 20, 40, 60 × 1.866 × 10^{-18} ergs s^{-1} cm^{-2} $Å^{-1}$ $pixel^{-1}$.

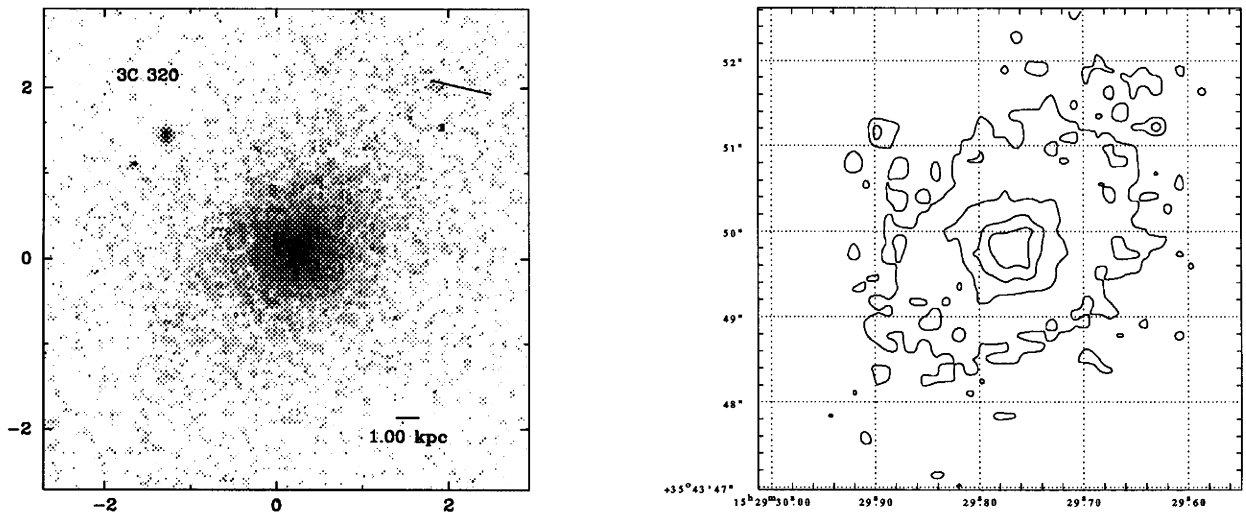

FIG. 59.—(*Left*) 3C 320, $z = 0.342$. (*Right*) Contour levels: 1, 2, 3, 4, 5 × 1.866 × 10^{-18} ergs s^{-1} cm^{-2} $Å^{-1}$ $pixel^{-1}$.

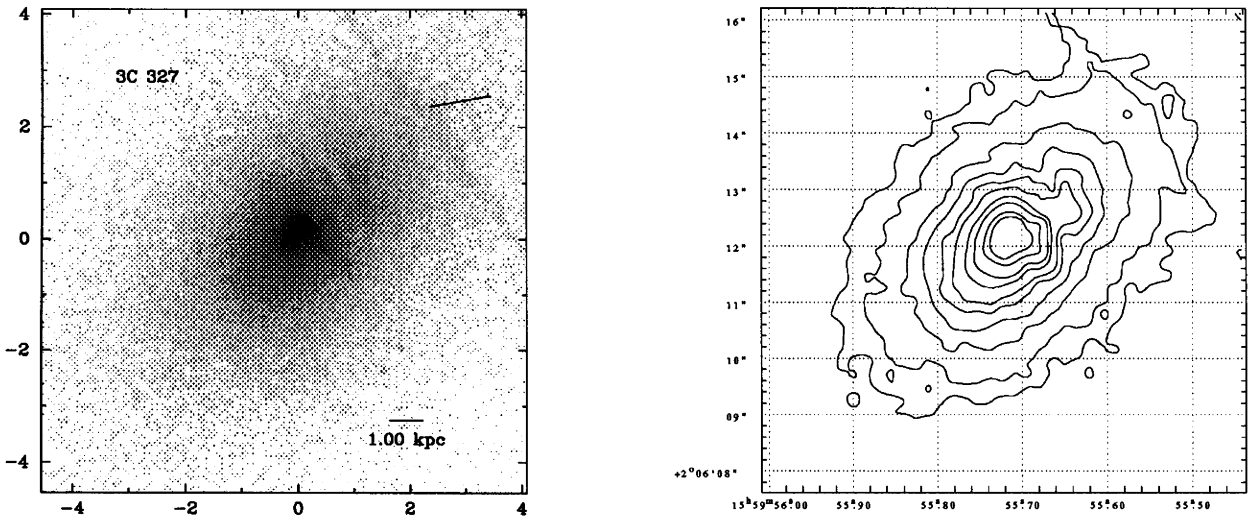

FIG. 60.—(*Left*) 3C 327, $z = 0.1039$. (*Right*) Contour levels: 1.5, 2, 3, 4, 5, 6, 8, 10, 15, 20 × 1.866 × 10^{-18} ergs s^{-1} cm^{-2} $Å^{-1}$ $pixel^{-1}$.

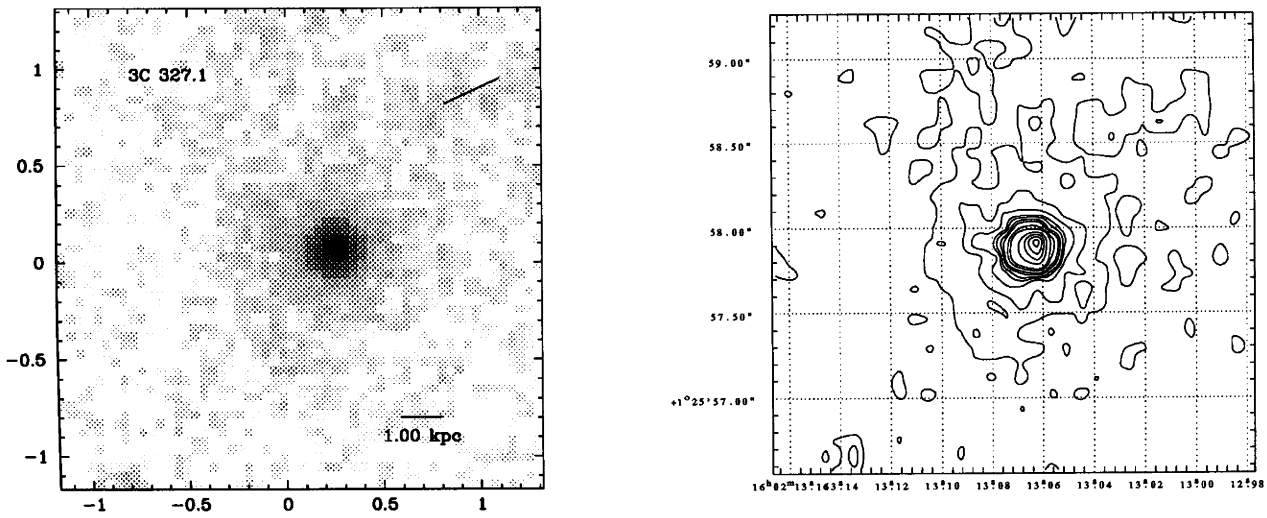

FIG. 61.—(*Left*) 3C 327.1, $z = 0.4268$. (*Right*) Contour levels: 2, 3, 4, 5, 6, 8, 10, 15, 20, 40, 60, 80, 100 × 10^{-18} ergs s^{-1} cm^{-2} $Å^{-1}$ $pixel^{-1}$.

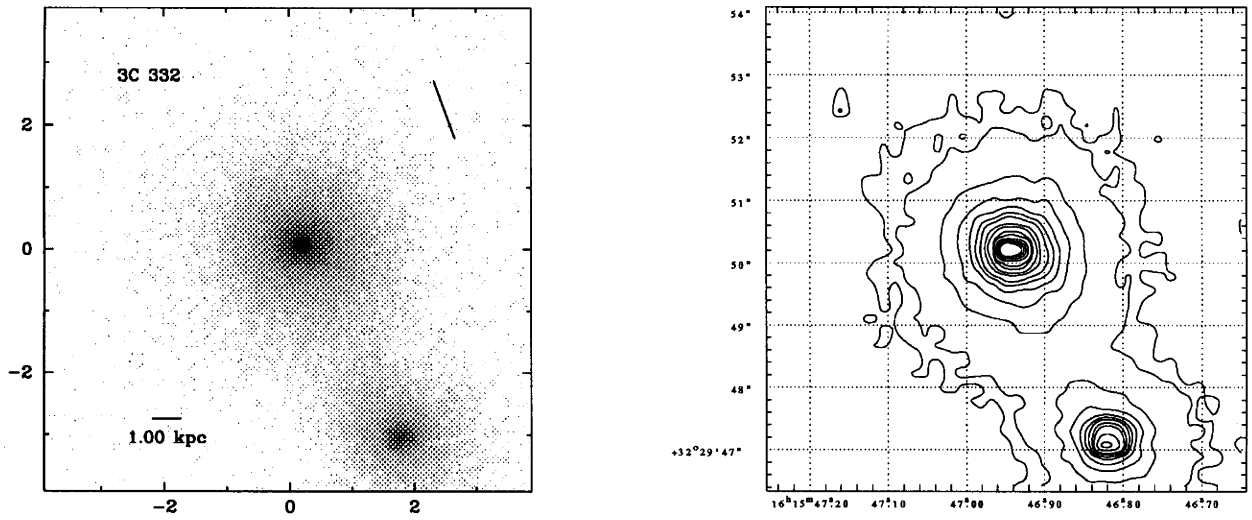

FIG. 62.—(*Left*) 3C 332, $z = 0.1515$. (*Right*) Contour levels: 0.75, 1, 2, 3, 4, 5, 6, 8, 10, 15, 20, 40, 60, 80 × 1.866 × 10^{-18} ergs s^{-1} cm^{-2} $Å^{-1}$ $pixel^{-1}$.

3C 223, $z = 0.1368$.—This galaxy is a member of a group of galaxies (Sandage 1972). The *HST* image shows a galaxy nucleus that is slightly elongated. There is some faint structure around it.

3C 223.1, $z = 0.1075$.—The image shows a beautiful central bulge with a dusty disk. This galaxy hosts an X-shaped radio source. The weaker radio emission is perpendicular to the dust disk, and the direction of the stronger radio lobes is indicated by the bar (Black et al. 1992).

3C 234, $z = 0.1848$.—This galaxy is a broad-line radio galaxy (McCarthy et al. 1995). There are features emanating from the nucleus in the east and west direction. This galaxy is known to have strong extended emission lines which are likely to be influencing the apparent morphology.

3C 244.1, $z = 0.428$.—This galaxy lies in a cluster of galaxies (Hill & Lilly 1991; McCarthy et al. 1995). The *HST* image shows an elliptical galaxy nucleus with some structure north of it. This object is known to have strong emission lines (Spinrad et al. 1985).

3C 258, $z = 0.165$.—The image shows a highly curved, irregular object and a disturbed companion to the north. These objects appear to be members of a small group. The irregularities may be due to a merger or a recent tidal interaction.

3C 268.2, $z = 0.362$.—The image shows a very elongated narrow host galaxy. The object has strong extended emission-line regions which are likely to be influencing the apparent morphology.

3C 268.3, $z = 0.371$.—On both sides of the nucleus, tails of emission extend out. The object is known to have strong emission lines. There is a feature that is a candidate for an optical jet. The radio source is elongated in the same direction (Akujor et al. 1991). This radio galaxy lies in a cluster of galaxies (Hill & Lilly 1991).

3C 274.1, $z = 0.422$.—This radio galaxy lies in a cluster of galaxies (Yates, Miller, & Peacock 1989).

3C 275, $z = 0.48$.—The nucleus appears to consist of two patches of emission. Some faint tails of emission extend out in the direction of the radio axis. This radio galaxy lies in a cluster of galaxies (Yates et al. 1989).

3C 277, $z = 0.414$.—The *HST* image shows that the galaxy is elongated in the eastwest direction, in the same direction as the axis of the radio source.

3C 284, $z = 0.2395$.—This galaxy lies in a moderately rich

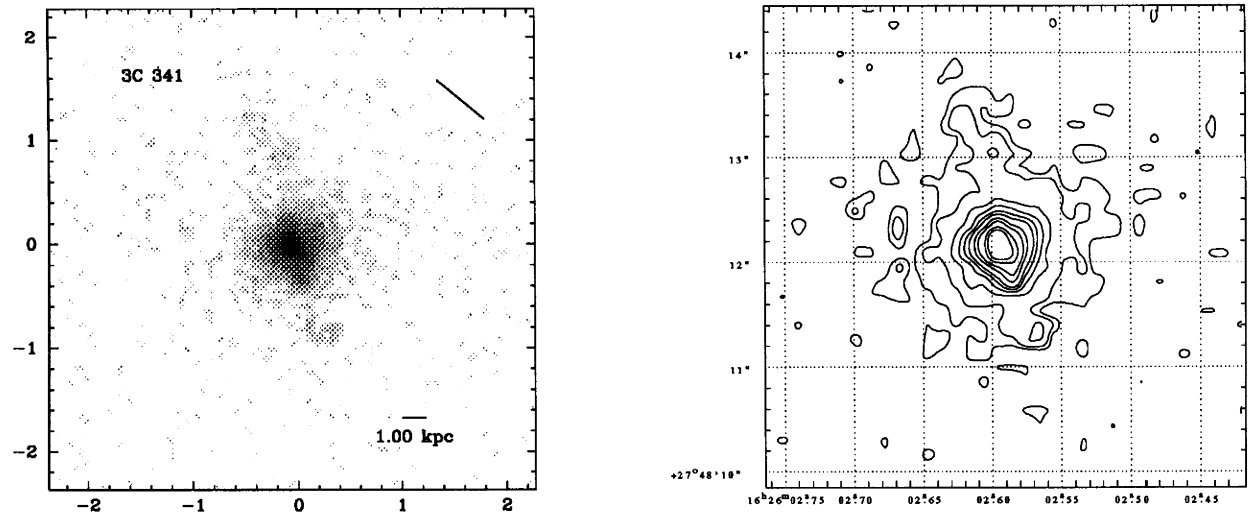

FIG. 63.—(*Left*) 3C 341, $z = 0.448$. (*Right*) Contour levels: 1.5, 2, 3, 4, 5, 6, 8, 10, 15, 20, 40 × 1.866 × 10^{-18} ergs s^{-1} cm^{-2} $Å^{-1}$ $pixel^{-1}$.

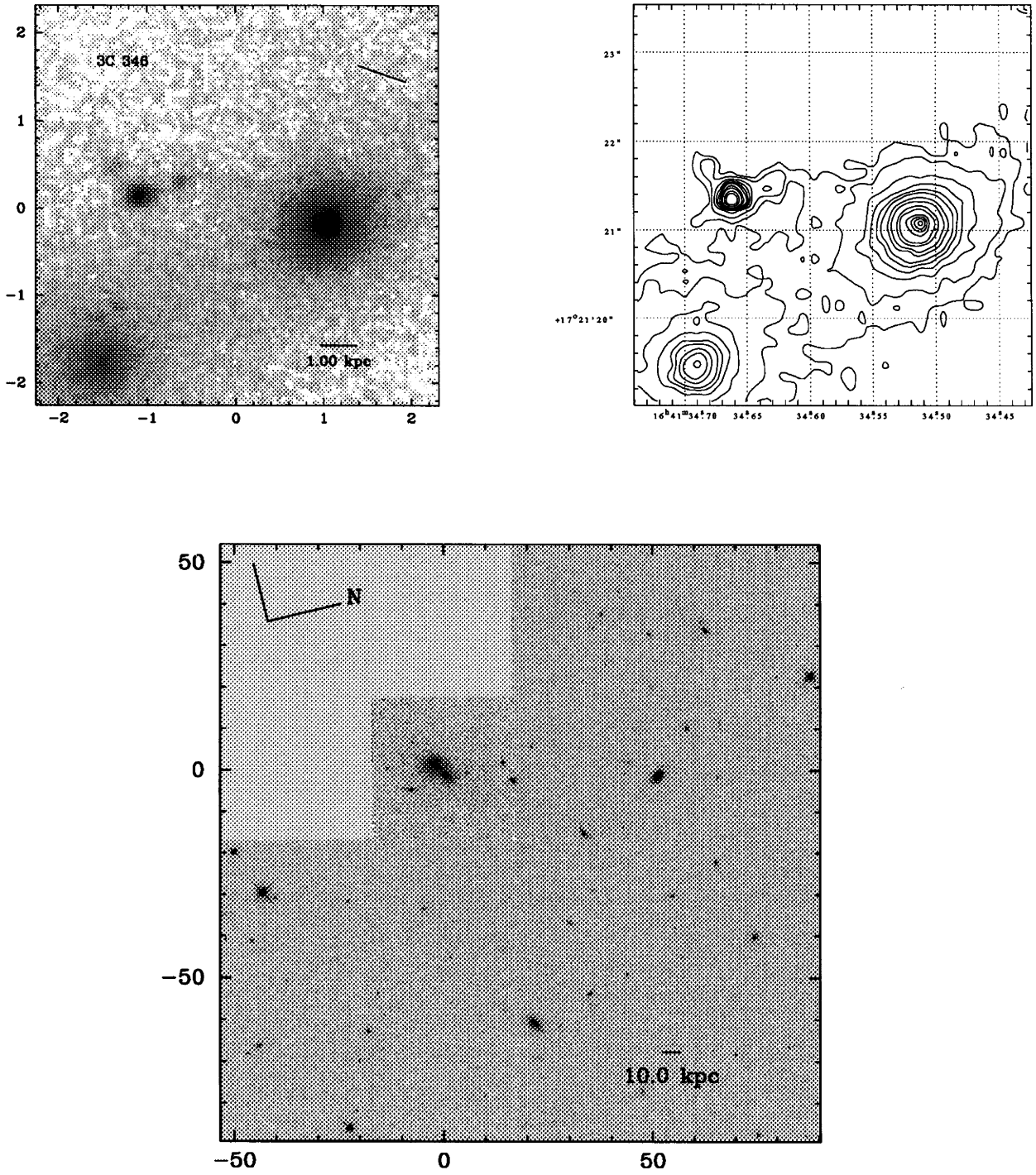

FIG. 64.—(*Left*) 3C 346, $z = 0.161$. (*Right*) Contour levels: 1.5, 2, 3, 4, 5, 6, 8, 10, 15, 20, 40, 60, 80, 100 × 1.866×10^{-18} ergs s^{-1} cm^{-2} $Å^{-1}$ $pixel^{-1}$. (*Bottom*) Wide field.

cluster (McCarthy et al. 1995). The *HST* image shows that the nucleus appears to consists of two parts, which is probably due to dust obscuration. The image shows two tails of emission in northeast and southwest directions. The radio axis points in roughly the same direction as the major axis of the nucleus (Leahy & Williams 1984).

3C 287.1, $z = 0.2159$.—This N galaxy shows a patch of emission close to the nucleus at a distance of less than 1 kpc.

3C 288, $z = 0.246$.—The diffuse nucleus of the galaxy appears to be double. A radio image by Bridle et al. (1989) shows no obvious connection with the optical image. Two globulars appear very near to the galaxy nucleus.

3C 299, $z = 0.367$.—The image shows a distorted galaxy. Three patches of emission and much filamentary emission are visible. A radio image at similar spatial resolution (Spencer et al. 1991) shows a northeast elongated radio structure.

3C 300, $z = 0.27$.—This object lies in a cluster of galaxies (McCarthy et al. 1995). The *HST* image shows an elliptical nucleus with indication of substructure. There is a patch of emission east of the galaxy nucleus.

3C 303, $z = 0.141$.—The image of this N galaxy shows a compact nucleus. The galaxy has strong emission lines.

3C 303.1, $z = 0.267$.—The nucleus of the galaxy appears

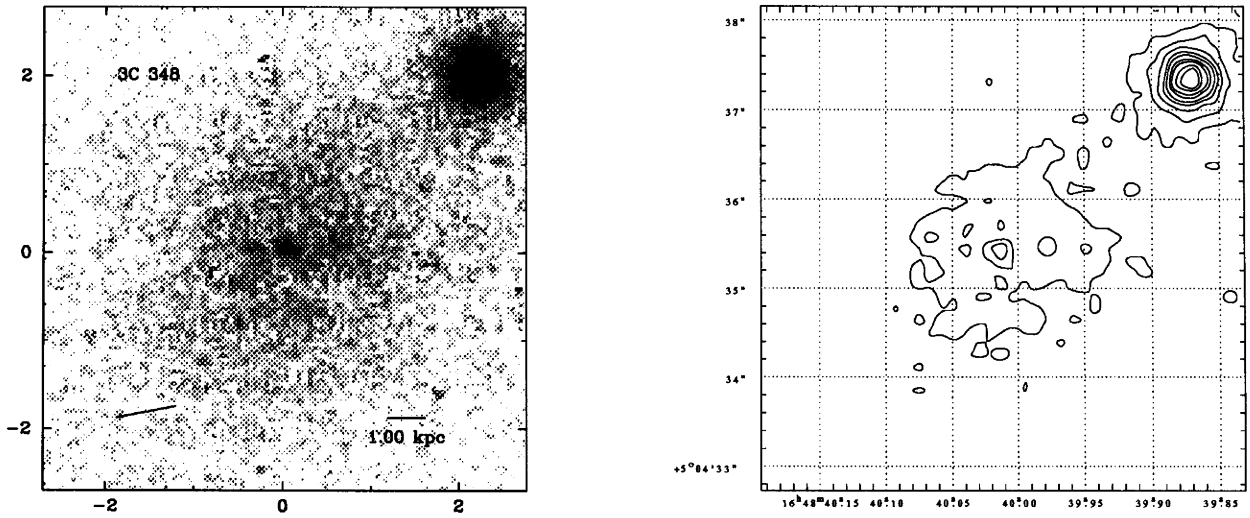

FIG. 65.—(*Left*) 3C 348, $z = 0.154$. (*Right*) Contour levels: 2, 3, 4, 5, 6, 8, 10, 15, 20, 40 × 1.866 × 10^{-18} ergs s^{-1} cm^{-2} $Å^{-1}$ $pixel^{-1}$.

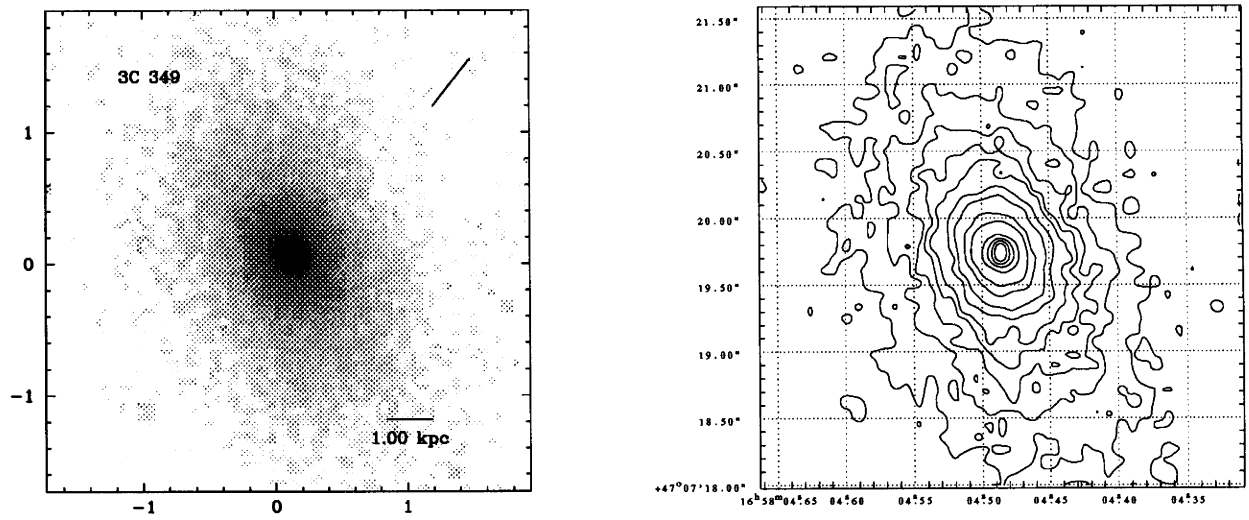

FIG. 66.—(*Left*) 3C 349, $z = 0.205$. (*Right*) Contour levels: 2, 3, 4, 5, 6, 8, 10, 15, 20, 40, 60, 80, 100 × 1.866 × 10^{-18} ergs s^{-1} cm^{-2} $Å^{-1}$ $pixel^{-1}$.

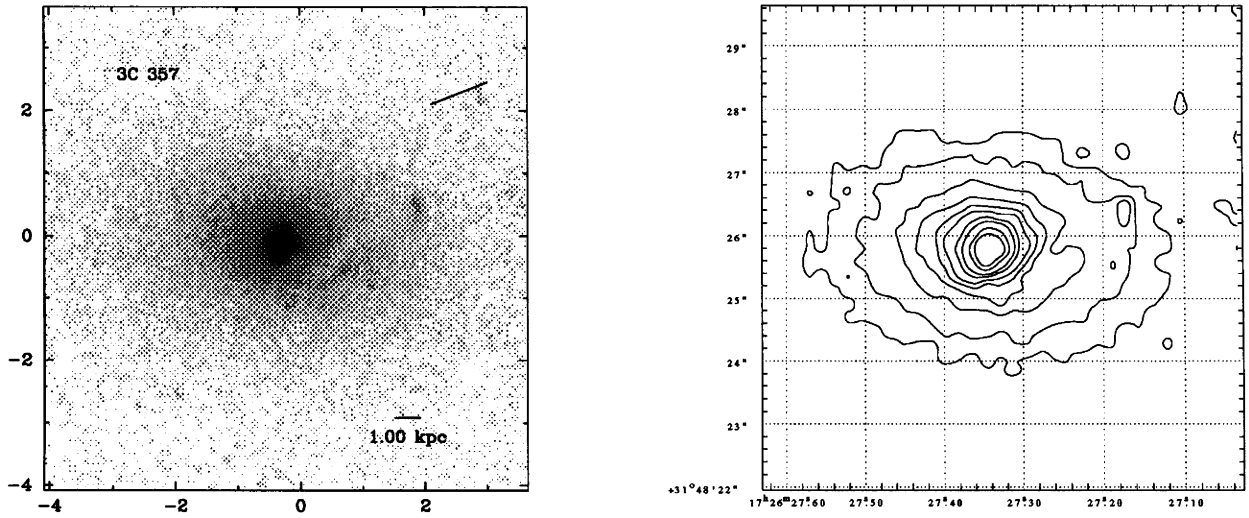

FIG. 67.—(*Left*) 3C 357, $z = 0.1664$. (*Right*) Contour levels: 1.5, 2, 3, 4, 5, 6, 8, 10, 15, 20, 40 × 1.866 × 10^{-18} ergs s^{-1} cm^{-2} $Å^{-1}$ $pixel^{-1}$.

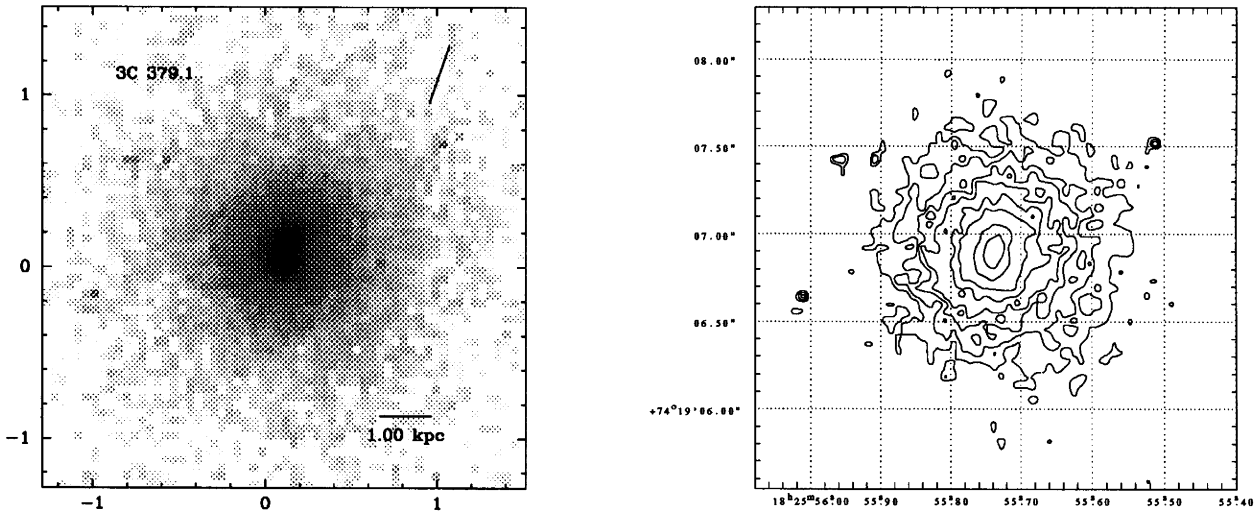

FIG. 68.—(*Left*) 3C 379.1, $z = 0.256$. (*Right*) Contour levels: 3, 4, 5, 6, 8, 10, 15, 20, 40 × 1.866 × 10^{-18} ergs s^{-1} cm^{-2} $Å^{-1}$ $pixel^{-1}$.

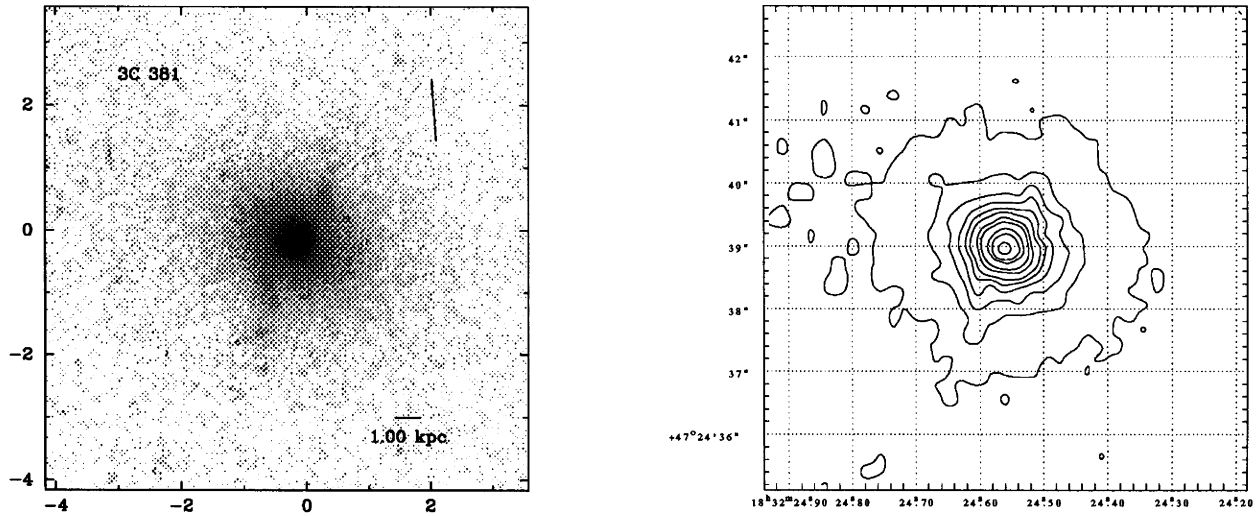

FIG. 69.—(*Left*) 3C 381, $z = 0.1605$. (*Right*) Contour levels: 1, 2, 3, 4, 5, 6, 8, 10, 20, 40, 60 × 1.866 × 10^{-18} ergs s^{-1} cm^{-2} $Å^{-1}$ $pixel^{-1}$.

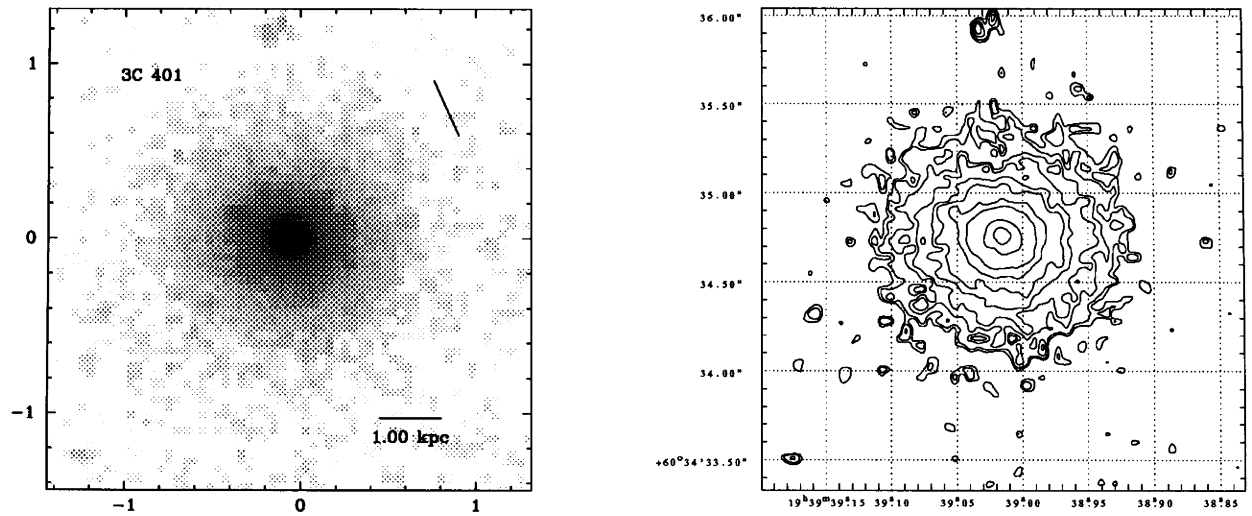

FIG. 70.—(*Left*) 3C 401, $z = 0.201$. (*Right*) Contour levels: 2.5, 3, 4, 5, 6, 8, 10, 15, 20, 40 × 1.866 × 10^{-18} ergs s^{-1} cm^{-2} $Å^{-1}$ $pixel^{-1}$.

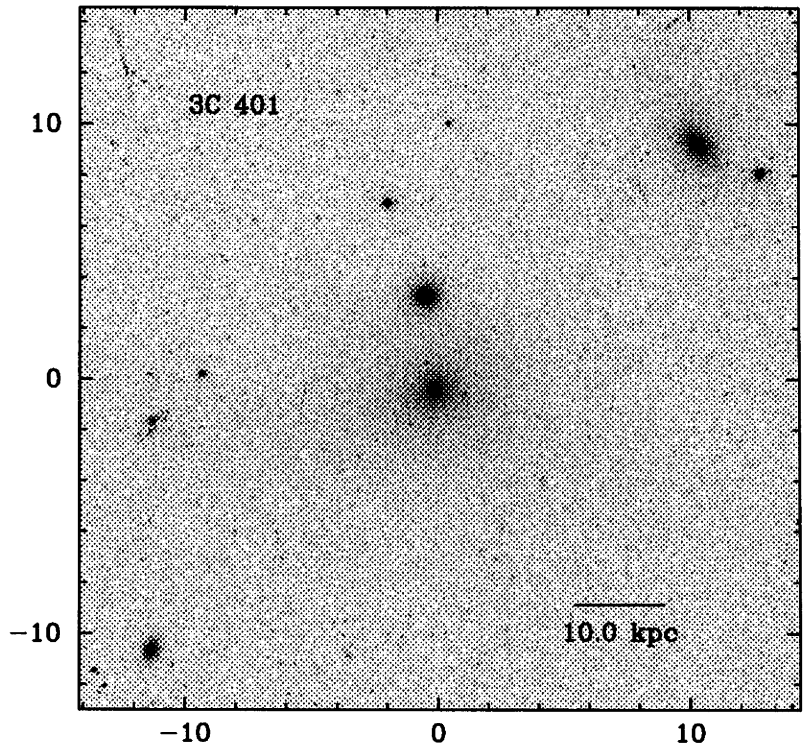

FIG. 71.—3C 401, $z = 0.201$, widefield

to consist of three or four components. The emission lies in the same direction as the radio emission.

3C 306.1, $z = 0.441$.—The *HST* image shows a nucleus that is partly obscured by dust. This radio galaxy is a member of a cluster of galaxies (Yates et al. 1989).

3C 313, $z = 0.461$.—This elliptical galaxy hosts a fairly large radio source ($LAS \sim 130''$) (Bogers et al. 1994). The galaxy nucleus is surrounded by patches of emission. The radio galaxy is a member of a cluster of galaxies (Hill & Lilly 1991).

3C 314.1, $z = 0.1197$.—The image shows an elliptical nucleus.

3C 315, $z = 0.1083$.—The image shows that the galaxy nucleus is highly elongated, and some substructure is seen. This radio galaxy is a member of a pair of galaxies. It hosts an X-shaped radio source.

3C 319, $z = 0.192$.—Some faint emission is apparent to the northwest of the nucleus.

3C 320, $z = 0.342$.—The image shows a diffuse elliptical galaxy, showing no obvious signs of substructures.

3C 327, $z = 0.1039$.—The image shows extensive dust lanes northwest of the galaxy nucleus. The radio axis lies perpendicular to these two dust lanes. The nuclear structure is complex.

3C 327.1, $z = 0.4628$.—This image shows an elliptical nucleus with a faint halo of emission around it. This galaxy has strong emission lines (Spinrad et al. 1985).

3C 332, $z = 0.1515$.—The image shows a smooth elliptical nuclear region and appears to be a member of a close pair.

3C 341, $z = 0.448$.—The image shows a distorted nucleus. Some emission extends to the north and south. The radio

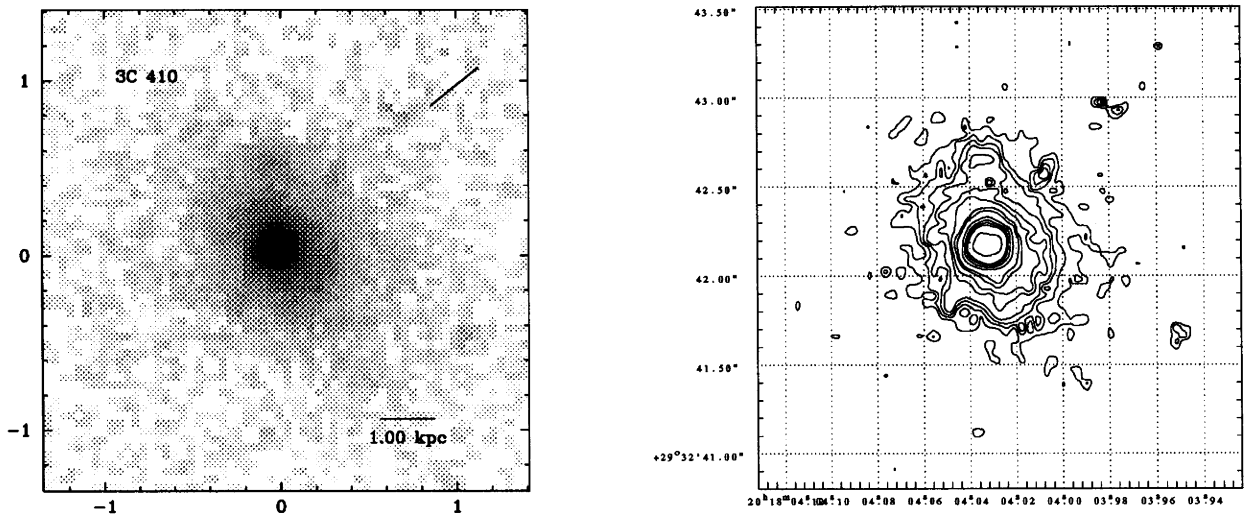

FIG. 72.—(*Left*) 3C 410, $z = 0.2485$. (*Right*) Contour levels: 3, 4, 5, 6, 8, 10, 15, 20, 40, 60, 80, 100, 200, 400 × 1.866 × 10^{-18} ergs s^{-1} cm^{-2} $Å^{-1}$ $pixel^{-1}$.

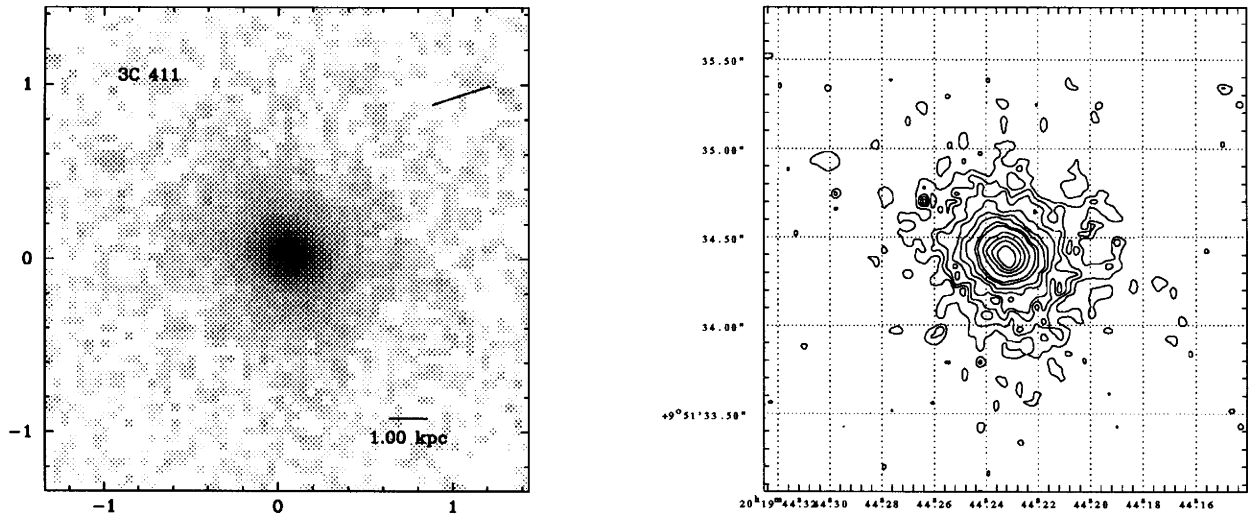

FIG. 73.—(*Left*) 3C 411, $z = 0.467$. (*Right*) Contour levels: 3, 4, 5, 6, 8, 10, 15, 20, 40, 60, 80, 100, 200 × 1.866 × 10^{-18} ergs s^{-1} cm^{-2} $Å^{-1}$ $pixel^{-1}$.

axis makes a small angle with the major axis of the elongated nucleus.

3C 346, $z = 0.161$.—Dey & van Breugel (1994) found blue optical continuum associated with a radio knot in this galaxy. Our image resolves this knot into a curved optical synchrotron jet and triple hot spot perfectly coinciding with the radio emission. There is a companion galaxy.

3C 348, $z = 0.154$.—3C 348, Hercules A, appears as an extremely diffuse low surface brightness galaxy with indication of absorbing dust in the shape of two rings. There is a nearby bright emission patch.

3C 349, $z = 0.205$.—This image shows an elliptical galaxy.

3C 357, $z = 0.1664$.—The image shows a galaxy with chaotic, filamentary dust lanes southwest of the nucleus. On the west side of the dust there is a patch of emission.

3C 379.1, $z = 0.256$.—The nucleus of this diffuse source is elongated along the radio axis.

3C 381, $z = 0.1605$.—The *HST* image shows an elliptical galaxy with two tails of emission pointing north and south. The radio axis runs approximately in the same direction as the tails (Leahy & Perley 1991). The galaxy is a broad-line radio galaxy (McCarthy et al. 1995).

3C 401, $z = 0.201$.—The *HST* image shows that this galaxy is part of a group of galaxies. The radio emission (Laing 1981) shows elongated structure in the same direction as the extended optical emission.

3C 410, $z = 0.2485$.—The image shows an elliptical nucleus with some faint emission around it. There is an extension toward the south in the same direction as the radio jet. This feature is a candidate for an optical jet.

3C 411, $z = 0.467$.—The image of this N galaxy shows an compact nucleus. The radio image shows a classical radio double.

3C 424, $z = 0.127$.—The image shows a slightly asymmetric elliptical nucleus. The wide field image shows a nearby cluster of galaxies.

3C 433, $z = 0.1016$.—This object lies in a cluster (McCarthy et al. 1995). The *HST* image shows a galaxy full of filaments of dust and possible regions of star formation. There is a faint patch of emission northwest of the galaxy coinciding with a spot of radio emission. The radio mor-

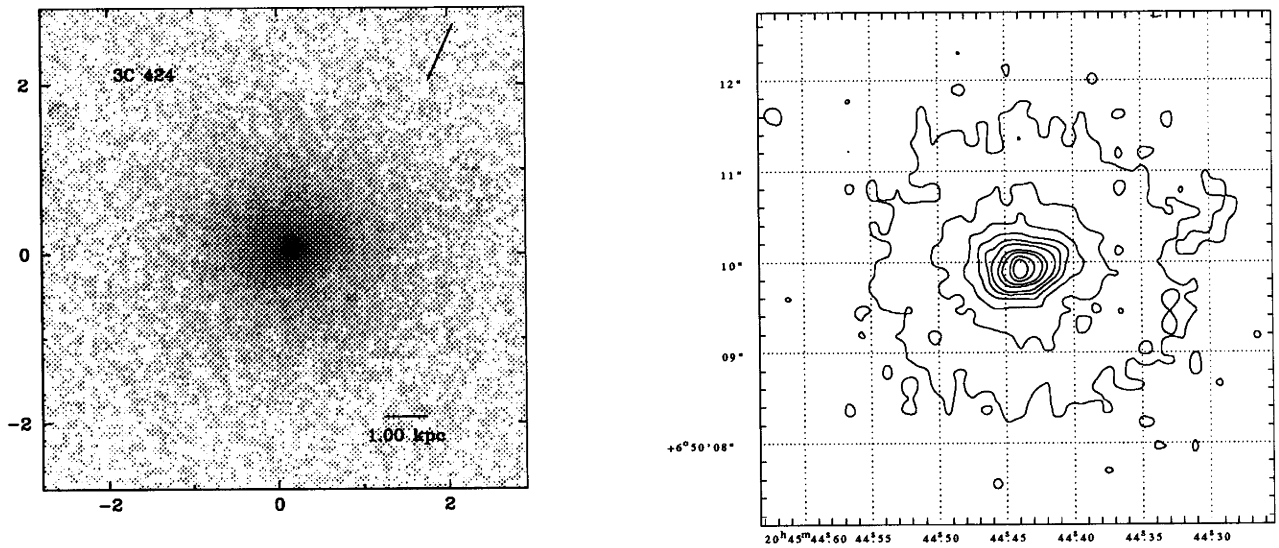

FIG. 74.—(*Left*) 3C 424, $z = 0.127$. (*Right*) Contour levels: 1, 2, 3, 4, 5, 6, 8, 10, 15, 20 × 1.866 × 10^{-18} ergs s^{-1} cm^{-2} $Å^{-1}$ $pixel^{-1}$.

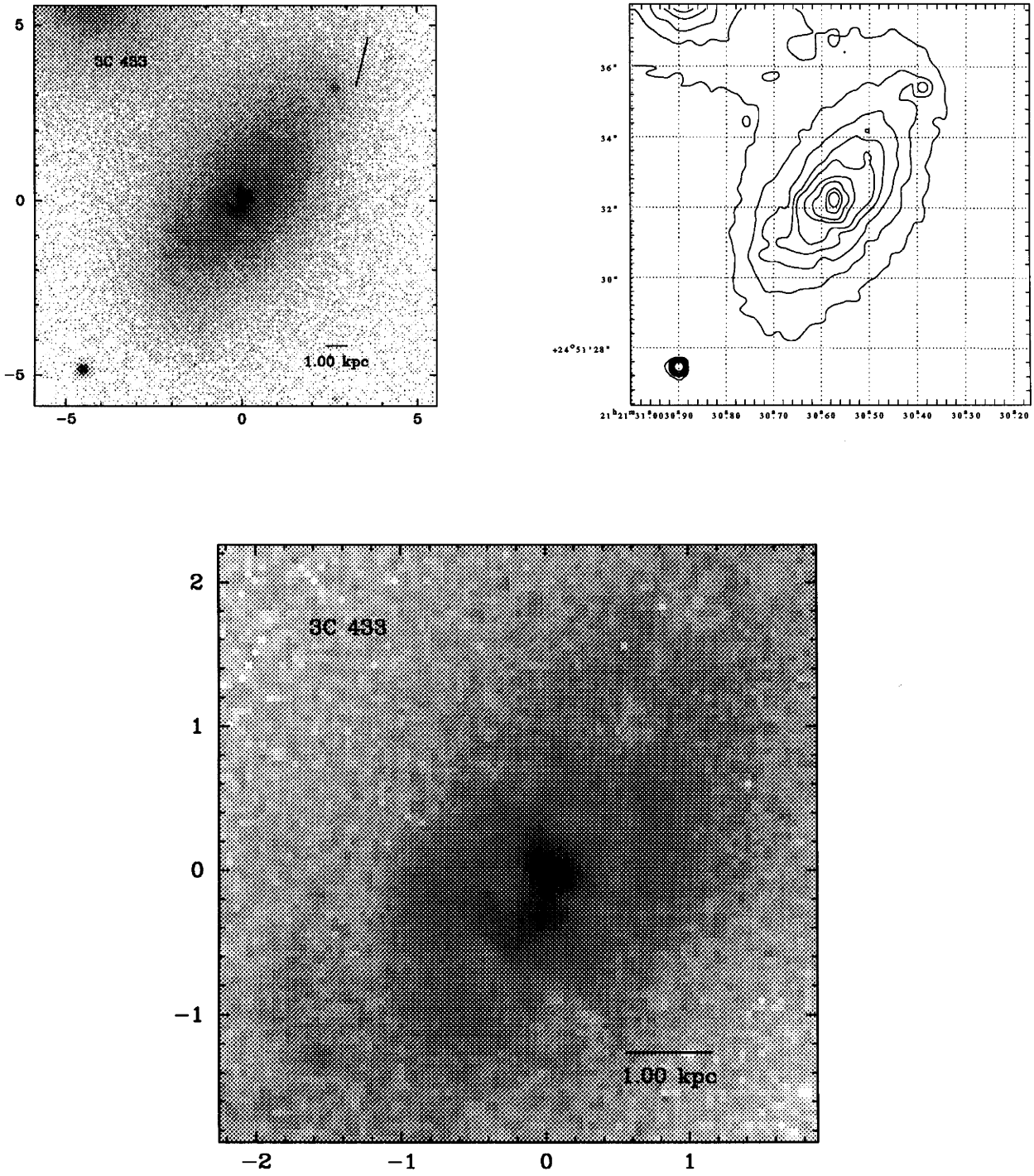

FIG. 75.—(*Left*) 3C 433, $z = 0.1016$. (*Right*) Contour levels: 2, 3, 4, 5, 6, 8, 10, 15, 20, 40 × 1.866 × 10^{-18} ergs s^{-1} cm^{-2} $Å^{-1}$ $pixel^{-1}$. (*Bottom*) Blow-up of central region.

phology (Black et al. 1992) shows a jet pointing to the north.

3C 434, $z = 0.322$.—The *HST* image shows an elliptical nucleus, slightly elongated in southeast direction. This radio galaxy lies in an average density environment (Yates et al. 1989).

3C 435A, $z = 0.471$.—The nucleus of this galaxy appears to have some structure. The radio emission lies in the direction of the optical major axis (McCarthy, van Breugel, & Spinrad 1989). This galaxy has two close companions.

3C 436, $z = 0.2145$.—This image shows a nucleus with dust features. Some filamentary emission is seen around the core.

3C 438, $z = 0.29$.—The *HST* image shows a diffuse nucleus that has structure. The object is a member of a cluster of galaxies.

3C 456, $z = 0.233$.—The nucleus of this galaxy is elongated in eastwest direction, and it has a slightly distorted shape.

3C 459, $z = 0.2199$.—The image of this N galaxy shows a compact nucleus surrounded by blobs and tails of emission.

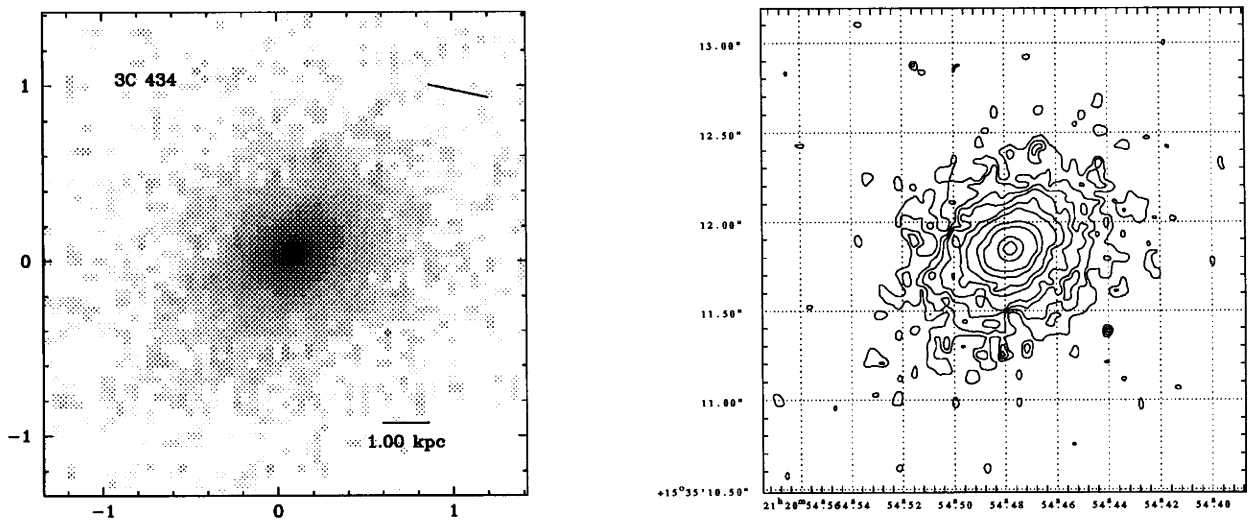

FIG. 76.—(*Left*) 3C 434, $z = 0.322$. (*Right*) Contour levels: 3, 4, 5, 6, 8, 10, 15, 20, 40, 60, 80 × 1.866 × 10^{-18} ergs s^{-1} cm^{-2} $Å^{-1}$ $pixel^{-1}$.

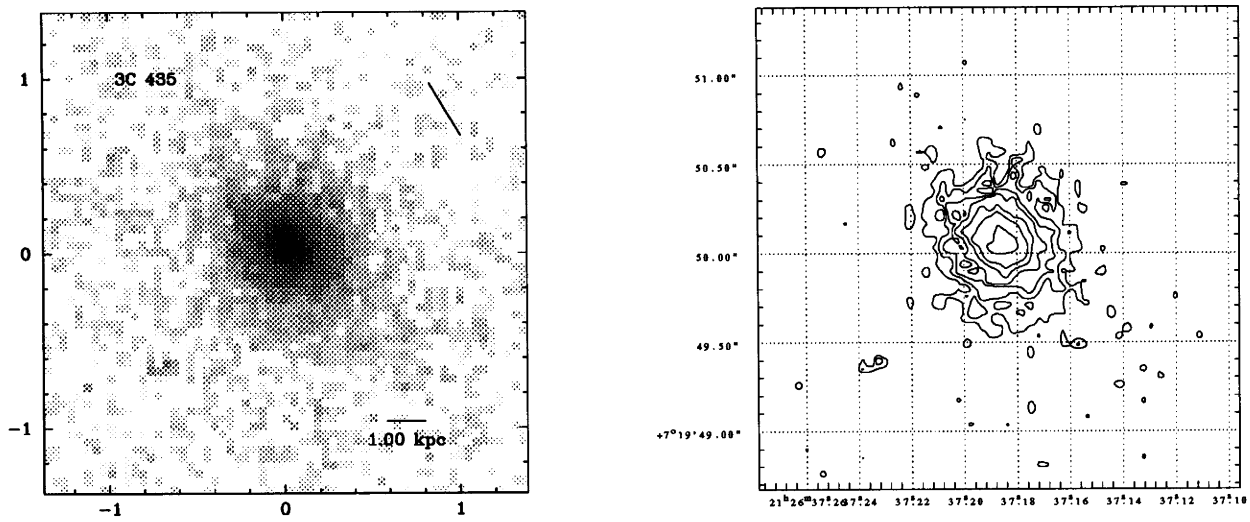

FIG. 77.—(*Left*) 3C 435, $z = 0.471$. (*Right*) Contour levels: 3, 4, 5, 6, 8, 10, 15, 20 × 1.866 × 10^{-18} ergs s^{-1} cm^{-2} $Å^{-1}$ $pixel^{-1}$.

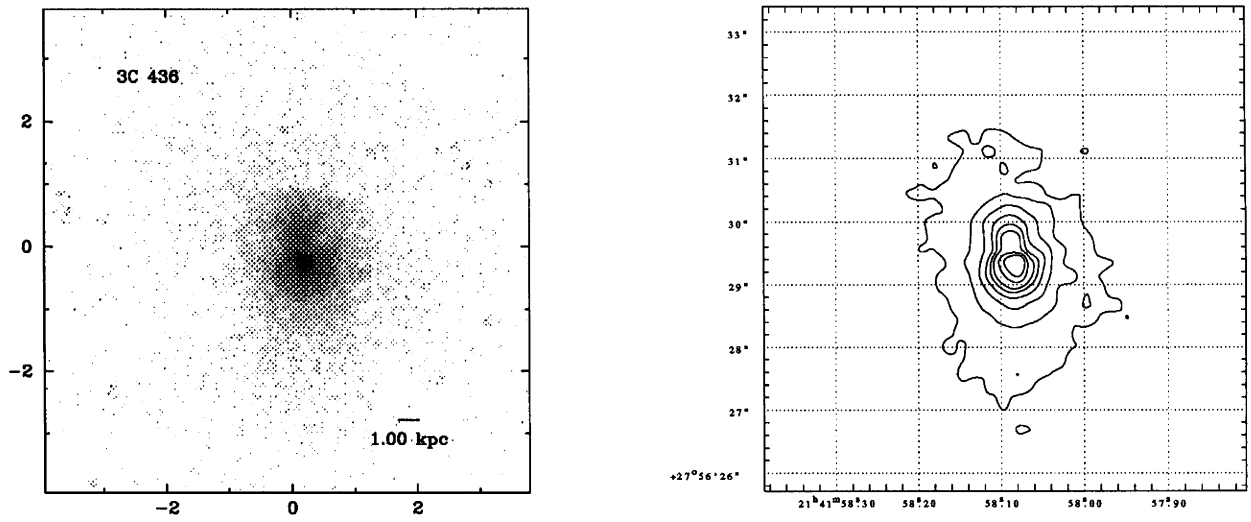

FIG. 78.—(*Left*) 3C 436, $z = 0.2145$. (*Right*) Contour levels: 1, 2, 3, 4, 5, 6, 8, 10 × 1.866 × 10^{-18} ergs s^{-1} cm^{-2} $Å^{-1}$ $pixel^{-1}$.

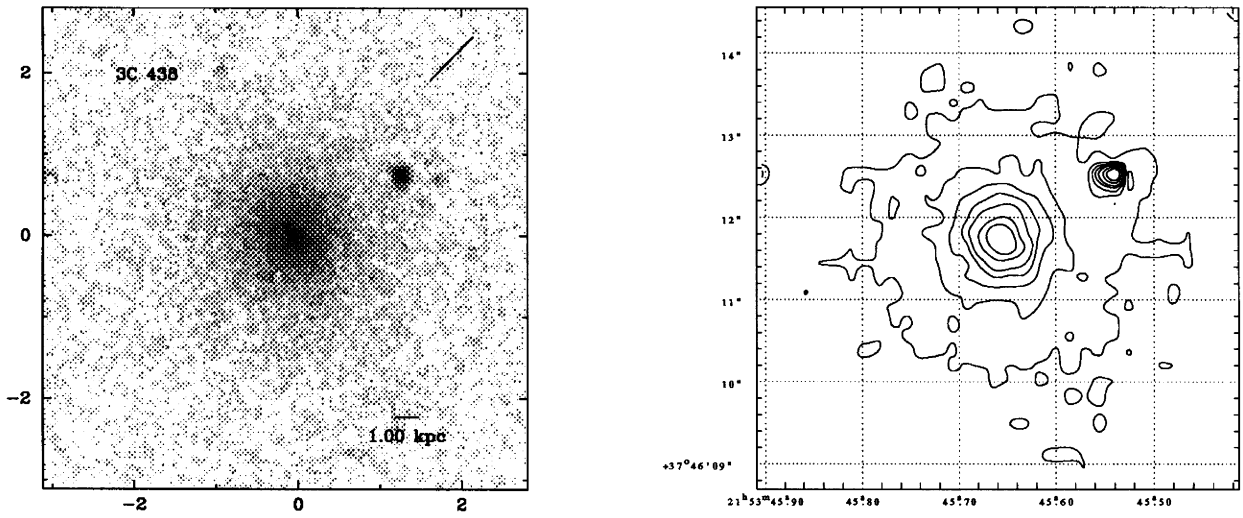

FIG. 79.—(*Left*) 3C 438, $z = 0.29$. (*Right*) Contour levels: 2, 3, 4, 5, 6, 8, 10, 15 × 1.866 × 10^{-18} ergs s^{-1} cm^{-2} $Å^{-1}$ $pixel^{-1}$.

One patch of emission east of the nucleus coincides with the radio emission (Morganti et al. 1993).

3C 460, $z = 0.268$.—The image shows a galaxy that consists of two components ~4 kpc apart. The radio axis lies along the direction of the optical major axis of the galaxy.

5. CONCLUDING REMARKS

We have used *HST* WFPC2 to image 267 3CR radio galaxies and quasars. Here we presented the 77 radio galaxies in the intermediate ($0.1 < z < 0.5$) redshift range. In future papers we will present the radio galaxies in the redshift ranges $z < 0.1$, $z > 0.5$, and the quasars, and we defer numerical and statistical results of these observations and their implications to future works. However, a few qualitative remarks can be made here.

We find that at least 30% of the galaxies in the redshift range $0.1 < z < 0.5$ have cores with disturbed morphologies. It is clear that in several cases dust is strongly influencing the appearance of the galaxy core, at least out to a redshift of order 0.5, although additional factors such as bursts of star formation and merging nuclei may be contributing to the disturbed morphologies. Additional observations at other wavelengths will help identify such cases and will allow us to estimate the reddening caused by dust.

Throughout the redshift range we see clumpy cores. This could be an indication for the merging of systems or similar

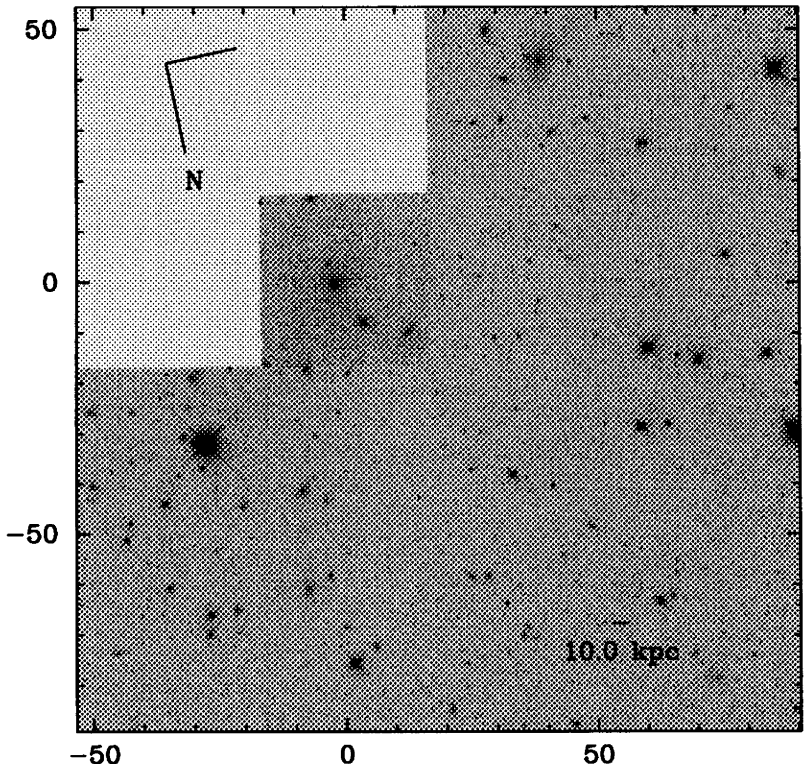

FIG. 80.—3C 438, wide field

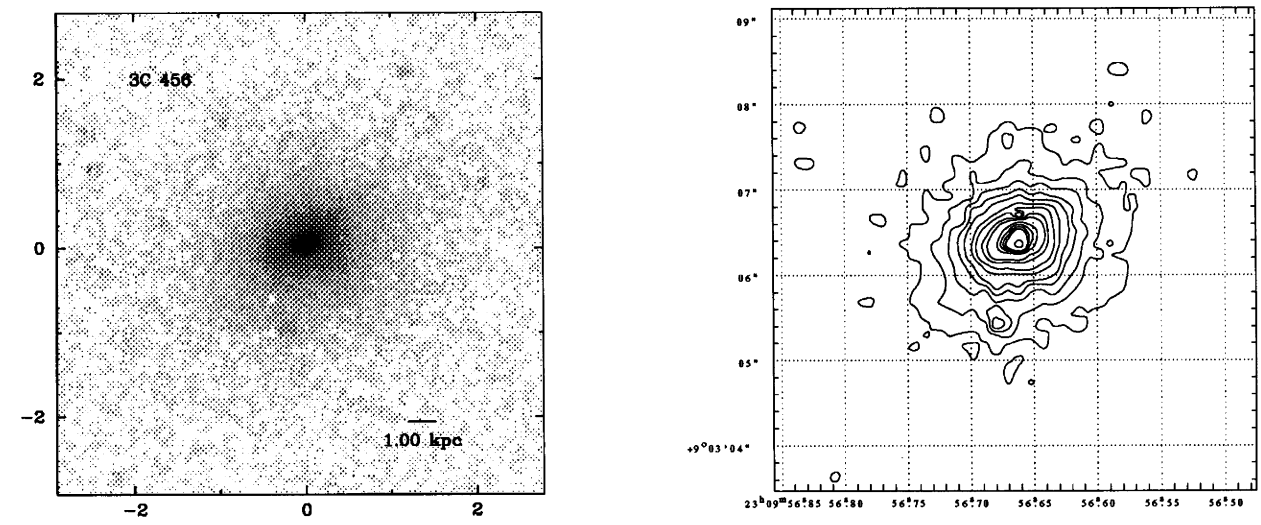

FIG. 81.—(*Left*) 3C 456, $z = 0.233$. (*Right*) Contour levels: 2, 3, 4, 5, 6, 8, 10, 15, 20, 40, 60, 80, 100, 200 × 1.866 × 10^{-18} ergs s^{-1} cm^{-2} $Å^{-1}$ $pixel^{-1}$.

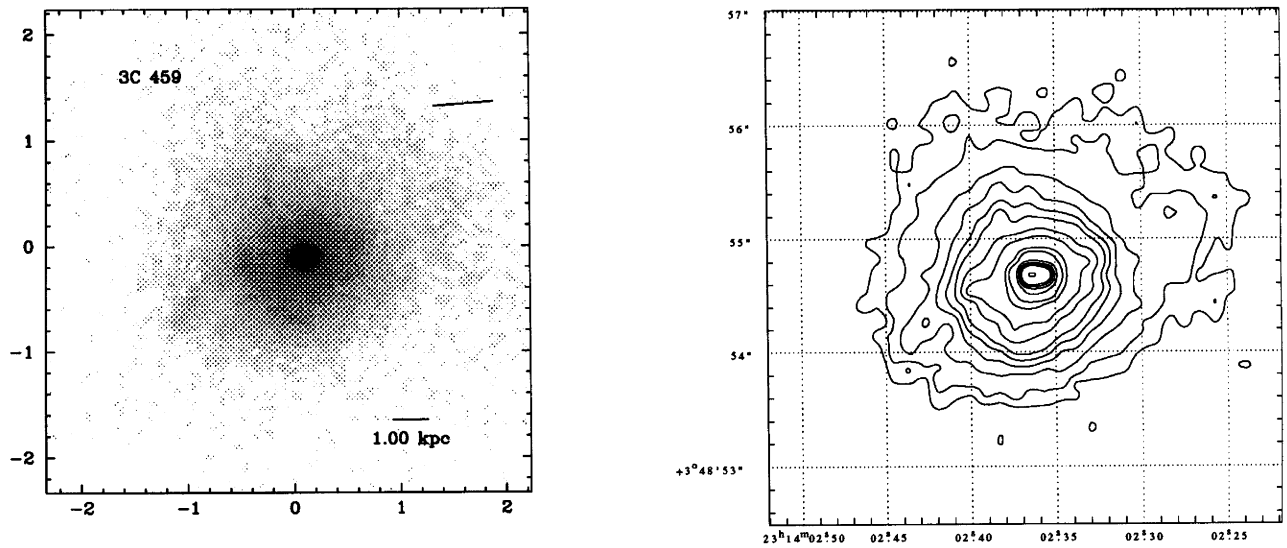

FIG. 82.—(*Left*) 3C 459, $z = 0.2199$. (*Right*) Contour levels: 1.5, 2, 3, 4, 5, 6, 8, 10, 15, 20, 40, 60, 80, 100, 200 × 1.866 × 10^{-18} ergs s^{-1} cm^{-2} $Å^{-1}$ $pixel^{-1}$.

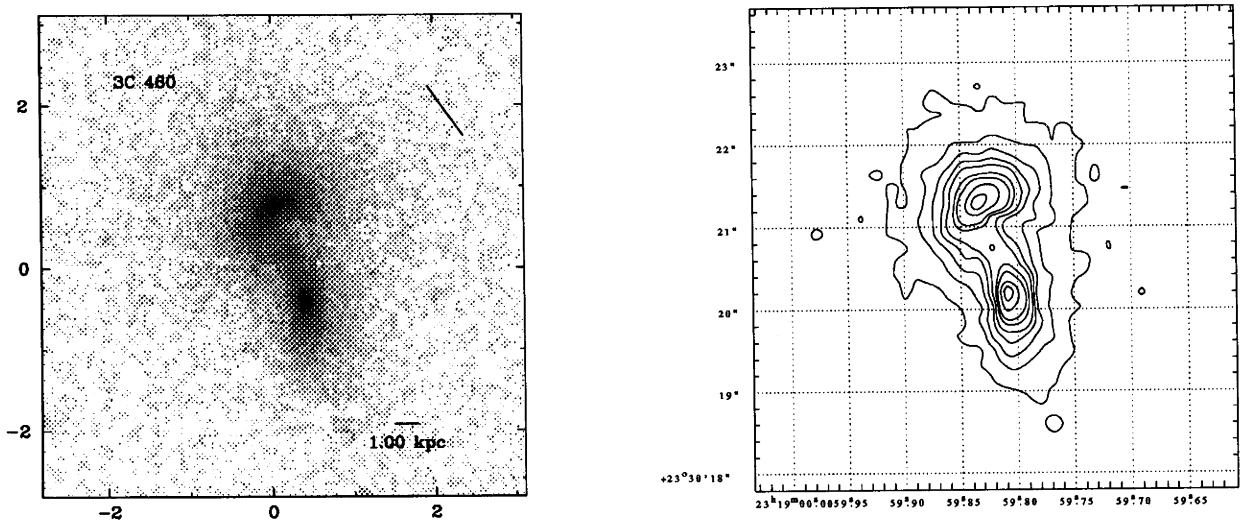

FIG. 83.—(*Left*) 3C 460, $z = 0.268$. (*Right*) Contour levels: 2, 3, 4, 5, 6, 8, 10, 15, 20, 40 × 1.866 × 10^{-18} ergs s^{-1} cm^{-2} $Å^{-1}$ $pixel^{-1}$.

dynamical activity. Some sources show tails of emission which is also an indication of the merging of systems. It is clear that our filter is contaminated with line emission throughout this redshift range; we may also therefore be witnessing a contribution from patches of ionized gas.

We find 13 candidates for optical synchrotron emission. The image of 3C 346 shows a curved optical jet and triple hot spot perfectly coinciding with the radio image. We find eight more candidates for optical synchrotron jets, where apparently linear features emanate from the nucleus in the approximate (in some cases, exact) direction of the radio source, and five candidates for optical hot spots where there is optical emission localized at the position of the radio hot spots. Detailed follow-up comparison to radio maps and optical polarization observations is required to determine if these candidates are, in fact, optical synchrotron emitters. Alternative possibilities for linear optical features and hot-spot emission include emission-line gas interacting with the radio jet, jet-induced star formation, and tidal tails.

In conclusion, we have presented the most basic data from this series of *HST* snapshot images of 3CR radio galaxies. The images have revealed a wealth of detail, including new optical jets, dust lanes, and multiple nuclei, and offer the prospect of enabling substantial progress to be made in the issues identified in the introductory section of this paper.

This research is supported by *HST* GO grant number GO-5476.01-93A.

REFERENCES

Akujor, C. E., Spencer, R. E., Zhang, F. J., Davis, R. J., Browne, I. W. A., & Fanti, C. 1991, MNRAS, 250, 215
Antonucci, R. R. 1985, ApJS, 59, 499
Baum, S. A., & Heckman, T. M. 1989, ApJ, 336, 702
Baum, S. A., Heckman, T., Bridle, A., van Breugel, W., & Miley, G. K. 1988, ApJS, 68, 643
Baum, S. A., Heckman, T. M., & van Breugel, W. 1992 ApJ, 389, 208
Baum, S. A., et al. 1994, *HST* Data Handbook
———. 1996, in preparation
Bennett, A. S. 1962a, MNRAS, 68, 163
———. 1962b, MNRAS, 125, 75
Biretta, J., Stern, C. P., & Harris, D. E. 1991, AJ, 101, 1632
Black, A. R. S., Baum, S. A., Leahy, J. P., Perley, R. A., Riley, J. M., & Scheuer, P. A. G. 1992, MNRAS, 256, 186
Bogers, W. J., Hes, R., Barthel, P. D., & Zensus, J. A. 1994, A&AS, 105, 91
Bridle, A. H., Fomalont, E. B., Byrd, G. G., & Valtonen, M. 1989, AJ, 97, 674
Burrows, C. J., et al. 1995, Wide Field and Planetary Camera 2 Instrument Handbook, ed. C. J. Burrows (Baltimore: STScI)
Chambers, K., Miley, G. K., & van Breugel, W. 1987, Nature, 329, 604
Crane, P., et al. 1993, ApJ, 402, L37
Dey, A., & van Breugel, W. 1994, AJ, 107, 1977
Djorgovski, S., Spinrad, H., McCarthy, P., Dickinson, M., van Breugel, W., & Strom, R. G. 1988, AJ, 96, 836
Dreher, J. W., & Feigelson, E. D. 1984, Nature, 308, 43
Feretti, L., Gioia, I. M., Giovannini, G., Gregorini, L., & Padrielli, L. 1984, A&A, 139, 50
Grandi, S. A., & Osterbrock, D. E. 1978, ApJ, 220, 783
Gregorini, L., et al. 1988, A&AS, 74, 107
Gregorini, L., & Bondi, M. 1989, A&A, 225, 333
Heckman, T., van Breugel, W., & Miley, G. K. 1984, ApJ, 286, 509
Hill, G. J., & Lilly, S. J. 1991, ApJ, 367, 1
Hiltner, P. R., Meisenheimer, K., Roser, H. J., Laing, R. A., & Perley, R. A. 1994, A&A, 286, 25
Holtzman, J. A., et al. 1995, PASP, 107, 156
Jenkins, C. J., Pooley, G. G., & Riley, J. M. 1977, MNRAS, 84, 61
Kotanyi, C. G., & Ekers, R. D. 1979, A&A, 73, L1
Laing, R. A. 1981, MNRAS, 195, 261
Laing, R. A., Riley, J. M., & Longair, M. S. 1983, MNRAS, 204, 151
Lawrence, C. R., Pearson, T. J., Readhead, A. C. S., & Unwin, S. C. 1986, AJ, 91, 494
Leahy, J. P., & Perley, R. A. 1991, AJ, 102, 537
Leahy, J. P., & Williams, A. G. 1984, MNRAS, 210, 929
Lilly, S. J., & Longair, M. S. 1984, MNRAS, 211, 833
Kristian, J. A., Sandage, A. R., & Katem, B. 1974, ApJ, 191, 43
Mathews, F. A., Morgan, W. W., & Schmidt, M. 1964, ApJ, 140, 35
McCarthy, P., et al. 1996, in preparation
McCarthy, P., Spinrad, H., & van Breugel, W. 1995, ApJS, 99, 27
McCarthy, P., van Breugel, W., & Spinrad, H. 1987 ApJ, 321, L29
———. 1989, AJ, 97, 36
McCarthy, P., van Breugel, W., & Kapahi, V. 1991, ApJ, 371, 478
Meisenheimer, K. 1991, in Physics of Active Galactic Nuclei, ed. W. Duschl & S. Wagner (Berlin: Springer), 525
Morganti, R., Killeen, N. E. B., & Tadhunter, C. N. 1993, MNRAS, 263, 1023
Owen, F. N., Hardee, P. E., & Bignell, R. C. 1980, ApJ, 239, L11
Pooley, G. G., Leahy, J. P., Shakeshaft, J. R., & Riley, J. M. 1987, MNRAS, 224, 847
Sandage, A. 1972, ApJ, 178, 25
Schmidt, M. 1965, ApJ, 141, 1
Sparks, W. B., Biretta, J., & Macchetto, F. D. 1994, ApJS, 90, 909
Sparks, W. B., Golombek, D., Baum, S. A., Biretta, J., de Koff, S., Macchetto, F., McCarthy, P., & Miley, G. K. 1995, ApJ, 405, L55
Spencer, R. E., McDowell, J. C., Charlesworth, Fanti, C., Parma, P., & Peacock, J. A. 1989, MNRAS, 240, 657
Spencer, R. E., et al. 1991, MNRAS, 250, 225
Spinrad, H., Djorgovski, S., Marr, J., & Aguilar, L. 1985, PASP, 97, 932
Trauger, J., et al. 1994, ApJ, 435, L3
Yates, M. G., Miller, L., & Peacock, A. 1989, MNRAS, 240, 129